Terms and Conditions of Use of Digitised Theses from Trinity College Library Dublin

Copyright statement

All material supplied by Trinity College Library is protected by copyright (under the Copyright and Related Rights Act, 2000 as amended) and other relevant Intellectual Property Rights. By accessing and using a Digitised Thesis from Trinity College Library you acknowledge that all Intellectual Property Rights in any Works supplied are the sole and exclusive property of the copyright and/or other IPR holder. Specific copyright holders may not be explicitly identified. Use of materials from other sources within a thesis should not be construed as a claim over them.

A non-exclusive, non-transferable licence is hereby granted to those using or reproducing, in whole or in part, the material for valid purposes, providing the copyright owners are acknowledged using the normal conventions. Where specific permission to use material is required, this is identified and such permission must be sought from the copyright holder or agency cited.

Liability statement

By using a Digitised Thesis, I accept that Trinity College Dublin bears no legal responsibility for the accuracy, legality or comprehensiveness of materials contained within the thesis, and that Trinity College Dublin accepts no liability for indirect, consequential, or incidental, damages or losses arising from use of the thesis for whatever reason. Information located in a thesis may be subject to specific use constraints, details of which may not be explicitly described. It is the responsibility of potential and actual users to be aware of such constraints and to abide by them. By making use of material from a digitised thesis, you accept these copyright and disclaimer provisions. Where it is brought to the attention of Trinity College Library that there may be a breach of copyright or other restraint, it is the policy to withdraw or take down access to a thesis while the issue is being resolved.

Access Agreement

By using a Digitised Thesis from Trinity College Library you are bound by the following Terms & Conditions. Please read them carefully.

I have read and I understand the following statement: All material supplied via a Digitised Thesis from Trinity College Library is protected by copyright and other intellectual property rights, and duplication or sale of all or part of any of a thesis is not permitted, except that material may be duplicated by you for your research use or for educational purposes in electronic or print form providing the copyright owners are acknowledged using the normal conventions. You must obtain permission for any other use. Electronic or print copies may not be offered, whether for sale or otherwise to anyone. This copy has been supplied on the understanding that it is copyright material and that no quotation from the thesis may be published without proper acknowledgement.

Plume dynamics in nanosecond and femtosecond laser ablation of metals

Tony Donnelly

Submitted for the degree of Doctor of Philosophy
School of Physics
University of Dublin
Trinity College

Declaration

I hereby declare that this thesis has not been submitted as an exercise for a degree in any other university.

This thesis is entirely my own work, except for the advice and assistance mentioned in the acknowledgements.

I agree to allow the library of Trinity College Dublin copy or lend a section or this entire thesis on request.

To my parents

Summary

This thesis examines the ablation plume produced from nanosecond and femtosecond laser ablation of metal targets in vacuum. Optical emission and absorption spectroscopy, a time-of-flight Langmuir ion probe and ablation depth measurements were used to study the ablation process. Nanosecond laser ablation plasma was also investigated as a deposition source for metal nanostructured film fabrication.

For nanosecond laser ablation the spectrally resolved plasma emission and absorption during the laser pulse is a broad continuum. Both spectral line broadening and a radiating hot surface are considered to cause this feature. The plasma absorption was measured in the visible region with a novel setup. Nanosecond laser ablation in vacuum has been shown to be a flexible and straight forward route to nanostructure film deposition. An effective medium theory was shown as a simple way to describe the main features of optical absorption by a silver nanoparticle film. Confined laser ablation was investigated as a technique to produce long lived dense laser ablation plasma. The confined plasma was used, for the first time, as a novel deposition source. The nanoparticle films produced from nanosecond laser ablation and from confined ablation show a very similar optical response and surface topography.

For femtosecond laser ablation the expansion dynamics of the plasma part of the ablation products was shown to be well described by the adiabatic isentropic model of plume expansion. The ion fraction is < 1% indicating that most of the ablated material leaves the target as nanoparticles. It seems a gas-dynamical approach can also describe the nanoparticle plume expansion but the physical reason for this remains unexplored. At high fluence the nanoparticle plume behaviour deviates from the model predictions and it

seems that this may be due to the increasing influence of the plasma pressure as the fluence is increased. Femtosecond laser ablation with double pulses has shown that the addition of a second delayed pulse has a strong influence on the dynamics of the ablated material and the overall ablation process. This is ascribed to the interaction of the second laser pulse with the structured nascent plume formed by the first pulse.

Acknowledgements

Publications and conferences attended (to date)

Publications

"Pulsed laser deposition of nanostructured Ag films", Tony Donnelly, Brendan Doggett and James G. Lunney, *Applied Surface Science*, *252, Issue 13, (2006) 4445-4448*

"A Comparative Study of Gadolinium Gallium Garnet Growth by Femtosecond and Nanosecond Pulsed Laser Deposition", M.S.B. Darby, T.C. May-Smith, R.W. Eason, T. Donnelly, J.G. Lunney and K.D. Rogers, *Applied Surface Science*, **254**, *11 (2007) 3364-3369*

"Pulsed laser deposition of nanoparticle films of Au", T. Donnelly, S. Krishnamurthy, K. Carney, N. McEvoy and J.G. Lunney, *Applied Surface Science*, *254, 4, (2007) 1303-1306*

"Optical absorption in early stage low temperature laser produced plasma", T. Donnelly and J.G. Lunney, *Appl. Phys. A, 92, 4, (2008) 951-955*

"Measurement of electron density in a laser produced plasma using a hairpin resonance probe", S.K. Karkari, B. Doggett, C. Gaman, T. Donnelly, D. O'Farrell, A.R. Ellingboe and J.G. Lunney, *Plasma Sources Sci. Tech., 17, 3 (2008) 032001*

"Growth of Carbon Nanotubes on Si Substrate Using Fe Catalyst Produced by Pulsed Laser Deposition", S. Krishnamurthy, T. Donnelly, N. McEvoy, W. Blau, J.G. Lunney, A.S. Teh, K.B.K. Teo, W.I. Milne, *J. Nanosci. Nanotech. 8, 11 (2008) 5748-5752*

"Double pulse ultrafast laser ablation of nickel in vacuum", T. Donnelly, J.G. Lunney, S. Amoruso, X. Wang, R. Bruzzese, X. Ni, *J. Appl. Phys.*, **106**, 013304 (2009)

"Dynamics of the plumes produced by ultrafast laser ablation of metals", T. Donnelly, J.G. Lunney, S. Amoruso, X. Wang, R. Bruzzese, X. Ni, *submitted to J. Appl. Phys.* (2010)

"Characterization of the nanoparticle component in ultrafast laser ablation metal plumes", T. Donnelly, J.G. Lunney, S. Amoruso, X. Wang, R. Bruzzese, X. Ni, *submitted to Appl. Phys. A* (2010)

Conferences

European Materials Research Society (EMRS), spring meeting May/June 2005, Strasbourg, France. Poster presentation titled *"Pulsed laser deposition of nanostructured Ag films"*.

European Materials Research Society (EMRS), spring meeting May/June 2007, Strasbourg, France. Poster presentation titled *"Pulsed laser deposition of nanoparticle films of Au"*.

Conference of Laser Ablation (COLA), September 2007, Tenerife, Spain. Poster presentation titled *"Optical absorption in early stage low temperature laser produced plasma"*.

Radiative properties of hot dense matter workshop, November 2008, Santa Barbara, California, USA. Poster presentation titled *"Optical absorption in early stage low temperature laser produced plasma"*.

Photonics Ireland, September 2009, Kinsale, Co. Cork, Ireland. Oral presentation titled *"Ultra-short laser ablation of metals"*.

Table of contents

Laser ablation involves focusing the output from a pulsed laser onto a solid target at power densities sufficient to vaporise a small amount of material at the target surface. Traditionally nanosecond lasers have been used to ablate solid targets; and for metals a laser fluence of ≥ 1 J cm^{-2} is required to remove a thin layer of material from the target surface. Below this threshold value modification of the target surface can still take place by surface melting and ejection of particles due to surface excitation. When bulk removal of material takes place by laser ablation, plasma is usually formed in the ablation process.

The main mechanisms involved in laser ablation and plasma formation are understood. Figure 1.1 shows the different stages that occur during nanosecond laser ablation. The laser is incident on a solid target (a) and the early part of the laser pulse heats the target past the melting point, a melt layer is produced and a melt front begins to propagate (b) into the target. Further heating of the surface by the laser leads to vaporisation (c). A rarefaction wave propagates into the target and the vapour begins to expand away from the target surface. Laser absorption in the vapour leads to ionisation and plasma formation (d). Between (c) and (d) the laser energy reaching the target has reduced and the melt front reaches its deepest position and begins to recede. Absorption of the laser in the plasma leads to plasma heating and depending on the laser wavelength and plasma density and temperature, total shielding of the target surface can occur.
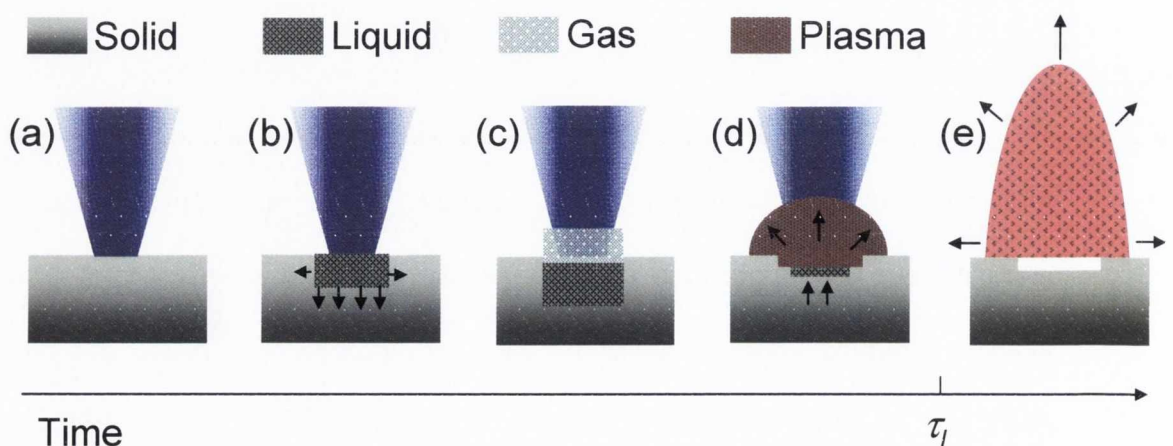
Figure 1.1 The various stages of nanosecond laser ablation of a solid target.

2

At the end of the laser pulse duration, τ_l, the plasma begins adiabatic three-dimensional expansion. The condition of the plasma depends on a number of factors including the pulse energy, its temporal and spatial profile and also the target condition. This process will be described in more detail in the theory section. Although a general understanding exists there are several features of the laser ablation process that are not fully understood. The laser absorption in the vapour/plasma produced by the leading edge of the laser pulse ((c) and (d) in Fig. 1.1) is one such point. The exact absorption mechanisms that act to shield the target surface and heat the vapour/plasma are not fully clear. It is understood that several mechanisms can contribute to the overall absorption but it is not known which process is dominant, particularly for plasma produced using lasers operating in the UV. To add to the complexity, the plasmas under consideration are highly non-ideal. Due to the high density ($\sim10^{19}$ cm^{-3}) and low temperatures (few eV) encountered in these plasmas they are strongly coupled. Strongly coupled plasma is plasma in which the Coulomb interaction energy is comparable to the plasma thermal energy. Strongly coupled plasmas of this kind exhibit a number of non-ideal effects which are not present in classical weakly coupled plasma. Part of the research presented in this thesis will try to shed some light on the optical properties of the early stage of the laser ablation plasma through measurement of the optical absorption and comparison to opacity calculations using a spectral synthesis code.

At the end of the laser pulse a dense, cool plasma layer is present on the target surface. The initial plasma thickness is typically an order of magnitude smaller than the other plasma dimensions and thus the larger pressure gradient normal to the target drives a forward directed 'plume' expansion, the physics of which is described by several gas dynamic models. The expansion model of Anisimov [6] has been applied to the expansion of plasma plumes in vacuum and has been shown to accurately describe nanosecond laser

ablation plasma plumes [7, 8]. The Anisimov model will be described in the theory section and will be applied in the later chapters.

Knowledge of the expansion dynamics of the ablated material is of direct relevance to thin film fabrication by PLD but it is often ignored by the thin film research community who utilise PLD as a deposition technique. High energy ions (~ 100eV) produced in the ablation process can induce significant self sputtering of the deposited material. The angular spread of the ablated material can also leads to a non-uniform thickness profile which is undesirable for thin film growth. As part of the work in this thesis we investigate deposition of ultra thin metal films and pay particular attention to a characterisation of our deposition plasma. Ultra thin metal films are structured on nanometer size scales and are of interest due to novel optical and catalytic properties. PLD grown nanostructured films are receiving interest due to the possibility to tailor film properties by change in the deposition parameters. It is of interest to correlate the removed material and the plasma expansion behaviour with the deposition of the ablated material and this will be investigated later in the thesis. The relevance of considering the ablation plume dynamics during deposition will be shown and an interesting application of laser ablation of metals for the growth of nanoparticle films will be demonstrated.

The previous discussion and outline of existing problems in the field of laser ablation has been concerned entirely with ablation using nanosecond laser pulses. In recent years femtosecond pulses have been used to ablate solid targets for material removal. Femtosecond laser ablation as it's called has also become known as ultra-short laser ablation (ULA). The ULA ablation process is quite different to ns ablation. During ULA of metals the laser energy is absorbed by free electrons in a thin layer on the target surface. This energy is transferred to the lattice in a period of time determined by the electron phonon coupling of the target material. For metals this time is of the order of picoseconds and for pulse lengths shorter than this the heat conduction into the target does not take

4

place during the laser pulse. This leads to critical heating of a thin layer of material on the target surface which subsequently cools and decomposes into a mixture of ions, atoms and nanostructured matter [9]. This material expands away from the target as a plume of material with very different characteristics than that produced from nanosecond laser ablation where the pulse is sufficiently long to allow for electron-lattice thermalisation and interaction with the ablated material. Much research has gone into understanding the ablation mechanisms and the dynamics of the irradiated surface but little attention has been paid to expansion dynamics of the ablated material. This will become more important as researchers explore the use of PLD with femtosecond pulses so a section of this thesis has been devoted to experiments to measure the expansion dynamics of ULA of a metal target. A comparison to the Anisimov model, used for nanosecond ablation, will be made to assess its applicability to ULA. We will also consider ablation using a pair of pulses separated by a fixed delay and look at how the ablation process can be modified by changing the time lag between pulses. This is significant as control over the material removal process allows for a flexible deposition technique.

1.2 References

[1] T.H. Maiman, *Nature*, **187**, 4736, 493-494 (1960)

[2] H.M. Smith and A.F. Turner, *Appl. Optics*, **4**, 147 (1965)

[3] *Pulsed Laser Deposition of Thin Films*, D. B. Chrisey and G. K. Hubler, Wiley-VCH, (1994)

[4] *Pulsed Laser Deposition of Thin Films, Application-Led Growth of Functional Materials,* R. Eason, Wiley (2006)

[5] *Laser Ablation and its Applications*, C. Phipps, Springer (2006)

[6] S. I. Anisimov, D. Bauerle and B. S. Luk'yanchuk, *Phys. Rev. B*, **48**, 12076 (1993)

[7] T. N. Hansen, J. Schou and J. G. Lunney, *Appl. Phys. A*, **69**, S601-S604 (1999)

[8] B. Toftmann, J. Schou and J. G. Lunney, *Phys. Rev. B*, **67**, 104101 (2003)

[9] S. Amoruso, R. Bruzzese, X. Wang, N. N. Nedialkov and P. A. Atanasov, *J. Phys. D: Appl. Phys.*, **40**, 331-340 (2007)

Chapter 2: Theory

In this section the relevant theory for laser ablation is given. Nanosecond laser ablation is considered and the ablation process is described in terms of an exact laser heating model which, upon extension to describe vaporisation, quickly turns into a computationally complex problem. A simpler model outlining the main mechanisms of ablation is described. Laser ablation research has to date been inadequate with regard to the description of the laser absorption in the plasma produced during ablation. This will also be discussed. The main features of ultra-short laser ablation are described. The target heating during ULA is outlined and the physics of target decomposition are explained.

The second part of the theory section describes the Anisimov model of adiabatic, isentropic, self similar plume expansion of the ablated material in vacuum. The formation of the model is given together with the equations describing the plume shape, time of flight and the pressure and density profiles within the plume. The final part of the theory section describes the optical properties of metal nanoparticles using an effective medium theory interpretation. An explanation of the theory involved is necessary in order to understand the use of optical techniques to characterise the deposits during pulsed laser deposition of ultra-thin metal films.

2.1 Laser ablation and plasma formation

During laser irradiation of a metal surface the laser pulse is absorbed in a thin layer determined by the optical absorption coefficient, α.

$$\alpha = \frac{4\pi k_{ext}}{\lambda} \qquad (2.1)$$

k_{ext} is the extinction coefficient of the metal and λ is the laser wavelength. The optical absorption depth, $d_{opt} = \alpha^{-1}$. For wavelengths in the visible region of the spectrum, d_{opt} is typically around a few nanometers. The laser is absorbed by the electrons in a thin layer at the target surface. Heating takes place via electron collisions that occur on a timescale τ_e and energy is transferred to the lattice by electron - phonon interactions which occur on a timescale τ_{ep}. The electron phonon coupling time, τ_{ep} is of the order of several ps for most metals and $\tau_{ep} \gg \tau_e$. Modern laser systems can now produce ultra-short (femtosecond) to short (nanosecond) pulses. Depending on how the pulse length τ_l compares with the electron-phonon relaxation time, different physical mechanisms are responsible for ablation. For femtosecond laser ablation, τ_l is shorter than the electron-phonon coupling time so the laser energy is initially absorbed by the free electrons within the metal. During the laser pulse, the electrons undergo rapid heating to a high temperature compared to the cold lattice. At later times of order of the electron phonon coupling time, the electron temperature drops and the lattice temperature increases. During this stage the heated layer decomposes into a combination of atoms, ions, and nanoparticulate matter and expands away from the target surface. On the other hand, for nanosecond pulses which are longer than τ_{ep}, the temperature of the electron and ion subsystems equilibrate very early in the laser pulse duration. Melting occurs during the laser pulse and further heating raises the

8

surface temperature to values of the order of the boiling point. At temperatures approaching the boiling point vapour is formed on the target surface. This occurs well before the end of the laser pulse if the laser fluence is large enough. The latter part of the pulse is then absorbed in the vapour, heating it so that ionisation occurs and plasma is formed on the target surface. A more detailed description of each process will be given further in this chapter.

2.1.1 Nanosecond laser ablation

As the pulse length is much longer than the electron-phonon coupling time, nanosecond ablation can be modelled using standard heat flow equations to describe laser heating of the target. The heat penetration depth, L_{th} is given by $L_{th} = 2(D\tau_l)^{1/2}$ and is the depth of heated material at the end of the laser pulse, assuming a constant laser intensity with time. D is the thermal diffusivity of the metal and τ_l is the laser pulse duration. The thermal diffusivity is given by $D = \dfrac{k_c}{C\rho}$ where ρ is the target material density, k_c is the bulk thermal conductivity and C is the specific heat capacity. For silver $k_c = 4.27$ W cm^{-1} K^{-1} and $C = 0.24$ J g^{-1} K^{-1} which gives $D = 1.69$ cm^2 s^{-1}. Then considering ablation using a KrF excimer laser (248 nm, ~30 ns) gives a value of $L_{th} \approx 4$ μm and $d_{opt} \approx 15$ nm. As $L_{th} \gg d_{opt}$ the laser heating can be modelled as a surface heat source and the following equation [1] can be used to describe the laser heating.

$$\rho C \frac{\partial T}{\partial t} = \frac{\partial T}{\partial z}\left(k_c \frac{\partial T}{\partial z}\right) + \alpha\left(1 - R\right)I_0 \exp(-\alpha z) \tag{2.2}$$

In the above equation, α is the optical absorption coefficient at the laser wavelength, I_0 is the laser intensity and z is the distance into the target. The above equation is difficult to

solve because of the non-linear boundary condition for vaporisation, a moving solid-liquid interface (melt front) is present and all the thermodynamic properties are temperature dependent. Figure 2.1 shows the variation of k_c, C and D with temperature [2].
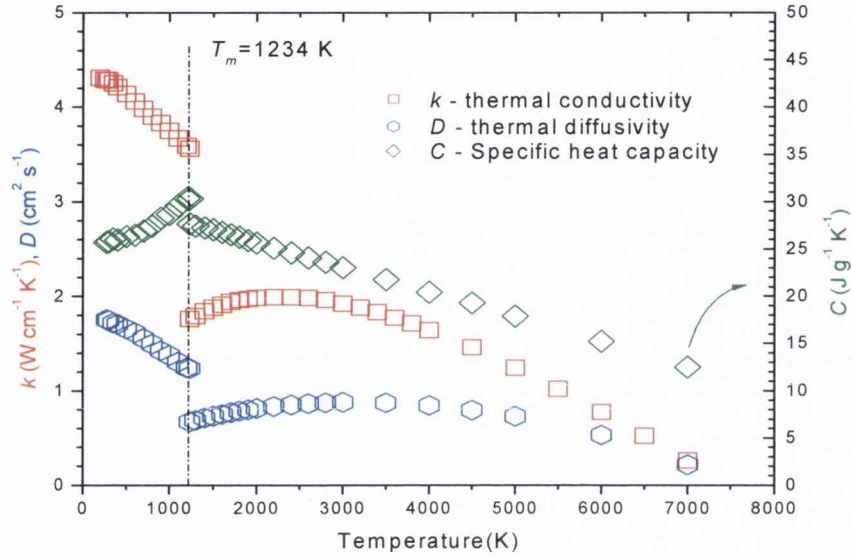
Figure 2.1 Thermal conductivity, specific heat capacity and thermal diffusivity for silver as a function of temperature. T_m is the melting point of silver.

A solution to the above problem, in the absence of vaporisation, was put forward by Tokarev and Kaplan [3]. They calculated the heating rate, the time to reach the melting point, the position of the melt front as a function of time and also included an analysis to predict the surface cooling and the position of the re-solidification layer as a function of time after the end of the laser pulse and assuming a constant laser intensity temporal profile. The solution to the set of equations given in Ref. 3 for temperature, T as a function of time, t, and distance, z, from the target surface is

$$T(z,t) = \frac{2(1-R)I_0}{C\rho}\left(\frac{t}{D}\right)^{\frac{1}{2}} ierfc\left(\frac{z}{2(Dt)^{\frac{1}{2}}}\right) + T_i \qquad (2.3)$$

10

In the above equation T_i is the initial surface temperature and the other quantities are as before. Letting $z = 0$ yields the surface temperature as a function of time.

$$T_s(0,t) = \frac{2(1-R)I_0}{C\rho}\left(\frac{t}{\pi D}\right)^{\frac{1}{2}} + T_i \qquad (2.4)$$

After the end of the laser pulse the temperature is described by

$$T_s(0,t) = \frac{2(1-R)I_0}{C\rho}\left(\frac{1}{\pi D}\right)^{\frac{1}{2}}\left(t^{\frac{1}{2}} - (t-\tau_l)^{\frac{1}{2}}\right) + T_i \qquad (2.5)$$

where τ_l is the laser pulse duration. In Fig. 2.2 the above set of equations are used to predict the surface temperature during and after the laser pulse for 248 nm laser irradiation of silver at a laser fluence of 0.5 J cm^{-2} and pulse duration of 26 ns. The reflectivity, R, of Ag at 248 nm is 0.2.
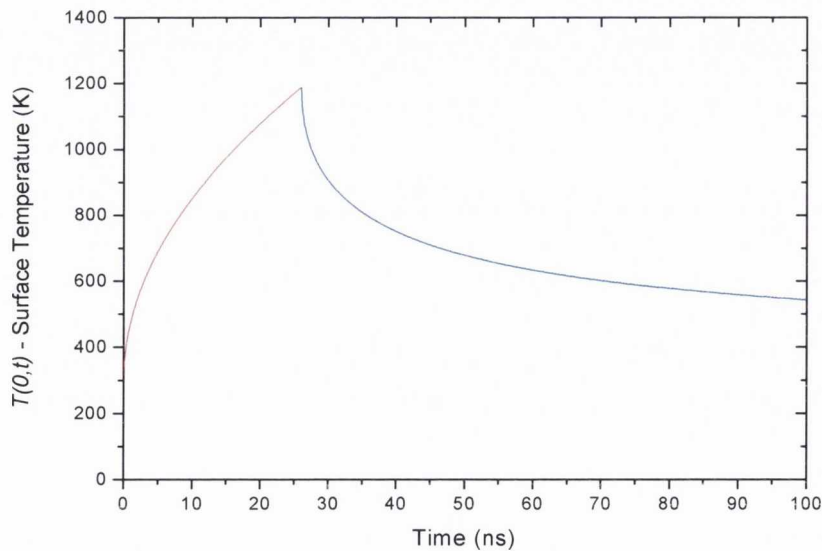
Figure 2.2 Surface temperature calculated using equations 2.4 (red) and 2.5 (blue) for 248 nm, 26 ns ablation of Ag at 0.5 J cm^{-2}.

In this particular case the intensity is just sufficient to raise the temperature to the melting point. For this calculation, constant values of k_c, ρ and C and R were used; whereas it would be more appropriate to use the temperature - dependent values shown in Fig. 2.1. Extending the above formalism to include vaporisation and shielding of the laser would be difficult and the temperature dependence of the physical quantities would also need to be included. Furthermore, the temperature - dependent reflectivity is also not well known. Due to the significant complexity of formulating an exact analytical model for laser ablation including vaporisation, approximate models have been devised to describe the main features of the ablation process [4, 5, 6, 7]. One such model will be described to emphasise the main mechanisms involved in laser ablation of a metal target.

2.1.2 Laser ablation model

In this section the ablation model of Lunney and Jordan [4] will be described. As shown in the example above the laser penetration depth is small in comparison to the thermal diffusion depth so the laser is treated as a surface heat source. The surface temperature T_S can be approximated by Duhamel's theorem [8];

$$T_S(t) = T_i - \frac{L_F}{C} + \frac{1}{\sqrt{\pi k_c \rho C}} \int_0^t I_S(t-\tau) \frac{d\tau}{\sqrt{\tau}} \qquad (2.6)$$

where L_F is the latent heat of fusion and k, ρ, c and T_i are as before. Constant values for these quantities have been employed in the model. In the original study room temperature values were used, though it may have been more appropriate to use average values taken over a wide temperature scale (see Fig. 2.1). The laser intensity reaching the target surface, $I_S(t)$, is given by the following equation.

12

$$I_S(t) = (1 - R_L)I_L(t)\exp\left(-\frac{\sigma Nl}{\cos\theta}\right) + I_P(1 - R_P) - \left(\frac{d(Nl)}{dt}\right)L_V \qquad (2.7)$$

$I_L(t)$ and I_P is the laser and plasma radiation intensity, R_L and R_P are the target reflectivity to the laser and plasma radiation. N is the average ion/atom density in the vapour, l is the vapour layer thickness and σ is the total absorption cross section of the vapour. The product $Nl\sigma$ gives the optical opacity of the layer and the $\cos\theta$ term accounts for the angle of incidence of the laser irradiation. L_V is the latent heat of vapourisation of the material under ablation. I_P, the plasma emission intensity is given by Stefan's law, $I_P = \sigma_s T_P^4(1 - \exp(-Nl\sigma))$ which describes the emission of the plasma up to a blackbody limit. The rate of change of the number of atoms/ions per unit area $d(Nl)/dt$ is given by

$$\frac{d(Nl)}{dt} = P_V\sqrt{\frac{1}{2\pi Mk_B T_S}} \qquad (2.8)$$

where P_V is the vapour pressure which is given by the Clausius – Clapeyron equation. The plasma temperature is then calculated by considering the laser power absorbed by the vapour and the power lost by emission. The model was originally applied to 248 nm ablation of iron and a complementary experimental study [9] showed it predicts the main features of the ablation process. Figure 2.3 shows the surface and plasma temperature and the plasma density calculated for iron ablation in that study with 26 ns, 248 nm pulses at a fluence of 4.5 J cm^{-2}.
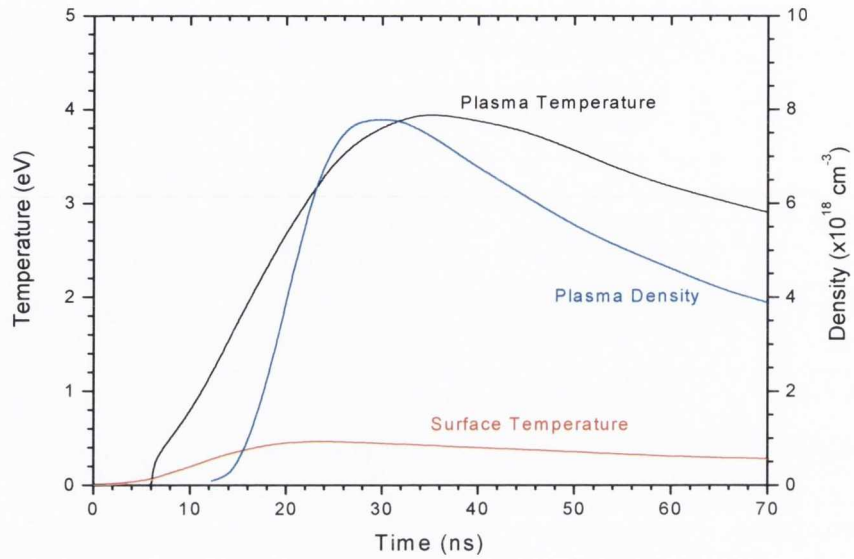
Figure 2.3 Target surface and plasma temperature and plasma density as a function of time for 248 nm abaltion of Fe at 4.5 J cm^{-2}.

Other more complex hydrodynamic models can also be used to simulate laser ablation but these are usually in the form of sophisticated computer codes which are not easily modified. One example was a recent study by Qaisar and Pert [10] where they have used the two-dimensional plasma hydrodynamic code POLLUX to simulate laser ablation of magnesium and compared with experimental results. They show reasonable agreement between the code output and experimental measurements.

One thing which is clear from the simplistic ablation model above and the detailed POLLUX model is that both include an over-simplified treatment of the laser absorption in the plasma. In the simple laser ablation model photo-ionisation from high-lying states was considered to dominate over inverse bremstrahlung and a single value of absorption cross section was used for all atoms and ions. This is a gross simplification but results in reasonable agreement with the experiment as the value chosen is close to the experimentally measured value at the laser wavelength. On the other hand, the hydrodynamic code calculation mentioned above considered only inverse bremstrahlung absorption which may be adequate when dealing with ablation using lasers operating in the

14

infra-red but is not sufficient for ablation using visible and UV pulses. In the next section we take a closer look at the laser absorption and the mechanisms involved.

2.1.3 Laser absorption

Absorption of the laser in the plasma reduces the laser intensity reaching the target surface and decreases the ablation rate. The absorbed energy heats the ablated material and plasma is formed. The laser absorption during the laser pulse also acts to regulate the plasma density and temperature. Consequently an accurate understanding of the mechanisms of light absorption in the plasma is critical for an understanding of the plasma formation and expansion dynamics.

Plasma can emit and absorb photons through three different types of interaction with electrons. The first of these is known as bound – bound absorption. The electrons can absorb photons of energy corresponding to the difference in energy of its current level and a higher lying level. Bound – bound transitions result in discrete absorption due to the finite energy values the electrons can occupy. When a bound electron absorbs a photon of energy greater than its ionisation energy the electron is freed from its parent atom/ion and any excess of energy is converted to kinetic energy. This type of absorption is known as bound-free absorption and results in photoionisation (PI) of the parent atom or ion. PI gives rise to a continuous absorption spectrum.

Photon absorption in plasma can also occur through collisions between free electrons and ions and atoms. Passing through the electric field of an atom or ion, an electron can absorb a photon and gain kinetic energy. This process is known as inverse bremsstrahlung (IB) and due to the difference in field strength for the ions compared to neutral atoms, IB absorption due to ions dominates over that from neutral species [11]. A generalised energy level diagram depicting the three different absorption mechanisms is given in Fig 2.4.

15
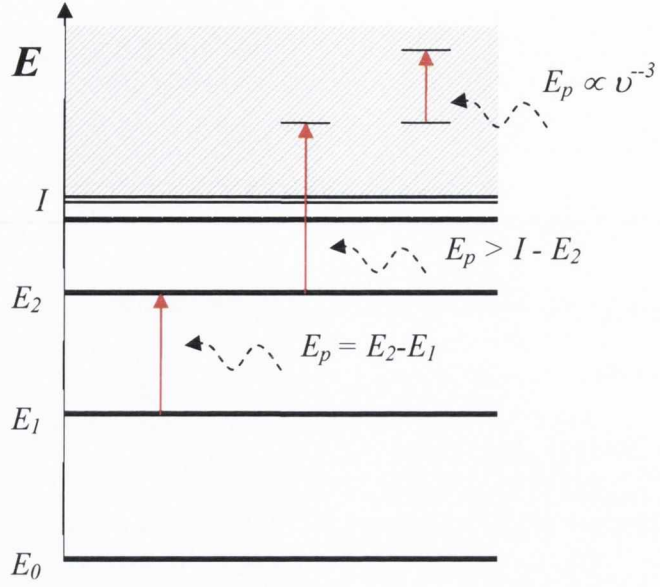
Figure 2.4 Generalised energy level diagram indicating the three different absorption mechanisms that can take place for atoms and ions in plasma. I **represents the ionisation limit of the atom or ion and the grey shaded area indicates the free electron ensemble in the plasma.** E_n **represents energy levels of quantum number** n**.**

The bound - bound absorption coefficient k_{bb} can be expressed as

$$k_{bb} = \frac{e^2}{4\varepsilon_0 mc} N_1 f_{12} L(\upsilon) \qquad (2.9)$$

where e is the charge of the electron, ε_0 is the permittivity of vacuum, m is the electron mass and c is the speed of light. N_1 is the density atoms in the lower level of the transition, f_{12} is the oscillator strength between the lower and upper level involved in the transition and $L(\upsilon)$ is the line shape function. f_{12} is related to the transition probability, A_{21} between levels and determines the emitted signal strength.

$$f_{12} = \frac{g_2}{g_1}\left(\frac{\varepsilon_0 mc^3}{2\pi e^2 \upsilon_{12}{}^2}\right) A_{21} \qquad (2.10)$$

Both f_{12} and A_{21} depend on the transition dipole moment between the initial and final quantum states. The dipole moment is given by the dipole matrix element which is found from the wavefunctions of the two states involved in the transition. To accurately calculate the total bound-bound absorption the detailed energy level structure of each ion stage needs to be known as well as the relative populations of each level. To calculate the transition rates between levels and the resultant overall emission the oscillator strengths between levels must also be known. As several ion stages may coexist in the plasma at a particular time, many transitions can occur resulting in a complex problem. For low Z elements and for low ionisation stages tabulated data are available for energy levels and transition strengths [12]. For medium Z elements and at higher ionisation stages atomic structure calculations [13] are performed to calculate the atomic and ionic wavefunctions from which the transition probabilities can be found. These calculations are difficult to perform accurately and, coupled with the need to incorporate them into a level population model, this can represent a significant computational exercise [14].

The calculation of bound-free absorption due to PI also requires knowledge of the energy level structure and transition rates of plasma species. Alternatively a more simplistic analysis [11] based on a calculation originally performed by Kramer can be used which assumes hydrogen-like atoms and the existence of at least partial thermal equilibrium. The equation for the bound - free absorption coefficient as derived by Kramer can be expressed as

$$k_{bf} = \frac{64\pi^4}{3\sqrt{3}} \frac{e^{10} m Z^4 N}{h^6 c \upsilon^3} \sum_{n^*}^{\infty} \frac{1}{n^3} \exp\left(-\frac{I}{k_B T}\left(1 - \frac{1}{n^3}\right)\right) \tag{2.11}$$

where e, m and c are as before, h is Planck's constant, Z is the nuclear charge, υ is the frequency of the incident electromagnetic radiation. N is the total plasma density, I is the

ionisation energy of the atom or ion in question and n is the principal quantum number of energy levels that the electron can occupy. The summation in the equation above refers to levels of $n*$ that the photon energy is greater than the energy difference between the ionisation limit (at $n \to \infty$) and the electron level in question. T is the plasma temperature and k is Boltzmann's constant. The above equation is strictly only valid for hydrogen-like systems but it works well for high-lying states of any species due to the fact that all atoms and ions become increasingly hydrogen-like for large n [15].

The IB absorption coefficient k_{ff} (cm^{-1}) can be calculated using the following equation [11].

$$k_{ff} = \frac{4}{3} \left(\frac{2\pi}{3mkT} \right)^{\frac{1}{2}} \frac{Z^2 e^6}{hcm\upsilon^3} N_i N_e \approx 3.7 \times 10^8 \frac{Z^2}{T^{\frac{1}{2}}\upsilon^3} N_i N_e \qquad (2.12)$$

All symbols are as before and in the simplified form above where k_{ff} is in units of cm^{-1}, T must be expressed in Kelvin. It is clear from the above equation that IB absorption will be most efficient in the long wavelength region of the spectrum. If we use the Saha equation to express the product $N_i N_e$ in terms of the ground state population N_1 and assuming $N_1 \sim N$, N being the total density, Eq. 2.12 can be re-written as:

$$k_{ff} = \frac{16\pi^2}{3\sqrt{3}} \frac{e^{10} m Z^4 N}{h^6 c \upsilon^3} \frac{\exp\left(-\frac{I}{kT}\right)}{\frac{I}{kT}} \qquad (2.13)$$

The equations for bound-free and free-free absorption both show a υ^{-3} dependence so that a simple equation can be derived for k_c, the continuous absorption coefficient which is the sum of k_{bf} and k_{ff}. This equation, known as the Kramers-Unsöld formula, is given as

$$k_c = \frac{16\pi^2}{3\sqrt{3}} \frac{e^6 m Z^2 kTN}{h^4 c \upsilon^3} \exp\left(-\frac{I - h\upsilon}{kT}\right) \qquad (2.14)$$

The semi-classical equations above are derived by treating the radiation field classically while the atomic system is described by quantum physics. They are especially accurate for hydrogen-like systems and reasonably accurate for treating the excited states of other systems [15].

When plasma is no longer weakly coupled i.e. small Coulomb interaction energy compared to thermal energy, a number of effects can occur that influence its optical properties. The plasma produced during laser ablation of solids are dense (10^{18} - 10^{19} cm^{-3}) and of low temperature (~ few eV). Under these conditions there is strong interaction between the electron and ions in the plasma to produce a highly non-ideal system [16, 17]. These types of plasmas are termed strongly coupled plasmas as the Coulomb interaction energy is comparable to the thermal energy in the plasma. When the ion coupling parameter, Γ is > 0.1 the plasma is strongly coupled. Γ is the ratio of potential to kinetic energy and is defined as

$$\Gamma = \frac{e^2 Z^2}{4\pi\varepsilon_0 k_B T} \left(\frac{4\pi}{3} N_i\right)^{\frac{1}{3}} \qquad (2.15)$$

For an aluminium plasma with $N_e = 1\times10^{19}$ cm^{-3} and $T_e = 2$ eV the corresponding mean ion charge Z, was found to be 0.85 from a plasma collisional - radiative model [18]. Inserting these values into the above equation yields $\Gamma \approx 0.2$. The above conditions are typical of laser ablation plasmas which, due to the high value of Γ, are subject to several non-ideal effects. The model of ionisation balance based on the Saha Boltzmann equation breaks down and significant ionisation potential depression (IPD), which is the reduction of the

binding energy due charge screening as the density increases, can occur [16]. The presence of large microfields in the plasma induces significant broadening and shifting of spectral lines [19]. For some conditions this effect can be so pronounced that merging of bound-bound transitions can occur and the bound-bound absorption spectrum is quasi-continuous as opposed to consisting of discrete transitions. Furthermore, discrete transitions in weakly coupled plasma can occur as bound-free transitions in strongly coupled plasma due to the IPD effect. The broadening of spectral lines due to plasma microfields has been studied by H. R. Griem [19]. For a limited set of elements broadening parameters have been calculated and tabulated [20]. For hydrogen and helium-like atomic systems accurate calculation have been performed that agree well with experiment but for other atomic systems calculations of the broadening are difficult to perform accurately. The IPD can be estimated using various models [21] (e.g ion sphere model) and incorporated into a model of the plasma ionisation dynamics.

Given the complexity of calculating the optical emission and absorption of dense low temperature plasma we make use of a spectral synthesis computer code to compute spectra to compare against experimental measurements. The PrismSPECT code [22] calculates the plasma ionisation and level populations incorporating IPD, includes data for energy level structure and transition probabilities, calculates the emission and absorption including line broadening and allows for simplistic treatment of radiative transfer effects in the plasma. A simpler spectral code called FLYCHK [23] was also investigated but it was found that the line broadening treatment and atomic data included in this code was not suitable for dense low temperature plasma. PrismSPECT includes a full atomic database and the line broadening is in good agreement with the published work of Griem [20] for certain test cases. More detail of the PrismSPECT code will be given in the next section.

Figure 2.5 shows a calculation from PrismSPECT for aluminium plasma for several values of temperature and density to illustrate some of the effects that were discussed in this section.
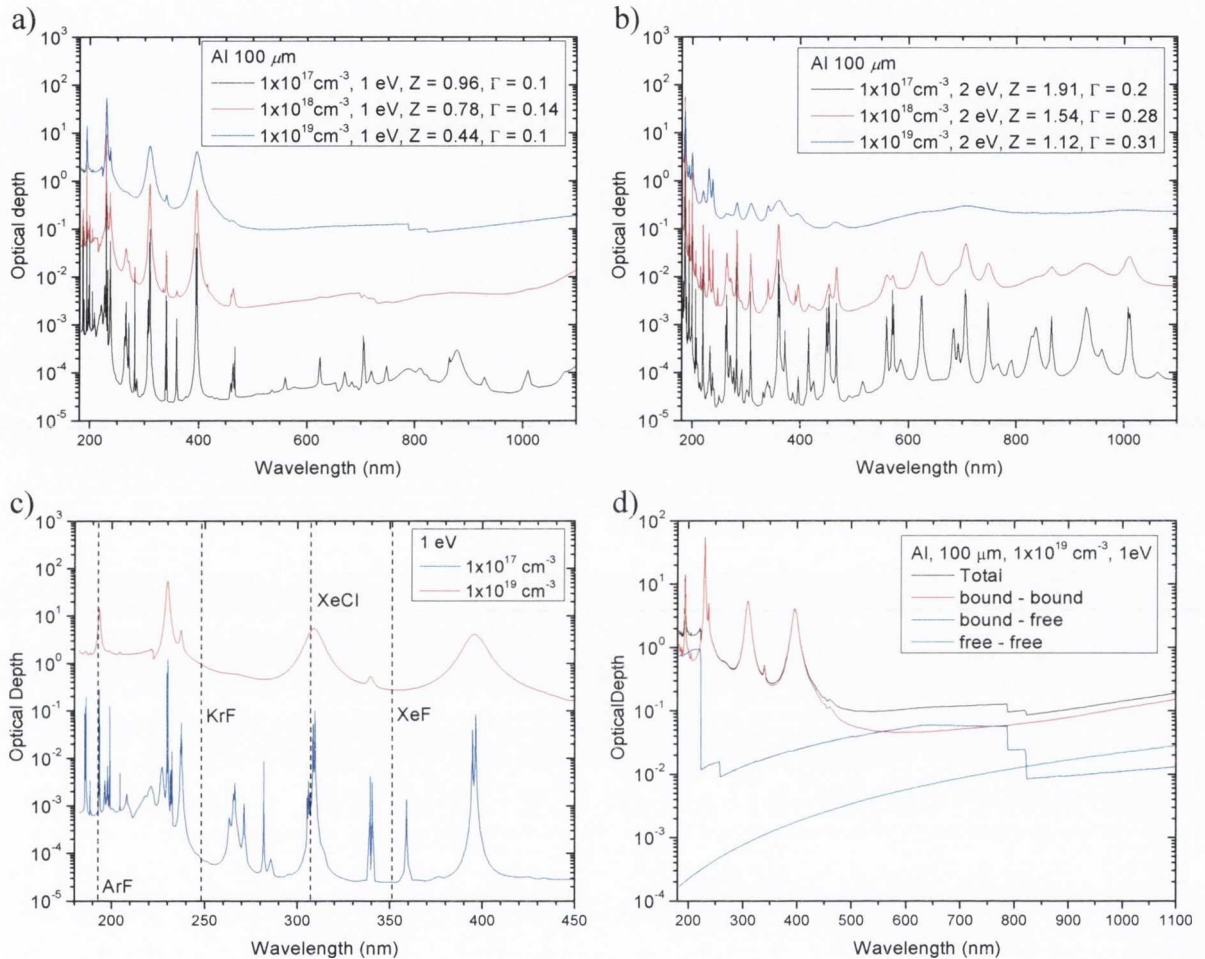
Figure 2.5 PrismSPECT calculations for the wavelength dependant optical depth of a slab of aluminium plasma of 100 micron thickness. (a) and (b) show the absorption as a function of density for 1 and 2 eV plasma temperature respectively. (c) shows the absorption in the UV and the wavelengths of several excimer lasers are indicated by dashed lines. (d) shows the contributions to the total absorption for one particular case.

In the above figure the optical depth is calculated as a function of wavelength for 100 μm thickness aluminium plasma of varying density and electron temperature. A number of discrete transitions due to neutral and singly ionised Al are present. Increasing the plasma density gives rise to a number of effects. There is significant broadening of lines and merging of bound - bound transitions. IPD is also evident in (a) from the photoionisation

edges located in the regions 600 - 800 nm. The movement of the edge to higher wavelengths indicates a lowering of ionisation potential due to the increased effects of neighbouring charges influencing the binding of the electron to the parent atom. The ion coupling parameter in each of the cases in (a) and (b) are ~ 0.1 indicating the plasma is strongly coupled. Fig. 2.5 (c) show the absorption in the UV in the vicinity of several commonly used excimer lasers. It can be seen that some of the laser wavelengths (ArF – 193 nm, XeCl – 308 nm) correspond to strong absorption lines indicating the importance of including bound – bound absorption when considering energy deposition into the plasma during ablation. Although the level populations will change during heating of the plasma the fact that at high density the absorption spectrum is a quasi - continuum due to broadening indicates absorption due to bound - bound states must be considered when dealing with laser absorption and radiative transfer in the plasma. From (d) the relative contributions to the overall absorption can be seen. Absorption due to bound transitions is the main mechanism, whereas bound - free is significant in the UV and free absorption does not contribute even in the near IR for this calculation. Later in this thesis, laser produced plasma will be characterised under standard ablation conditions and the spectral codes will be used to calculate the absorption properties of the plasma during laser ablation.

2.1.4 Femtosecond laser ablation

The physical mechanisms involved in ablation using femtosecond pulses are considerably different to nanosecond laser ablation. For metals, the free electron ensemble absorbs the laser irradiation in a thin layer near the target surface determined by the optical penetration depth (Eq. 2.1). The electrons are initially driven into a highly excited state compared to the lattice after which the absorbed laser energy is transferred to the lattice on a time scale determined by the electron - phonon coupling in the target material. This

quenches the electron excitation and the lattice temperature rises. The absorption of the laser energy and redistribution of this energy as heat in the lattice can be described by the two temperature model [24]. The one - dimensional equations that describe the energy exchange between the electron and lattice subsystems are;

$$C_e \frac{\partial T_e}{\partial t} = \frac{\partial}{\partial z}\left(k_e \frac{\partial T_e}{\partial z}\right) - \Pi(T_e - T_l) + Q$$

$$\text{(2.16)}$$

$$C_l \frac{\partial T_l}{\partial t} = \frac{\partial}{\partial z}\left(k_l \frac{\partial T_l}{\partial z}\right) + \Pi(T_e - T_l)$$

where C_e and C_l are the heat capacities and k_e and k_l are the thermal conductivities for the electrons and the lattice respectively. T_e and T_l are the electron and lattice temperatures, Π is the electron lattice energy coupling term and Q is the laser source term. As the lattice heat transport is orders of magnitude smaller than the electron heat transport the term involving k_l in the second equation of Eq. 2.16 can be dropped. To find the temporal variation of T_e and T_l the above coupled differential equations can be solved numerically and under certain assumptions, analytical solutions can also be found. Figure 2.6 is an example of a calculation performed by Ivanov [25] for ablation of a 50 nm nickel film at an absorbed laser fluence of 0.043 J cm^{-2} using 200 fs pulses.
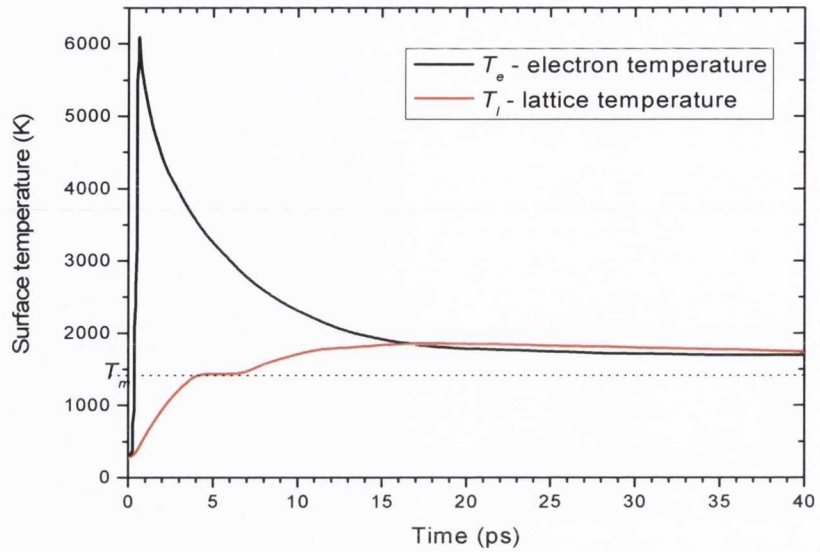
Figure 2.6 Temporal evolution of surface ion and electron temperature during fs laser ablation of a Ni thin film. From Ref. [25]

From this calculation it can be seen that the electrons are subjected to an extraordinary heating rate while the lattice remains comparably cold in the early stages. After a period of time which is determined by energy transfer times between electrons and the lattice, the lattice temperature increases as energy is acquired from the excited electrons. The electron excitation is reduced while the lattice reaches the melting point after which the temperature increases and becomes approximately equal to the electron temperature at ~ 20 ps. Several researchers have predicted the amount of material removed during ablation by using the two temperature model. An ablation criterion often used is that the lattice energy must exceed the heat of vaporisation, $C_l T_l > \rho \Omega_{vap}$ where ρ and Ω_{vap} are the density and enthalpy of vaporisation of the target material. Two examples of such modelling are given by Nolte [26] and Vestentoft [27]. Both consider two separate ablation regimes depending on the laser fluence used. Ablation in the first regime is determined by the optical absorption depth of the incident laser pulse. As the fluence is increased, electronic heat conduction determines the depth of heated material. In both frameworks the ablation depth due to optical penetration (low fluence) d_{opt}, can be described by a logarithmic relationship. In

24

Nolte's interpretation of the heat conduction equations there is also a logarithmic dependence of the ablated depth on the laser fluence at higher laser fluence. In contrast to this, Vestentoft's analysis predicts a linear relationship between the ablated depth and fluence in the electron heat conduction regime. This interpretation of the heat conduction equations resulted in the reduction of the two coupled differential equations to an individual differential equation for which an analytical solution for the temperature distribution is known. It seems that the reason why both models arrive at different depth dependence on fluence is due to the fact that first model considers a fixed ablation time (the electron phonon coupling time) where the second model considers an ablation time that is fluence dependent. The models will be described in more details in a later section and a comparison to experiment will be made.

More complicated modelling can be undertaken in the form of hydrodynamic [28, 29, 30, 31] or molecular dynamic simulations [32, 33, 34] of the ablation process. Hydrodynamic calculations treat a large scale system through knowledge of the material's equation of state whereas molecular dynamic calculations consider an atomistic system where position, velocity and force between atoms at each time step is calculated. Both are computationally expensive, especially the molecular dynamic simulations but can give a deeper insight into the ablation process and the nature of the ablation products which is considerably different when compared to nanosecond laser ablation. For ultra-short ablation material removal can take place via several mechanisms depending on which part of the temperature-density phase diagram the heated material occupies. Different mechanisms such as vapourisation, fragmentation and phase explosion have all been suggested as possible mechanisms for material removal. A simplified phase diagram is shown in Fig. 2.7 (a) which shows the main T-ρ trajectories the ablated material can evolve along. The binodal line is the solid black line and represents the line of separation between stable and metastable phase states e.g liquid and superheated liquid. The spinodal line

represents the unstable region where two phases can co-exist. At high temperature, but below T_c, liquid and gas states co-exist. At lower temperature within the spinodal region solid and gas phases co-exist. Phase explosion occurs when the T-ρ trajectory crosses the binodal line and enters into the metastable region. As the trajectory approaches the spinodal line the gas phase will start to nucleate and bubbles are formed in the metastable liquid. When the T-ρ trajectory passes within the vicinity of the critical point ($\mathbf{P_c}$ in Fig. 2.7 (a)) phase separation occurs as the trajectory enters the unstable region bounded by the spinodal line. This is known as fragmentation and it leads to decomposition into a heterogeneous clustered phase.
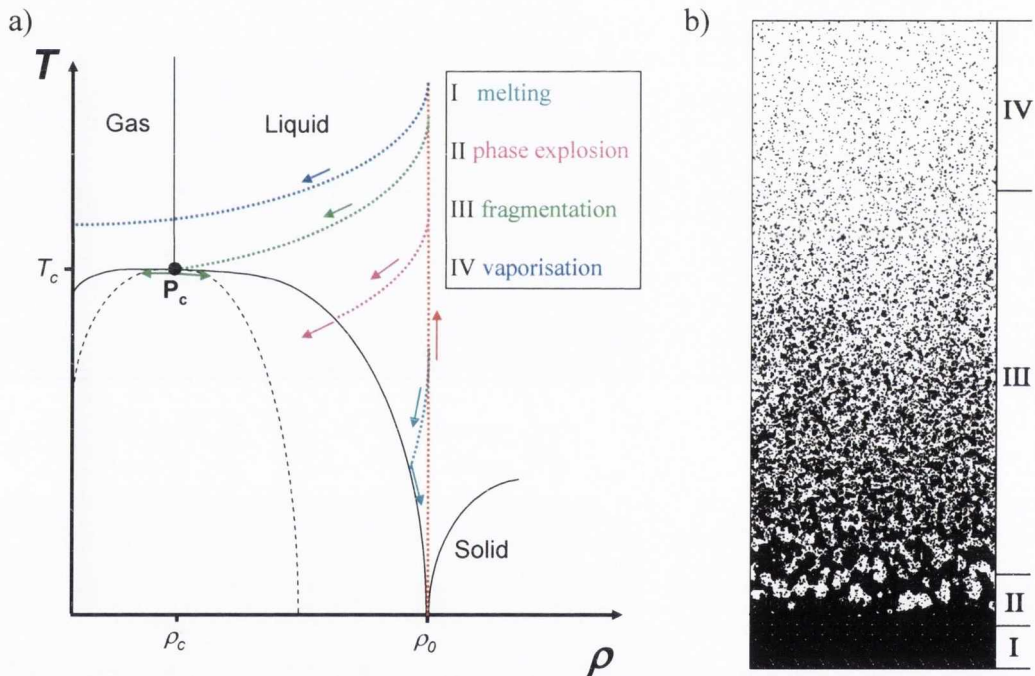
Figure 2.7 (a) Simplified T-ρ phase diagram indicating the main mechanisms taking place during ablation. (b) Molecular dynamics simulation of target decomposition during femtosecond ablation showing how different regions in the target are subject to different decomposition mechanisms. From Ref. [34].

Figure 2.7 (b) is a snapshot of the target decomposition taken for simulated ablation from Ref. 34. In the first situation (I), which corresponds to deep inside the target, the layer is heated so that melting occurs but the trajectory along which the material relaxes does not

26

cross the binodal line that separates the stable and metastable liquid regions so this layer does not undergo decomposition. The second region (II) is heated to a sufficiently high temperature that it relaxes along a trajectory that crosses the binodal into the metastable region. On approaching the spinodal line, nucleation of liquid bubbles occurs and this is known as phase explosion. If the thermodynamic trajectory enters the unstable or metastable regions in the vicinity of the critical point the heated material becomes thermodynamically unstable. This leads to rapid expansion of a super critical fluid and decomposition into a heterogeneous clustered phase ensues. This is known as fragmentation (III). Depending on whether the material trajectory approaches P_c from a higher temperature or from the metastable region between the binode and the spinode the resultant material decomposition can have different behaviour. If the initial temperature is very high the thermodynamic trajectory does not pass close to the critical point and the target decomposes directly into the gas phase (IV). This generally occurs in a thin layer at the target surface. A more detailed discussion on the thermodynamic trajectories and the different effects that can arise can be found in Ref. 28 - 34.

2.2 Ablation plume expansion

The Anisimov model [35, 36] provides a gas dynamical description of the adiabatic phase of expansion of a laser ablation plume in vacuum. For ns laser ablation this adiabatic regime commences at the end of the laser pulse, at which time the ablated material exists as a thin layer of hot vapour on the surface of the target. It is based on a three-dimensional, adiabatic and isentropic self-similar solution of the gas dynamics equations. While the model was developed for the expansion of a neutral gas cloud, it has been successfully used to describe the expansion of both the plasma part [37] and the overall plume (ions and neutrals) [38] for laser produced plasma (LPP) generated by ns laser ablation in vacuum. The expansion is considered to be isentropic when the thermal diffusion is too slow to keep pace with the rate of expansion. Singh *et al.* [39] considered the case where the plume can be considered to be isothermal. By comparing the expansion velocity and the rate of heat diffusion in a LPP, Lunney *et al.* [40] estimated that when the electron temperature is less than ~12 eV the expansion is isentropic. As typical plasma temperatures encountered during laser ablation is, for both ns and fs laser pulses, less than this value, the isentropic model is the correct one to use.

The thickness of the layer of ablated material at the onset of the adiabatic expansion is a critical parameter in the Anisimov expansion model, since it determines the extent to which the final plume is forward-peaked. For ns pulses, vapour ejected from the target during the laser pulse is further heated by absorption of the laser. Thus, apart from some energy transport from the vapour to the target, the end of the laser seems the appropriate choice for the onset of the adiabatic expansion. The initial dimensions of the gas cloud can be estimated as follows. The initial thickness d is approximated as $d \approx c_s \tau_l$ where c_s is the sound velocity and τ_l is the laser pulse duration. The dimensions in the plane of the target are determined by the size of the ablation spot size, which is related to the laser beam spot.

Good agreement with the experimental data seems to support these assumptions [37, 38]. The plume mass can be found by measuring the ablation depth. The plume energy is related to the fraction of the laser energy absorbed in the vapour, but can also be determined from the final expansion velocity.

For femtosecond laser ablation it is not clear how to choose the initial thickness of the ablated material at the commencement of the adiabatic expansion. Indeed, it has been observed that two distinct plumes are produced, a faster-moving atomic plume and a slower nanoparticle one [32, 41, 42, 43]. Looking first at the formation of the atomic plume, we can note that at the end of the laser pulse the material near the target surface has a high electron temperature but the density is still close to the value of the solid. A rarefaction wave will move into the hot material at about the sound velocity and vapour will move away from the target with a maximum velocity of $2c_s/(\gamma-1)$, where the adiabatic index γ has a value of about 1.25 in low temperature plasma [11]. The formation of the vapour layer will cease when the rarefaction wave reaches a depth beyond which the material is not transformed into vapour. This depth corresponds to 10 - 20% of the ablation depth, which will be 10 – 20 nm at a fluence of around 1 J cm^{-2}. For laser fluence around this value the absorbed energy per atom is ~15 eV per atom which gives c_s ~3×10^3 m s^{-1}. Thus the formation time for the vapour layer is 3 - 6 ps and it is 100 – 200 nm thick when the adiabatic expansion begins. Regarding the definition of the parameters which determine the expansion of the nanoparticle plume, the situation is even less clear than for the atomic plume. However, time-resolved images of nanoparticle plume expansion show that they are quite ellipsoidal in shape [42, 43], as is the case in the Anisimov model. The starting thickness of the adiabatic expansion of the NP layer might be estimated as the ablation depth, the appropriate value of γ is not clear at this stage.

The initial plume is considered to be semi-ellipsoidal in shape with principal radii X_0, Y_0 and Z_0, where X_0 and Y_0 are the major and minor radii of the ablation spot and Z_0 is

the thickness of the ablated material as shown in Fig. 2.8. As the expansion proceeds the radii of the ellipsoidal plume front in the *x*, *y* and *z* directions are *X(t)*, *Y(t)* and *Z(t)*.
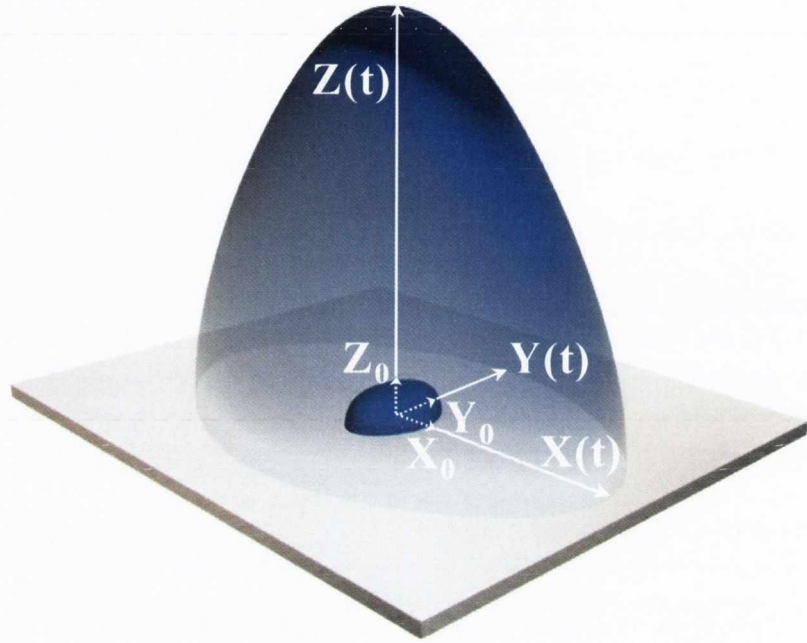
Figure 2.8 Image depicting the initial plasma dimensions and the plasma dimension during expansion.

The gas dynamic equations are the starting point for the Anisimov model and are given below.

$$\frac{\partial \rho}{\partial t} + \nabla \cdot (\rho v) = 0$$

$$\frac{\partial v}{\partial t} + (v \cdot \nabla)v + \frac{1}{\rho}\nabla p = 0 \qquad (2.17)$$

$$\frac{\partial S}{\partial t} + (v \cdot \nabla)S = 0$$

The quantities ρ, v, p, and S are the plume density, velocity, pressure and entropy respectively. The evaporated material is assumed to behave like an ideal gas with adiabatic

exponent $\gamma = \dfrac{c_p}{c_v}$ being the ratio of specific heats at constant pressure (c_p) and constant volume (c_v). A special solution of the gas dynamic equations was utilised by Anisimov which considers flow parameters of the plume that are constant on ellipsoidal surfaces. This solution leads to expressions for the pressure and density profiles in the plume. For an adiabatic gas flow these expressions are:

$$\rho(x,y,z,t) = \frac{M}{I_1(\gamma)XYZ}\left(1 - \frac{x^2}{X^2} - \frac{y^2}{Y^2} - \frac{z^2}{Z^2}\right)^{1/(\gamma-1)}$$

(2.18)

$$p(x,y,z,t) = \frac{E}{I_2(\gamma)XYZ}\left(\frac{X_0 Y_0 Z_0}{XYZ}\right)^{\gamma-1}\left(1 - \frac{x^2}{X^2} - \frac{y^2}{Y^2} - \frac{z^2}{Z^2}\right)^{\gamma/(\gamma-1)}$$

The terms $I_1(\gamma)$ and $I_2(\gamma)$ are described in Ref. 31 and are integrals involving γ and S. The plume propagation is described by the following set of ordinary differential equations:

$$\xi\frac{d^2\xi}{d\tau^2} = \eta\frac{d^2\eta}{d\tau^2} = \zeta\frac{d^2\zeta}{d\tau^2} = \left(\frac{\xi_0\eta_0\zeta_0}{\xi\eta\zeta}\right)^{\gamma-1}$$

(2.19)

where

$$\xi = \frac{X(t)}{X_0}; \ \eta = \frac{Y(t)}{X_0}; \ \zeta = \frac{Z(t)}{X_0}; \ \tau = \frac{t}{t_0}$$

are dimensionless space and time variables. The time parameter t_0 is given by

$$t_0 = \frac{\sqrt{\beta}}{X_0}; \ \beta = (5\gamma - 3)\frac{E_p}{M_p} = (5\gamma - 3)\frac{\varepsilon_p}{m_p}$$

E_p and M_p are the energy and mass of the initial plume (ε_p and m_p are the average energy per particle and mass of the plume particles respectively). It is worth noting that while t_0, and therefore β, define the time scale of the plume expansion, the plume shape does not depend on these parameters. Numerical solution of this equation set yields the temporal variation of the principal radii of the plume front, and therefore the plume shape.

The initial conditions used for Eq. 2.19 are as follows

$$\xi(0) = 1, \quad \eta(0) = \eta_0, \quad \zeta(0) = \zeta_0 \text{ and } \dot{\xi}(0) = \dot{\eta}(0) = \dot{\zeta}(0) = 0.$$

The plume expansion behavior can be illustrated by choosing starting parameters of the same order as for the plasma plume in our ULA experiments, namely $Y_0/X_0 = 0.5$. In this experiment X_0 and Y_0 are approximately 200 and 100 μm respectively. The plume thickness, Z_0 is set to 100 nm, $\varepsilon_p = 15$ eV, m_p = atomic mass of nickel (Ni), and 1.25 is used for γ. Fig. 2.9 (a) shows the evolution of the dimensionless radii. As expected the expansion velocity is greatest in the z direction which is direction of highest pressure gradient in the initial plume. It can also be seen that the plume expansion becomes inertial (constant velocity) for values of τ beyond 5. The plume velocity in each dimension can be found by differentiation.
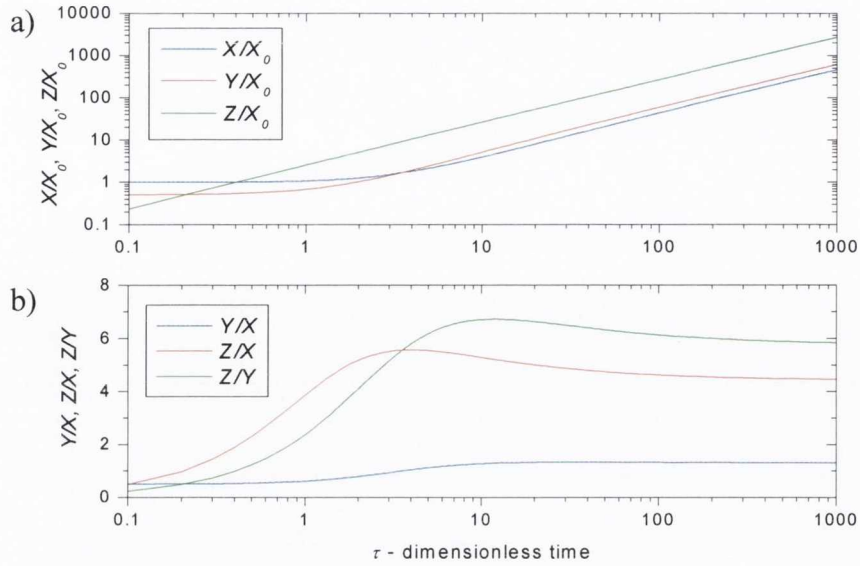
Figure 2.9 (a) Evolution of the dimensional radii as a function of dimensional time. (b) Plume aspect ratios as a function of dimensional time.

Fig. 2(b) shows the aspects ratios ζ/ξ, ζ/η, η/ξ ($\equiv Z/X$, Z/Y, Y/X) as a function of τ. The so-called 'flip over' effect can be seen, where the aspect ratio Y/X is initially less than 1 but changes to a value greater than 1 at late time in the inertial phase. As before, this behavior is a reflection of the ratio of pressure gradients in the x and y directions in the initial plume. The final values of Z/X, Z/Y, Y/X are labeled k_{zx}, k_{zy}, k_{yx} and correspond to the plume length-to-width ratios in the zy and zx planes and the width ratio in the yx plane. The values of k_{zx} and k_{zy} determine the angular spread of the particle flux on a detector at large distance. Figure 2.10 shows plume k values calculated as a function of normalized plume thickness, for $Y_0/X_0 = 0.5$ and for different γ values. It can be seen that if the initial thickness is increased with respect to the in plane dimension the plume aspect ratio is reduced. The plume shape is seen to depend strongly on γ.
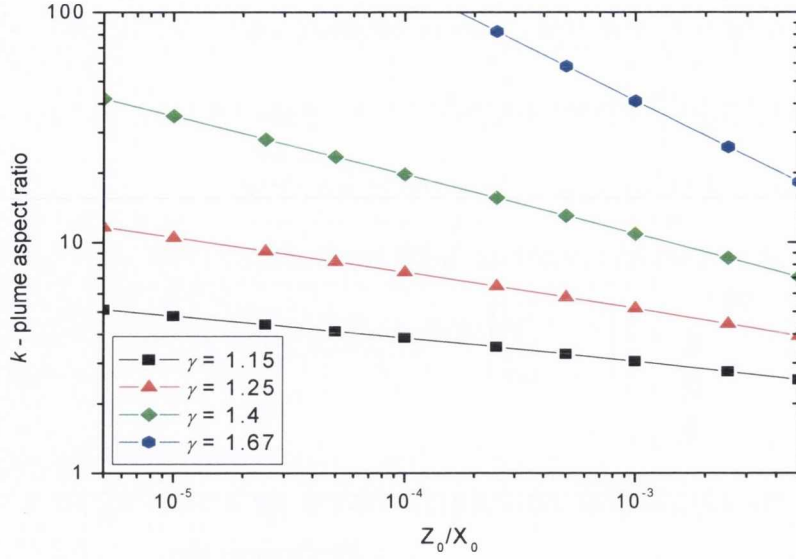
Figure 2.10 Calculation of the plume aspect ratio as a function of the normalised initial plume thickness for several values of γ.

The equation describing the particle flux on to a detector positioned at (y, z) in the yz plane and oriented to face the ablation spot is;

$$j(y,z,t) = (N/I_1(\gamma))(XYZ)^{-1}\left[1-\left(\frac{y}{Y}\right)^2-\left(\frac{z}{Z}\right)^2\right]^{\frac{1}{\gamma-1}}\left(v_y^2+v_z^2\right)^{\frac{1}{2}} \qquad (2.20)$$

where N is the total number of particles in the plume, I_1 is a constant which depends on the value of γ [35] and v_y and v_z are the components of the local plume velocity. The equation describes the signal recorded on the ion probe operating in time-of-flight mode. It also describes how the TOF signal depend on the angle θ measured away from the target normal, where $\sin\theta = y/z$. This equation can be integrated to yield the angular distribution and its associated full width half maximum of the deposition on hemispherical and plane surfaces. For the deposition on a hemisphere [37] the distribution is:

34

$$F(\theta) = F(0)\left(1 + \tan^2 \theta\right)^{3/2}\left(1 + k_{zy}^2 \tan^2 \theta\right)^{-3/2} \tag{2.21}$$

while for a plane it is:

$$F(\theta) = F(0)\left(1 + k_{zy}^2 \tan^2 \theta\right)^{-3/2} \tag{2.22}$$

The full-width-half-maximum (FWHM) for hemispherical and planar deposition can be found from Eq. 3 and 4 respectively and are as follows [38]:

$$\Delta\theta = 2\arctan\sqrt{\frac{2^{2/3} - 1}{k_{zy}^2 - 2^{2/3}}}$$

$$\tag{2.23}$$

$$\Delta\theta = 2\arctan\sqrt{\frac{2^{2/3} - 1}{k_{zy}^2}}$$

Similar expressions can be derived for the angular distribution of deposition in the other plane (xz).

A computer program was written in Mathematica to solve Eq. 2.19 for user input values of X_0, Y_0, Z_0, γ and ε_p and is shown in Appendix A. The program calculates the plume front position as a function of time, the plume aspect ratios, the final ratio, in both expansion planes, when the expansion has become inertial and the time of flight profile of the plume.

35

2.3 Optical properties of metal nanostructured films

Nanostructured films of silver (Ag) and gold (Au) exhibit interesting optical properties due to the resonant excitation of surface plasmons. This excitation occurs when a metal is subject to electromagnetic radiation with frequency equivalent to the plasma frequency of the free electron ensemble in the metal. For Ag and Au this resonance occurs in the visible region of the spectrum. For nanoparticles and nanostructured films the effect is more pronounced as confinement of charge to nanometer length scales leads to an enhancement of the local electric field. The optical properties of Ag and Au nanoparticles are relatively well known. For nano Ag the surface plasmon resonance (SPR) occurs between 400 – 500 nm and for Au is between 550 - 650 nm. The resonance peak position and shape are dependent on the size and shape of the nanoparticles and also their average spacing. Due to the relevant ease of measuring the SPR in thin and nanostructured films using UV-Vis spectrophotometry, it can be of use to infer structure size and shape as well as the surface coverage. To do this, a detailed model of the light interaction with a metallic nanostructured surface including substrate effects is required. Such modeling is beyond the scope of this thesis and even the simpler case of light interaction with a spherical nanoparticle is a complex topic. Therefore to describe the optical properties of nanostructured films grown by pulsed laser ablation later in chapter 6 a relatively simple model is used that can predict the main features of the optical response. This model uses the standard Fresnel equations for reflection, transmission and absorption but treats the film as a composite layer with an effective dielectric function. The effective refractive index is calculated from an effective medium theory (of which several exist) and averages the wavelength dependent optical response over the composite film. The optical model used is described below and a MathCAD routine was constructed to calculate the optical response. This is given in Appendix B.

2.3.1 Optical models

The optical properties of thin films are well known and described in standard texts by Heavens [44] and Born and Wolf [45]. The interaction of electromagnetic radiation at an interface is described by the Fresnel coefficients for transmission and reflection. For normal incidence these are as follows:

$$r_{12} = \frac{n_1 - n_2}{n_1 + n_2}, \quad r_{23} = \frac{n_2 - n_3}{n_2 + n_3}, \quad t_{12} = \frac{2n_1}{n_1 + n_2}, \quad t_{23} = \frac{2n_2}{n_2 + n_3} \tag{2.24}$$

n_1, n_2, n_3 are the refractive indices of the three mediums, n_1 represents ambient, n_2 the thin film and n_3 the substrate refractive index respectively. The reflectance, transmittance and absorbance can then be found from the following equations,

$$R = \left(\left| \frac{r_{12} + r_{23} \cdot \exp(-2i\delta)}{1 + r_{12} \cdot r_{23} \cdot \exp(-2i\delta)} \right| \right)^2$$

$$T = \left(\left| \frac{t_{12} \cdot t_{23} \cdot \exp(-i\delta)}{1 + r_{12} \cdot r_{23} \cdot \exp(-2i\delta)} \right| \right)^2 \tag{2.25}$$

$$A = -\log(T)$$

where $\delta = \frac{2\pi}{\lambda} n_2 d$ is the phase difference induced as light travels through an absorbing film of thickness d. These formulae can be used to calculate the optical response of a thin film on a non - absorbing substrate. However for multi-component and nanostructured thin films the refractive index is unknown. To simulate the optical properties of composite thin films, approximate methods in the form of effective medium theories can be used [46, 47] to calculate an average dielectric function which takes into account the dielectric functions

of each component of the film. This average dielectric function is then used in conjunction with the previous set of equations to calculate the optical response of these types of films. Two widely used effective medium theories are the Maxwell-Garnett [48] and Bruggeman theory [49]. The Maxwell-Garnett theory considers a two component layer. One component is considered as spherical inclusions in a host medium of the second component and the volume fraction of the inclusions is small. Figure 2.11 demonstrates this idea. This framework will be applied to the nanostructured films in this thesis. Bruggemann on the other hand considered a layer where two or more components of similar volume fraction are present.
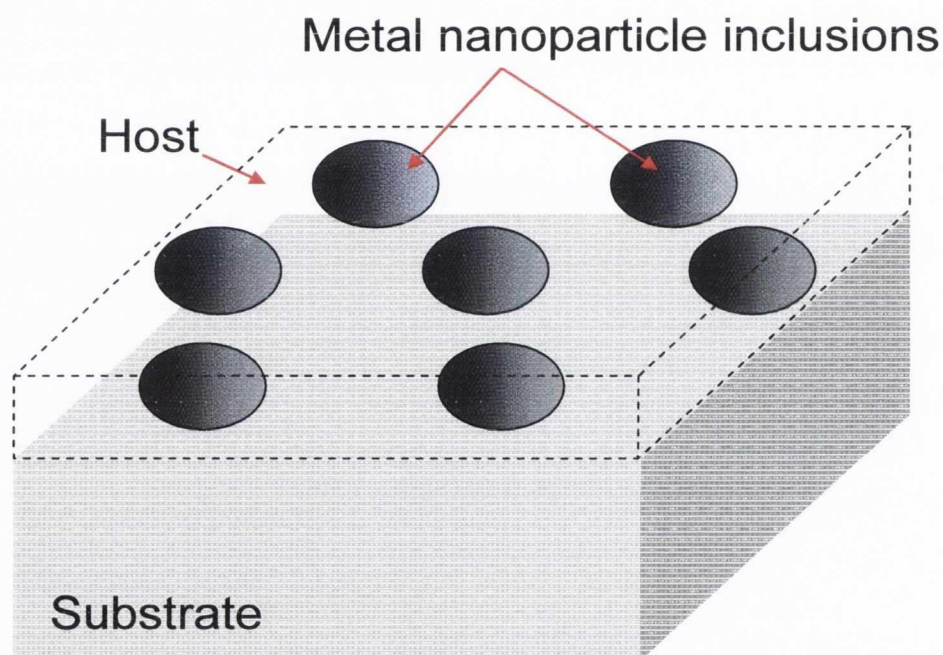
Figure 2.11 Composite thin film in the Maxwell Garnett framework. The film is made up of spherical metal inclusions in a host material.

The Maxwell-Garnett expression for calculating an effective dielectric function, ε_{eff}, is given in Eq. 2.26. The equation relates ε_{eff} to the bulk dielectric function of the host, ε_0, and spherical metal inclusions, ε_m.

$$\left(\frac{\varepsilon_{eff} - \varepsilon_0}{\varepsilon_{eff} + 2\varepsilon_0} \right) = f_1 \left(\frac{\varepsilon_m - \varepsilon_0}{\varepsilon_m + 2\varepsilon_0} \right) \tag{2.26}$$

In the above equation, f_1 is the volume fraction of inclusions and solving for the average dielectric coefficient ε_{eff} gives the following:

$$\varepsilon_{eff} = \varepsilon_0 \left(1 + \frac{3 f_1 \beta}{1 - f_1 \beta} \right)$$

$$\beta = \left(\frac{\varepsilon_m - \varepsilon_0}{\varepsilon_m + 2\varepsilon_0} \right)$$

(2.27)

There are a number of shortcomings of the Maxwell-Garnett theory such as asymmetry in results when the roles of ε_0 and ε_m are interchanged and the fact that a percolation threshold cannot be estimated using this theoretical treatment. In general, effective medium theories are unable to predict a percolation value, with the Bruggemann formalism being an exception. For a composite layer where the inclusions have a similar volume fraction to the host material the Bruggeman framework is the more appropriate model to use. The generalised Bruggeman formula is

$$\sum_i f_i \left(\frac{\varepsilon_i - \varepsilon_{eff}}{\varepsilon_i + 2\varepsilon_{eff}} \right) = 0$$

(2.28)

where ε_i and f_i are the dielectric function and volume fraction of the i-th component. Solving the Bruggeman equation for a two component composite layer ($i = 2$) gives

$$\varepsilon_{eff} = \frac{1}{4}\left(\gamma + \sqrt{\gamma^2 + 8\varepsilon_1\varepsilon_2}\right)$$

$$\gamma = (3f_1 - 1)\varepsilon_1 + (3f_2 - 1)\varepsilon_2 \qquad (2.29)$$

$$f_1 + f_2 = 1$$

These equations can be used in the same way as the Maxwell-Garnett equation to simulate the optical response of composite films. The Bruggeman equation can also be used to calculate a percolation threshold and the asymmetry that is present in the Maxwell-Garnett formulation is absent here.

The exact calculation of light interaction with nanosized metal spheres is called Mie theory [50]. The theory is very complex but a simple result can be used when working within the dipole approximation where the particle size is assumed to < 20 nm (a few percent of wavelength of light) and are separated such that neighbouring particles are non-interacting. The equation for the extinction cross section σ_{ext} and transmission, T of a nanostructured thin film of equivalent thickness d in the Mie framework is

$$\sigma_{ext} = \left(\frac{9\omega}{c}\right)\varepsilon_m^{3/2} V_0 \left[\frac{\varepsilon_2}{\left(\varepsilon_1 + 2\varepsilon_0\right)^2 + \varepsilon_2^2}\right]$$

$$(2.30)$$

$$T = I/I_0 = \exp\left(-N\sigma_{ext}\right) = \exp\left(-d\frac{\sigma_{ext}}{V_0}\right)$$

where ε_0 is the host dielectric function, ε_1 and ε_2 are the real and imaginary part of the dielectric function of the metal nanoparticles. V_0 is the volume of the metal spheres, ω and c is the angular frequency and speed of light respectively. I and I_0 are the transmitted and incident intensity and N is the number of nanoparticles per unit area. The above equation becomes invalid as the size of the nanoparticles exceeds 10% of the wavelength of light

($\approx$50 nm). The equation does not account for the actual size or distribution of sizes of the nanoparticles but instead considers an equivalent thickness of deposited metal that forms randomly orientated, non interacting spherical particles.

2.3.2 Maxwell-Garnett calculations

For comparison to experiment and to interpret data, the Maxwell-Garnett theory was chosen as it is the closest model to our physical situation. In what follows, the calculation of the optical response of a nanoparticle Ag will be outlined. The extent of its applicability and the model failures will also be discussed. The starting point is the construction of the effective dielectric function of our composite layer. The bulk dielectric function for Ag can be found from tabulated data. Using Eq. 2.27, taking the volume fraction $f = 0.1$ and considering the host medium as ambient ($\varepsilon_0 = 1$) we can construct an effective dielectric coefficient. The real and imaginary parts of the effective dielectric function as well as the bulk function for Ag are plotted in Fig. 2.12. Using the parameters above we have simulated a layer consisting of spherical Ag nanoparticles that account for 10% of the overall volume. The components of the effective dielectric function are significantly different to the bulk function so that the optical properties of the composite layer will be very different to a bulk thin film. If we take the effective dielectric function, derive the wavelength dependent refractive index and insert into Eq. 2.25 we can find the transmission and then the absorption of the nano-composite layer. For this calculation n_1 is taken to be ambient (i.e. = 1), n_2 is the effective refractive index ($n_2 = \varepsilon_{eff}$) of the composite layer and n_3 is the substrate refractive index and for our example we will use glass ($n_3 = 1.5$).
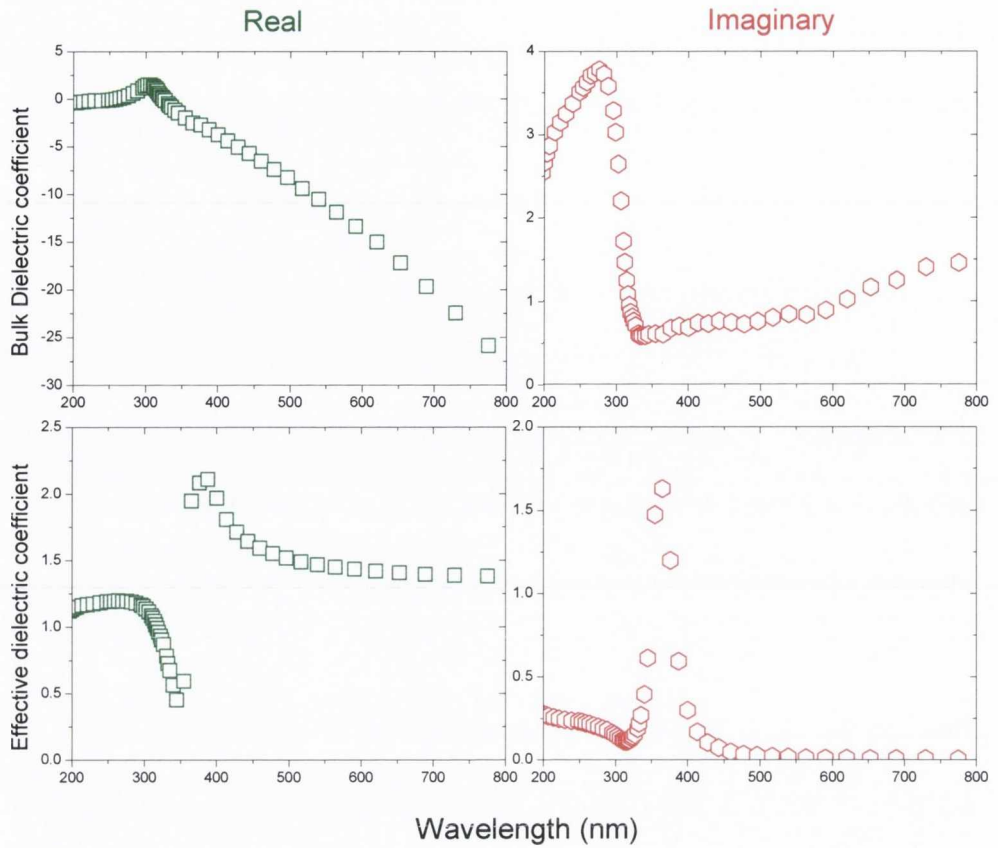
Figure 2.12 Bulk and effective dielectric coefficients calculated from Maxwell Garnett theory.

Setting the volume fraction to be 0.1 and considering an equivalent film thickness of 1 nm gives a composite layer thickness of 10 nm. Herein, the optical absorption can be found. This is shown in Fig. 2.13. A large peak is observed in the absorption spectrum around 360 nm indicating that the simplistic approach of the Maxwell - Garnett theory can include the surface plasmon resonance feature observed for nanostructured metal films and particles.

Figure 2.13 Calculated absorption and transmission for 10 nm thick composite layer containing 1 nm equivalent thickness of Ag.
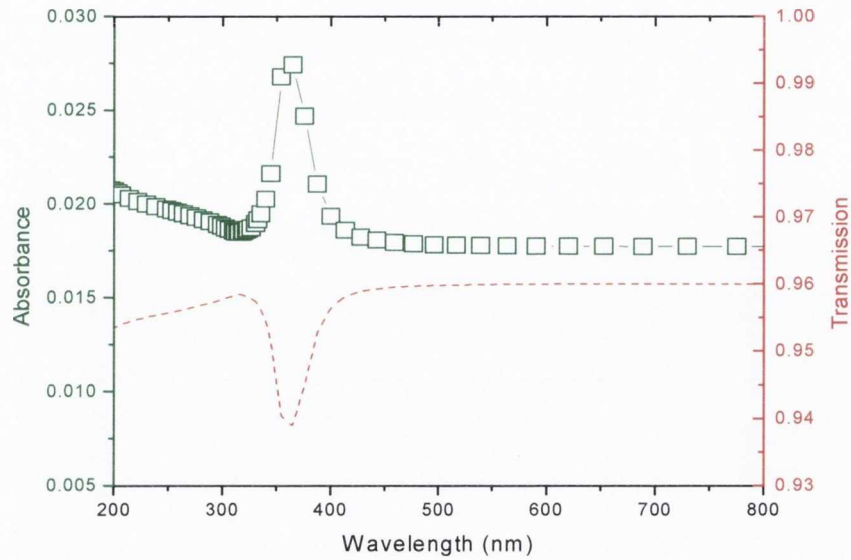
It is of interest to see how the predicted SPR peak behaves with changing the volume fraction and film thickness. In Fig. 2.14 the volume fraction is varied for a 1 nm equivalent thickness. The thickness of the composite layer will change accordingly. Also included is a spectrum for equivalent thickness of 2.5 nm and a volume fraction value of 0.25 that sets the layer thickness the same as the $f = 0.1$ case. From this plot it can be seen that the peak position depends on the volume fraction of inclusions in the layer. As f is increased for 1 nm equivalent Ag, the SPR peak shifts to longer wavelengths and increases in magnitude even though the overall layer thickness is reduced. Keeping the composite layer thickness constant and increasing the volume fraction by increasing the quantity of Ag in the layer also shifts the absorption peak but the magnitude is increased. For equal f the peak position remains the same but the absorption is increased for a larger layer thickness.
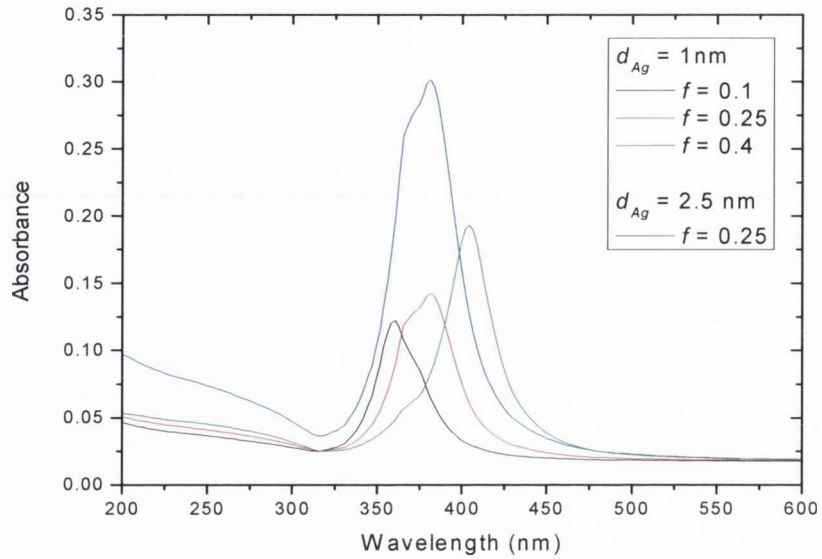
43

Figure 2.14 Change in calculated absorption as the volume fraction and equivalent thickness of Ag is changed.

Running the calculation routine (Appendix B) a few other aspects are worth noting. For different host media, i.e. changing ε_0, there will be a change in the peak wavelength of the SPR. If ε_0 is increased the SPR peak shifts to longer wavelengths. This can be seen in Fig. 2.15 where a comparison is shown for a Ag film of 1 nm equivalent thickness, $f = 0.1$ for vacuum and glass host media. In reality, metal nanoparticles on a substrate will be in contact with both environments so that behaviour will be an average of the two. The average case is also shown in Fig. 2.15. This behaviour has been observed experimentally [51] and shows the plasmon resonance can be tuned depending on the host environment.
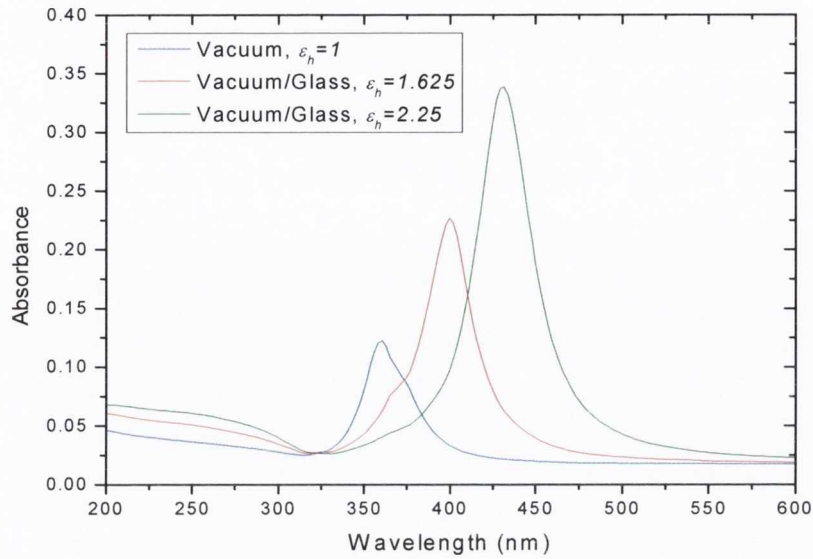
Figure 2.15 Change in calculated absorption as the host medium is changed.

Fig. 2.16 (a) compares a MG calculation for $f = 1$ and 1 nm Ag to a calculation using the bulk refractive indices and a film thickness of 1 nm. Figure 2.16 (b) also shows a comparison of a Maxwell Garnett calculation for 1 nm Ag at low f and compares with a Mie calculation, using Eq. 2.30, for a 1 nm equivalent thickness Ag film. To further verify the consistency of the Maxwell Garnett model we can test its behaviour as $f \rightarrow 1$ which corresponds to a bulk film and for $f \rightarrow 0$ which should correspond to the Mie result in the dipole approximation where the nanoparticles are assumed non interacting.
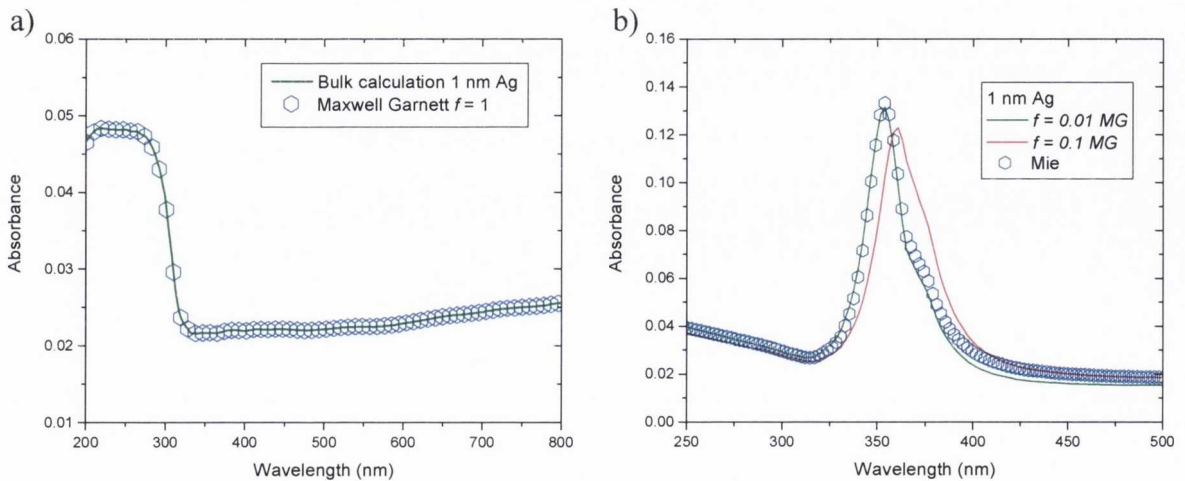
Figure 2.16 (a) Comparison of Maxwell Garnett theory to bulk and (b) Mie calculations for large and small volume fractions respectively.

It is clear, that although the aforementioned drawbacks exist, in both cases the Maxwell Garnett model is successful in replicating the Mie and bulk results. The asymmetry in the theory will be particularly evident for $\varepsilon_m/\varepsilon_0 \gg 1$ [46]. In spite of its shortcomings, this model easy to use and allows one to quickly generate approximate optical spectra to compare with the measurements for nanostructured films grown by PLD.

2.4 References

[1] S. Amoruso, R. Bruzzese, N. Spinelli and R. Velotta, *J. Phys. B: At. Mol. Opt. Phys.*, **32** (1999) R131–R172.

[2] *Thermophysical properties of high temperature solid materials*, Y. S. Touloukian, Collier-MacMillan (1967)

[3] V. N. Tokarev and A. F. H. Kaplan, *J. Appl. Phys.*, **86**, 5 (1999) 2836 - 2845

[4] J. G. Lunney and R. Jordan, *Appl. Surf. Sci.*, **127 - 129** (1998) 941 – 946

[5] S. Amoruso, *Appl. Phys. A*, **69** (1999) 323-332

[6] B. Wu and Y. C. Shin, *J. Appl. Phys.*, **99**, 084310 (2008)

[7] C. R. Phipps, Jr., T. P. Turner, R. F. Harrison, G.W. York, W. Z. Osbourne, G. K. Anderson, X. F. Corlis, L. C. Haynes, H. S. Steele, K. C. Spicochi and T. R. King, *J. Appl. Phys.*, **64**, 3 (1988) 1083 – 1096

[8] *Conduction of Heat in Solids*, H. S. Carslaw and J. C. Jaeger, Oxford (1959)

[9] R. Jordan and J. G. Lunney, *Appl. Surf. Sci.*, (1998)

[10] M. S. Qaisar and G. J. Pert, *J. Appl. Phys.*, **94**, 3 (2003) 1468 - 1477

[11] *Physics of Shock Waves and High Temperature Hydrodynamic Phenomena*, Y. B. Zel'dovich, Y. P. Raizer, Dover, New York, (2002)

[12] NIST spectral database; http://physics.nist.gov/PhysRefData/ASD/index.html

[13] *The Theory of Atomic Structure and Spectra*, R. D. Cowan, University of California Press (1981)

[14] M. E. Sherrill, R. C. Mancini, J. Bailey, A. Filuk, B. Clark, P. Lake and J. Abdallah Jr., *Phys. Rev. E*, **76**, 056401 (2007)

[15] *Spectrophysics: Principles and Applications*, A. P. Thorne, U. Litzen and S. Johansson, Springer (1999)

[16] D. J. Heading, G. R. Bennett, J. S. Wark and R. W. Lee, *Phys. Rev. Lett.*, **74**, 18 (1995) 3616 – 3619

[17] A. N. Mostovych, L. Y. Chun, K. J. Kearney, D. Garrenn, C. A. Iglesias, M. Klapisch and F. J. Rogers, *Phys. Rev. Lett.*, **75**, 8 (1995) 1530 – 1533

[18] H. K. Chung, M. H. Chen, W. L. Morgan, Y. Ralchenko and R. W. Lee, *High Ener. Dens. Phys.*, **1**, (2005) 3 - 12

[19] *Principles of Plasma Spectroscopy*, H. R. Griem, Cambridge University Press (2005)

[20] *Spectral Line Broadening by Plasmas*, H. R. Griem, Academic Press Inc. (1974)

[21] *Atomic Physics in Hot Plasmas*, D. Salzman, Oxford University Press (1998)

[22] http://www.prism-cs.com/Software/PrismSpect/PrismSPECT.htm

[23] R. W. Lee, J. T. Larsen, *J. Quant. Spect. Rad. Transf.*, **56** (1996) 535

[24] S. I. Anisimov, B. L. Kapelovich and T. L. Perel'man, *Zh. Eksp. Teor. Fiz*, **66** (1974) 776

[25] D. S. Ivanov and L. V. Zhigilei, *Phys. Rev. B*, **68**, 064114 (2003)

[26] S. Nolte, C. Momma, H. Jacobs, A. Tunnermann, B. N. Chichkov, B. Wellegehausen and H. Welling, *J. Opt. Soc. Am. B*, **14**, 10 (1997) 2716 - 2722

[27] K. Vestentoft and P. Balling, *Appl. Phys A*, **84** (2006) 207 - 213

[28] M. E. Povarnitsyn, T. E. Itina, M. Sentis, K. V. Khishchenko and P. R. Levashov, *Phys. Rev. B*, **75**, 235414 (2007)

[29] A.M. Komashko, M.D. Feit, A.M. Rubenchik, M.D. Perry, and P.S. Banks, Appl. Phys. A **69**, S95 (1999)

[30] K. Eidmann, J. Meyer-ter-Vehn, and T. Schlegel and S. Huller, *Phys Rev. Lett.*, **62**, 1202 (2001)

[31] F. Vidal, T. W. Johnston, S. Laville, O. Barthélemy, M. Chaker, B. Le Drogoff, J. Margot, and M. Sabsabi, *Phys Rev. Lett.*, **86**, 2573 (2000)

[32] S. Amoruso, R. Bruzzese, X. Wang, N. N. Nedialkov and P. A. Atanasov, *J. Phys. D: Appl. Phys.*, **40**, 331-340 (2007)

[33] C. Cheng and X. Xu, *Phys. Rev. B*, **72**, 165415 (2005)

[34] D. Perez and L. J. Lewis, *Phys. Rev. Lett.*, **89**, 255504 (2002)

[35] S. I. Anisimov, D. Bauerle and B. S. Luk'yanchuk, *Phys. Rev. B*, **48**, 12076 (1993)

[36] S. I. Anisimov, B. S. Luk'yanchuk and A. Luches, *Appl. Surf. Sci.*, **96-98**, 24-32 (1996)

[37] T. N. Hansen, J. Schou and J. G. Lunney, *Appl. Phys. A*, **69**, S601-S604 (1999)

[38] B. Toftmann, J. Schou and J. G. Lunney, *Phys. Rev. B*, **67**, 104101 (2003)

[39] R. K. Singh and J. Narayan, *Phys. Rev. B* **41**, 8843 (1990)

[40] J.G. Lunney, B. Doggett and Y. Kaufman, *J. Phys.: Conf. Ser.* **59**, 470-474 (2007)

[41] S. Amoruso, R. Bruzzese, N. Spinelli, R. Velotta, M. Vitiello, X. Wang, G. Ausanio, V. Iannotti and L. Lanotte, *Appl. Phys. Lett.*, **84**, 4502 (2004)

[42] S. Amoruso, R. Bruzzese, C. Pagano and X. Wang, *Appl. Phys. A*, **89**, 1017 – 1024 (2007)

[43] S. Amoruso, R. Bruzzese, X. Wang and J. Xia, *Appl. Phys. Lett.*, **92**, 041503 (2008)

[44] *Optical Properties of Thin Solid Films*, O. S. Heavens, Dover (1955)

[45] *Principles of Optics: Electromagnetic Theory of Propagation, Interference and Diffraction of Light*, M. Born and E. Wolf, Cambridge University Press (1997)

[46] *Effective Medium Theory: Principles and Applications*, T. C. Choy, Oxford University Press (1999)

[47] D. E. Aspnes, *Thin Solid Films*, **89** (1982) 249-262

[48] J. C. Maxwell-Garnett, *Philos. Trans. R. Soc. London, Ser. A*, **203**, (1904) 385

[49] D. A. G. Bruggeman, *Ann. Phys. (Liepzig)*, **24**, 5 (1935)

[50] G. Mie, *Ann. Phys. (Liepzig)*, **25** (1908) 377

[51] G. Xu, M. Tazawa, P. Jin and S. Nakao, *Appl. Phys. A*, **80** (2005) 1535 - 1540

Chapter 3: Experimental and computational techniques

The purpose of this chapter is to describe the experimental equipment and to outline the computational techniques used throughout this thesis. The laser systems, vacuum chambers and laser beam delivery optics are discussed. Optical spectroscopy and Langmuir probes are described as these are the two main plasma diagnostic techniques used in this thesis. Some surface and thin film characterisation techniques were also utilised for analysing the ablation deposits and laser irradiated surfaces.

To calculate the emission and absorption properties of laser produced plasma a spectral synthesis code is required and this is also discussed in this section.

3.1 Lasers and vacuum systems

To carry out laser ablation in vacuum, a pulsed laser source of sufficient energy to ablate when focused onto a solid target is required. For a vacuum environment, ablation is carried out inside a sealed chamber evacuated using a pump. The laser pulse is focused onto the ablation target inside the chamber. Over the course of this work, three different laser systems and two different vacuum systems were used. The laser systems are detailed in Table 3.1.

Laser System	Wavelength (nm)	Pulse duration @ FWHM	Max. Energy (mJ)
Nd:YAG: Continuum, Surelite I	1064	6 – 15 ns	330
	532	6 – 15 ns	150
	355	6 – 15 ns	60
KrF: Lambda Physik, LPX 105	248	26 ns	180
Nd:Glass: Light Conversion Ltd., Twinkle	1054	0.9 - 1 ps	2
	527	250 - 300 fs	0.8

Table 3.1 Operating parameters for various laser systems used throughout this research.

The vacuum system used for nanosecond laser ablation consisted of a cylindrical stainless steel chamber that utilised Kwik Fit (KF) flanges and had a number of KF 40 and 50 ports

51

for access. The laser entry window was comprised of quartz with good transmission from UV to IR. The chamber volume was approximately 20 l and a 50 l s^{-1} Pfeiffer Balzers (TPH050) turbo-molecular pump, backed by a rotary vane pump, was used to evacuate the system. The chamber pressure was measured using an Edwards Pirani gauge for high pressure (> 10^{-2} mbar) and a Balzers Penning gauge at lower pressure down to a base pressure of around 5x10^{-6} mbar. The ablation target was mounted on a rotating arm in vacuum that was driven externally by a continuous motor. The laser pulses were imaged onto the target surface at an angle of 45°. An imaging setup consisting of a 20 cm quartz lens and an aperture was used. The aperture was placed 60 cm from the lens and its image was formed, at 30 cm, on the target inside the vacuum chamber. The aperture selected a uniform section of the beam and allowed for a well defined on target laser spot with a demagnification of two. By varying the aperture size the spot size could also be changed. This setup was used for both nanosecond lasers systems.

The vacuum system used for the femtosecond laser ablation experiment was of similar size to the nanosecond chamber but contained conflat flange (CF) fittings. A 300 l s^{-1} turbo pump was used to evacuate this chamber to a base pressure of 1x10^{-7} mbar and the pressure was measured using a wide range Pfeiffer vacuum gauge. The laser was focused onto the target surface using a 20 cm focal length quartz lens and the target was positioned at the beam focus. The analysis of laser spot and calculation of the laser fluence in this geometry is described in chapter 5. The target was rotated in vacuum by a set of in vacuum stepper motors.

3.2 Optical spectroscopy

Atoms and ions present in plasma can emit and absorb photons. The amount of emission and absorption can be related to the density and temperature of the different species within the plasma. The emission and absorption mechanisms that can take place in plasma have been discussed in chapter 2.

For measurement of optical emission from laser produced plasma a system of optics and mirrors was used to image the light emission from the plasma to the entrance slit of an imaging spectrometer. The spectrometer dispersed the light allowing for a spectrally resolved measurement of the plasma emission which was recorded on an intensified charged coupled device camera (ICCD). The spectrometer used was an Oriel MS260i imaging spectrometer which was coupled to an Andor ICCD camera. The Spectrometer employed an asymmetrical in plane Czerny-Turner configuration which is shown in Fig. 3.1. The optical configuration used in the spectrometer images the slit, 1:1 in the horizontal direction and 1:1.6 magnified in the vertical plane onto the exit slit plane where the ICCD camera is placed.
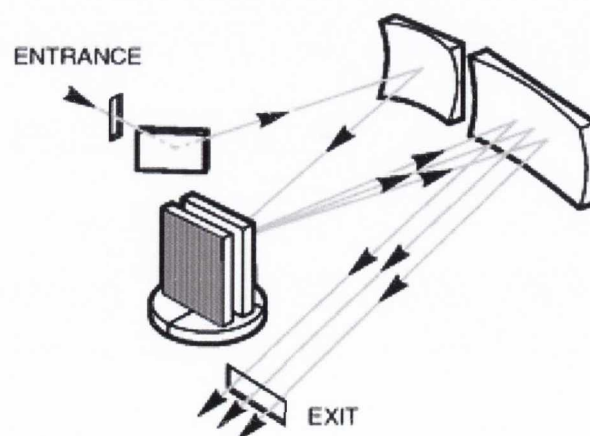

Figure 3.1 Optical configuration used in the Andor MS260i imaging spectrometer.

The entrance slit to the spectrometer was 3mm x 50 μm in dimension and the dispersive element used was a ruled diffraction grating with a line density of 300 mm^{-1}. The blaze wavelength of the grating was 500 nm, making it suitable for measurements in the UV and visible region but not for measurements in the IR. The Andor ICCD camera (DH 520 18F) used to record wavelength dispersed spectra consisted of an array of 1024 x 256 pixels of size 26 x 26 μm. The minimum sampling (gate) time that could be set on the camera was 8 ns and the delay between measurement and some reference time zero was set using a Standford delay generator. The theoretical maximum spectral resolution obtained using the above slit width and line density is about 0.7 nm.

The imaging optical system was used in experiments to image the plasma emission onto to spectrometer slit to deliver light into the spectrometer. The imaging optical system is shown in Fig. 3.2.
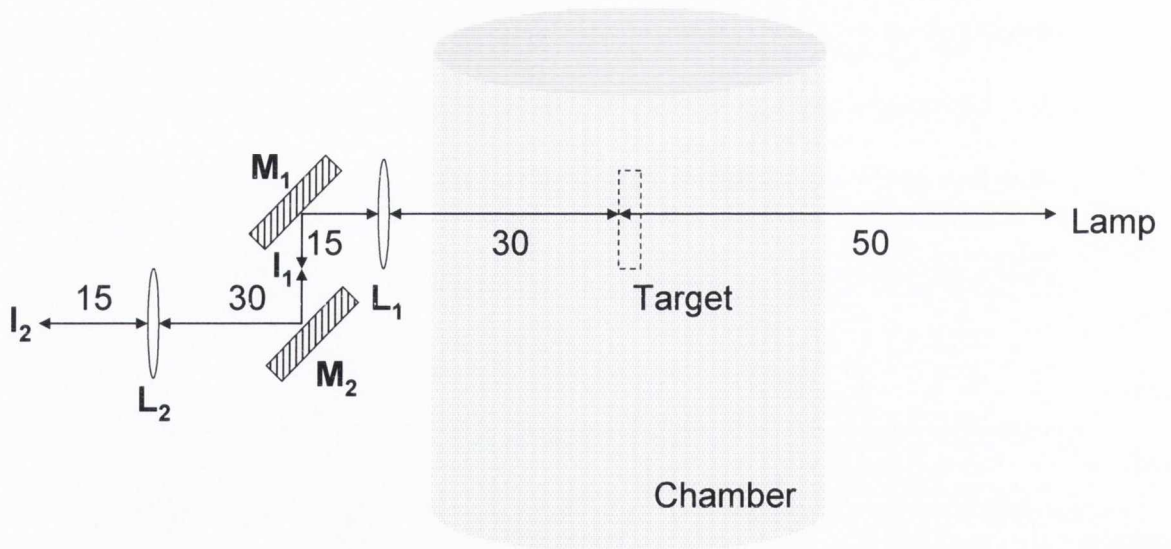

Figure 3.2 Optical imaging setup for light collection from plasma. All distances are in centimetre units.

In the above diagram above M_1 and M_2 are aluminium mirrors of 1" diameter, L_1 and L_2 are 10 cm focal length lenses also of 1" diameter. L_1 is quartz plano - convex lens while L_2 is an achromatic lens made of glass. Originally the system was designed to measure down to the KrF wavelength of 248 nm. The achromatic lens L_2 was inserted to correct for aberration effects one made of quartz was not available at the time the experiments were

54

carried out. This increased the minimum wavelength the system can measure at, which was approximately 325 nm. Figure 3.3 shows typical spectra for the calibration of the wavelength (a) and intensity (b) in the region 350 – 590 nm.
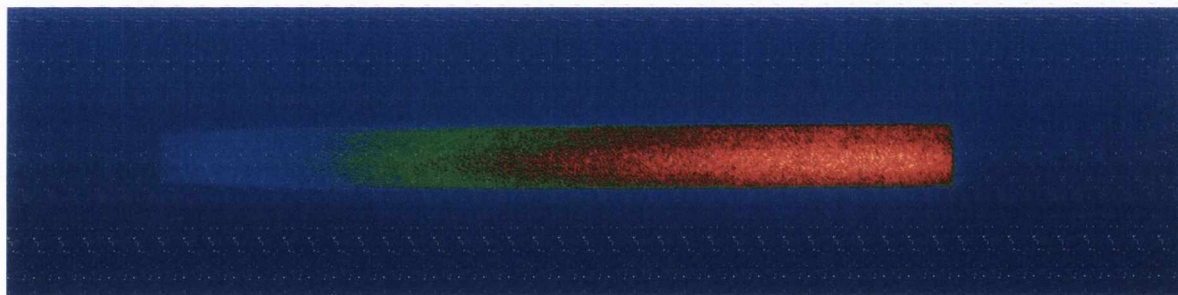
(a)

(b)

Figure 3.3 (a) ICCD image of the spectral emission measured from a mercury lamp in the spectral range 350 – 590 nm. The well known transitions at 365, 405, 408, 436, 546, 577 and 579 are seen. (b) ICCD image of the broadband spectral emission from the quartz tungsten halogen lamp.

I_1 and I_2 are the image positions of L_1 and L_2 respectively and the spectrometer entrance slit was placed at I_2. The image system used resulted in an overall de-magnification of 4 of the emission area (at target surface) onto the spectrometer slit. Losses occur at lens L_2 and the half - angle subtended to the entrance slit is around 4°. This value is less than the spectrometer acceptance half - angle of 7°. The solid angle subtended to the plasma by the optical system is 0.0014 sr and the spatial resolution is approximately 100 μm.

Figure 3.2 also shows the position of the spectral lamp that was used to make calibrated measurements of the absolute spectral radiance emitted from the plasma. To calibrate the wavelength scale of the spectrometer in the UV and visible region, a mercury

lamp and helium-neon laser operating at 632.8 nm were used. For calibration of the emission intensity a quartz tungsten halogen lamp (Oriel QTH 6333, 100 W) with a well defined output was used.
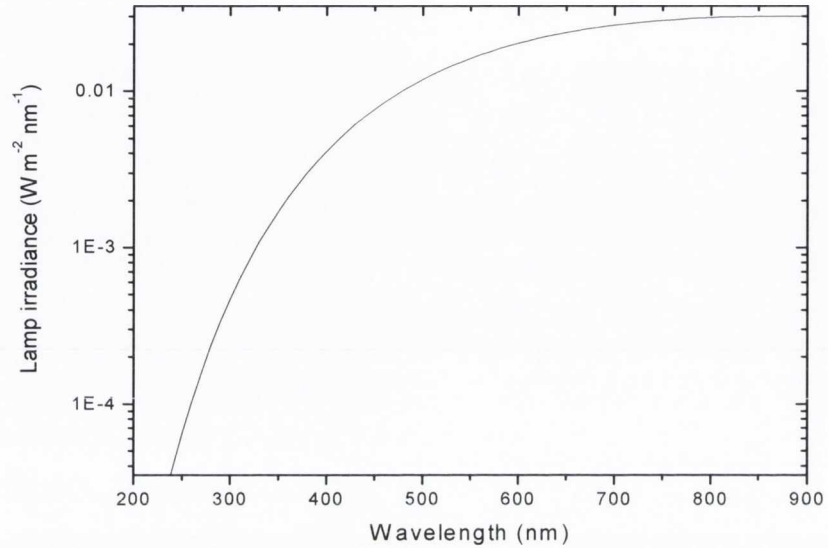

Figure 3.4 Irradiance at 50 cm of quartz tungsten halogen lamp that was used to calibrate the spectrometer

The calibration lamp emission profile is blackbody-like with a well known spectral irradiance $E(\lambda)$ (W m^{-2} nm^{-1}), at 50 cm from the emission source. The solid angle subtended by the calibration lamp is smaller than the solid angle of the collection optics. The output from the lamp (at 50 cm) is described by the following equation and shown in Fig. 3.4.

$$E(\lambda) = A_{fit} \cdot 10^{-9} \frac{2\pi hc^2}{\lambda^5} \frac{1}{e^{\frac{hc}{\lambda kT}} - 1} \tag{3.1}$$

In Eq. 5.1 $A_{fit} = = 7.64 \times 10^{-6}$ is a fitting constant and $T = 3317.8$ K is the blackbody temperature. The detector will measure a certain number of counts from an emitting

56

source. The number of counts, $C(\lambda)$ can be related to the irradiance of the source $E_l(\lambda)$ by the following equation;

$$C(\lambda) = F(\lambda)E(\lambda)n_a n_p \Delta t \qquad (3.2)$$

n_a is the number of acquisitions, n_p is the number of pixels binned and Δt is the gate time of the camera. $F(\lambda)$ is a calibration function that takes into account all losses encountered during measurement. Rearranging for $F(\lambda)$ gives the following expression.

$$F(\lambda) = \frac{C_l(\lambda)}{E_l(\lambda) \cdot (n_a n_p \Delta t)_l} \qquad (3.3)$$

If a source of known irradiance is measured the calibration function for a particular setup can be found. Measurements were made of the lamp output 50 cm from the lamp source where there is a uniform radiation flux described by Eq. 3.1. This is shown in Fig. 3.5 for four different spectral regions.
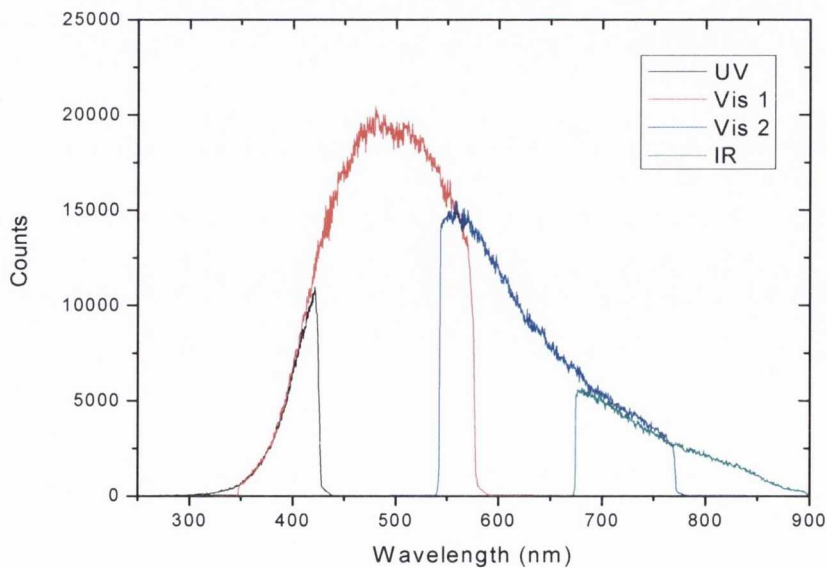

Figure 3.5 Signal recorded from the quartz tungsten halogen lamp for different spectral regions.

The equation for the number of counts measured from a plasma source will be as follows;

$$C_p(\lambda) = F(\lambda) \cdot L_p(\lambda) \cdot \Delta\Omega \cdot (n_a n_p \Delta t)_l \qquad (3.4)$$

In the above equation $L_p(\lambda)$ is the plasma spectral radiance (W m^{-2} nm^{-1} sr^{-1}). Rearranging Eq. 3.4 for $L_p(\lambda)$ and substituting for $F(\lambda)$ (Eq. 3.3) gives the following;

$$L_p(\lambda) = \frac{C_p(\lambda) \cdot E_l(\lambda) \cdot \left(n_a \cdot n_p \cdot \Delta t\right)_l}{C_l(\lambda) \cdot (n_a \cdot n_p \cdot \Delta t)_p \cdot \Delta\Omega} \qquad (3.5)$$

For the optical spectroscopy measurements, the lamp irradiance was measured using the following parameters: $n_a = 1$, $n_p = 30$, $\Delta t = 10$ μs whilst for the plasma measurements, $n_a = 1$ $n_p = 10$, $\Delta t = 10$ ns.

3.3 Langmuir probe

The Langmuir probe developed by Irving Langmuir in 1923 offers a simple method for plasma analysis [1]. The probe consists of a conducting surface that is biased and inserted into plasma. Depending on the whether the probe has a negative or positive bias, the ion or electron component of the plasma can be studied. The use of Langmuir probes in flowing plasma was developed by Koopman [2]. A small biasing circuit is required to record a signal from the plasma and a typical planar probe and a biasing circuit are shown in Fig. 3.6
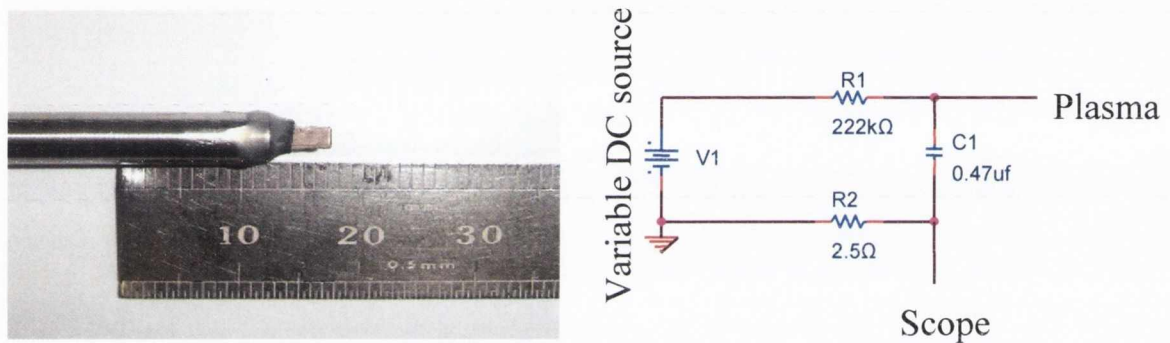

Figure 3.6 Typical planar Langmuir probe and biasing circuit

The probe is a planar piece of metal insulated at the back and the connected to an oscilloscope by coaxial cable. When a bias is placed on the probe an electric field is produced at the probe surface. If the bias is sufficiently negative then electrons from the plasma are repelled and ions are accelerated toward the probe surface. The opposite occurs if the bias is sufficiently positive. If one scans a voltage range from a large negative value to a large positive value and records the current, the probe current – voltage (IV) characteristic plot can be obtained. In the IV characteristic there are separate saturation regions; when biased sufficiently negative (< - 5 V) a saturated current due to ions is recorded. For positive bias a current due to electrons is measured. A typical ion signal is shown, in Fig. 3.7, for plasma produced from 248 nm ablation of silver in vacuum. The

laser fluence was 1 J/cm^2, the probe was biased at -30 V and placed at 9.5 cm from the target. The current was measured over a 10 ohm resistor.
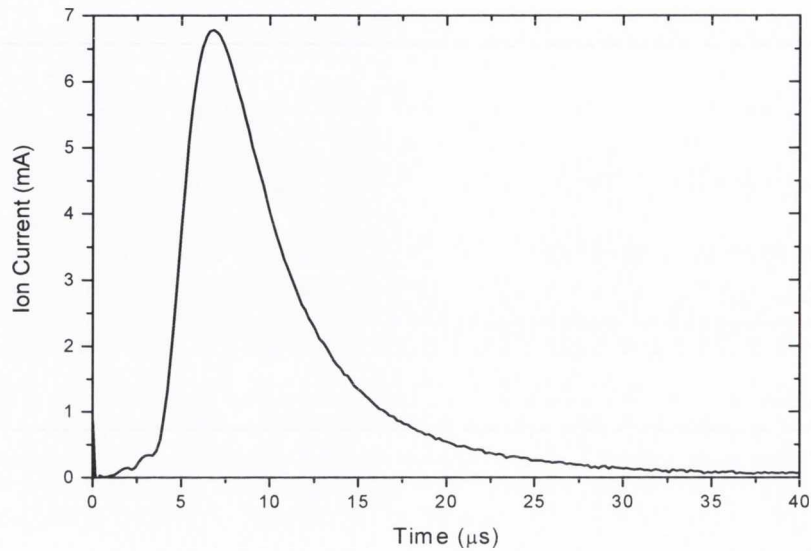

Figure 3.7 Ion time of flight signal taken during 248 nm ablation of Ag using a Langmuir probe biased at -30 V.

From Fig. 3.7 the arrival of the plasma at the probe is around 3 μs, the peak time of flight occurs at 7μs and the less dense part of the plasma reaches the probe at later times. There is a small fast peak at $\approx$ 2 μs which is due to low Z contamination on the target surface. The relationship between the ion current I, and the ion density n_i is given by [3]

$$I = n_i e A v \qquad (3.6)$$

where v is the velocity of the ions and can be approximated by the target – probe distance d, divided by the time of flight t found from the ion signal. There is an initial acceleration of the laser ablation plume but it is short compared with the time of flight. A is the probe area and e is the charge due to an electron. The ion time of flight signal can also be used to find the ion energy distribution through the following equation [3]

60

$$\frac{dN}{dE} = \frac{It^3}{Amed^2}$$ (3.7)

where dN/dE is the number of ions per energy interval per unit area with units $eV^{-1}\ m^{-2}$ and m is the ion mass The average ion energy is found from the ion energy distribution using the following equation [3].

$$<E> = \frac{\int E \frac{dN}{dE} dE}{\int \frac{dN}{dE} dE}$$ (3.8)

If the probe is biased sufficiently positive then it will record a signal due to the electron component of the plasma. The electron signal is somewhat similar in shape to the ion signal and a typical electron signal is shown in Fig. 3.8 corresponding to the same conditions as for the ion signal shown in Fig. 3.7 but with a bias of + 10V.
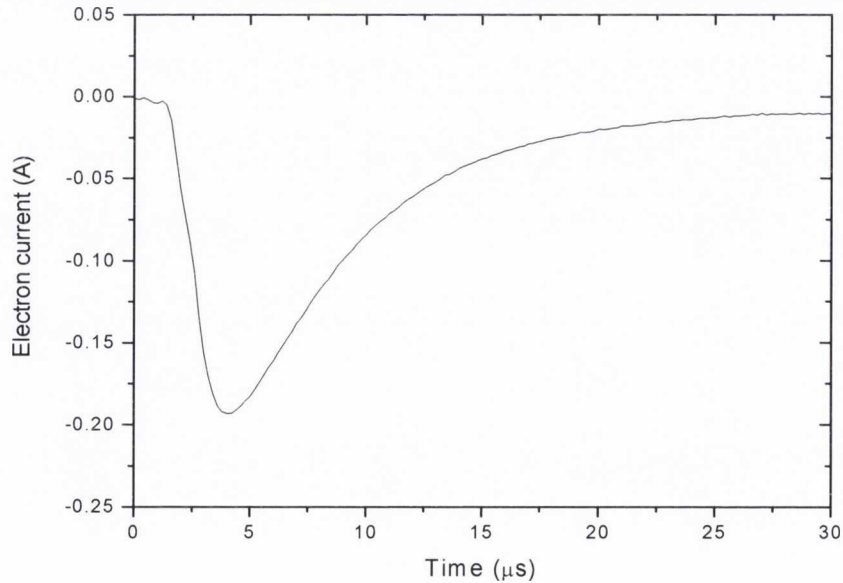

Figure 3.8 Electron current measured using a Langmuir probe biased at +10 V.

A comprehensive study on the use of Langmuir probes in laser ablation plasmas was undertaken by Doggett [3].

3.4 Surface and thin film characterisation techniques

3.4.1 Material removal during laser ablation

For removal of material during laser ablation a Zygo white light interferometer was used. The interferometer can profile the variation of height on a surface. A small crater can be formed in a solid target for a fixed number of laser shots if the target is kept stationary. The three - dimensional (3D) depth profile can be measured and the average ablated volume and/or the ablated depth per shot can be found. Interferometry of the target surface produces a pattern of bright and dark fringes that result from an optical path difference between a reference and a sampling beam. White light is split inside the interferometer, one beam going to an internal reference surface and the other to the target. After reflection, the beams recombine inside the interferometer, undergoing constructive and destructive interference and producing a fringe pattern. A precision translation stage and a CCD camera together generate a 3D interferogram of the sample which is stored in the computer memory. The interferogram is then transformed by frequency domain analysis into a quantitative 3D image. Figure 3.9 shows an image of the setup within the Zygo instrument and a 3D surface profile.
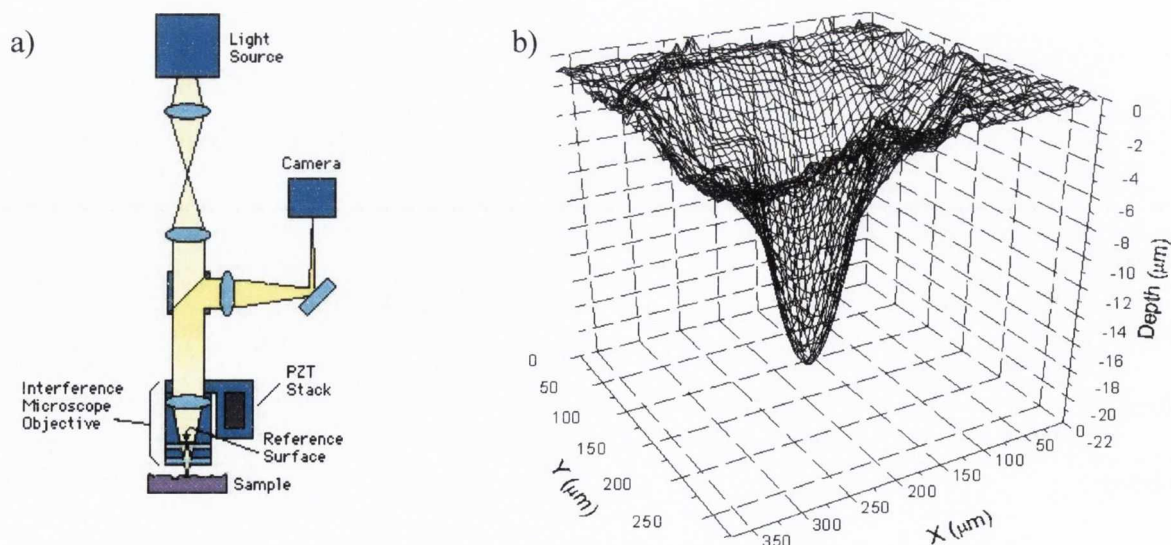

Figure 3.9 Diagram of the main components of the Zygo white light interferometer (a) and a measured 3D surface profile of a crater formed by laser ablation (b).

During some earlier measurements, before the availability of the interferometer, a mass loss technique was used to find the average amount of material removed per. If a rotating target is ablated for a large number of shots ($\approx$1-5x10^4) a sufficient amount of mass is removed that can be measured by a microbalance. Knowing the atomic mass of the target material and its solid density the average total number of ablated atoms per shot can be found from which the ablated volume and depth can be inferred. The accuracy of this technique is limited by the time it takes to remove a measurable amount of material. At 10 Hz the time it takes to remove a measurable amount of material is between 16 and 90 minutes for the shot number quoted above. During ablation the target condition can degrade during such a long ablation time and this can lead to a variation of the amount of ablated material during the measurement.

3.4.2 Deposited film characterisation

The ablation products can be deposited on suitable substrates placed at a fixed distance from the target surface. To image the surface profile of deposits and/or laser irradiated targets both optical and electron microscopy was used. A 5 mega pixel Leica DFC 420 CCD camera was coupled to a Leitz Laborlux 12 ME microscope which was used for optical microscopy at the micron scale. A Hitachi H700, 100 kV Transmission Electron Microscope (TEM) was used to image at the nano scale. The resolution of the optical microscope was a few μm. The TEM has a resolution of around 0.5 nm.

The optical properties of metal deposits were analysed using UV-Vis optical spectrophotometry. The UV-Vis spectra could be compared to optical calculations to infer thickness and whether the deposits behave like a bulk thin film. This technique was also used to examine the more peculiar properties of nanostructured metal films. The spectrophotometer used was a Shimadzu UV-2401PC that contained a dual arm configuration and operated from 350 – 800 nm. The optical program used for comparison

to measurements was the XOP IMD 4.1 suite [4] which allowed for calculation of optical properties of single and multi layers as a function of substrate and beam properties.

To measure thin film thickness of large area samples, a second technique was developed which was based on an optical transmission flatbed scanner (Epson Perfection V700 PHOTO, 6400 dpi). The scanner was calibrated for transmission using a set of neutral density filters. The transmission values of the filters that are correlated to the transmission signal of the scanner are for a wavelength of 515 nm. The calibration curve is shown in Fig. 3.10
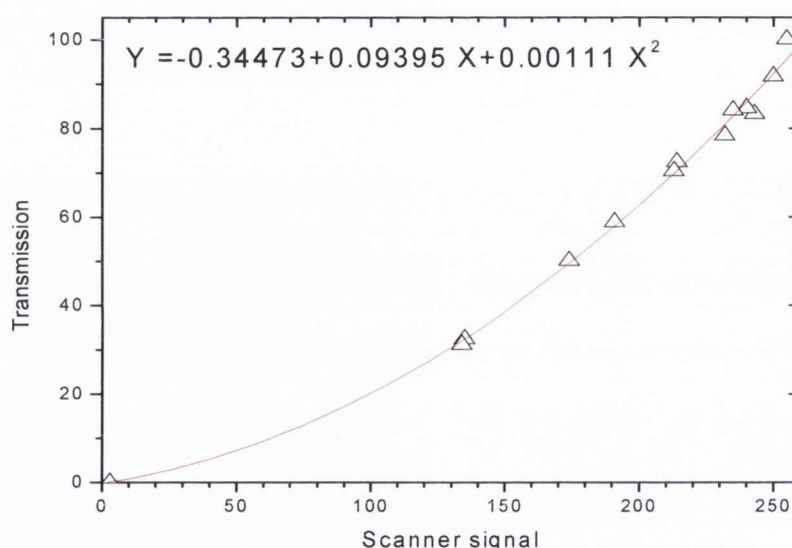

The plot shows the fit equation: $Y = -0.34473 + 0.09395\ X + 0.00111\ X^2$

Figure 3.10 Calibration curve for the optical transmission scanner to convert scanner signal to film transmission. A 2nd order polynomial fit is shown in red and the equation is given in the plot.

Using the above calibration the spatial variation of transmission of a film (and substrate) can be found. The total transmission, T_t of a thin film on a substrate is simply $T_t = T_1 T_2 T_3$ where the subscripts 1, 2 and 3 represent interfaces between regions of different refractive index. This is shown in Fig. 3.11. The transmission of a bare substrate, T_s is given by $T_s = (T_3)^2$. The film transmission into the substrate is $T_f = T_1 T_2$.
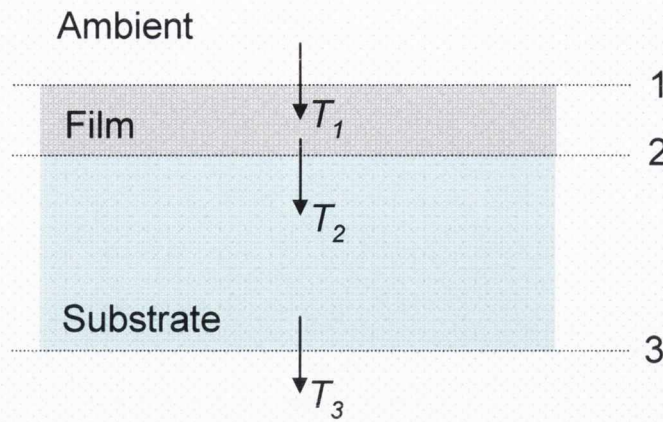
Figure 3.11 Formalism for measuring transmission with flatbed scanner

Dividing T_t by T_s, T_f can be expressed as the following.

$$T_f = Tt/T_3 \tag{3.9}$$

Taking an example of a thin film on glass, the film transmission into the glass would be the total transmission, T_t multiplied by 0.96. If bulk values are assumed for the refractive indices of the film and substrate, the film thickness can be found. A calculation using the XOP program [4], which is based on Eq. 2.24 - 2.25, was used to calculate the change in transmission with film thickness. This is shown in Fig. 3.12 for the example of a nickel film. This plot can then be used to convert the measured transmission into thickness. Although this technique is approximate it was found to compare well with thickness measurements made by spectroscopic ellipsometry and the optical properties of the deposited films did not differ substantially from bulk. This was confirmed using UV-vis optical spectrophotometry.
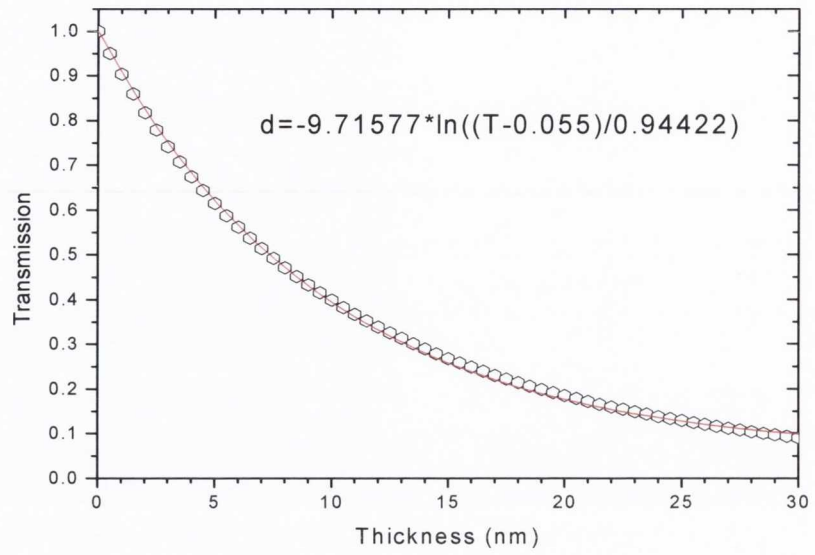
$$d=-9.71577*\ln((T-0.055)/0.94422)$$

Figure 3.12 Calculated transmission as a function of nickel thickness.

In chapter 5 this technique is used to measure the variation of the deposited material during femtosecond laser ablation and this measurement is related to the angular distribution of the total ablation plume.

3.5 Spectral synthesis code

To calculate the emission and absorption from laser produced plasmas the PrismSPECT code is used [5]. PrismSPECT is a collisional - radiative spectral analysis code designed to simulate the atomic and radiative properties of laboratory and astrophysical plasmas. It computes the ionisation dynamics and spectral properties of single-cell plasmas and is designed to calculated plasma properties over a grid of input parameters such as temperature, density and length. In this thesis the code is used to infer plasma conditions from spectroscopic measurements and to calculate absorption properties of low temperature laser produced plasma.

For PrismSPECT simulations a set of atomic data for each element is provided from the ATBASE suite of atomic codes [6]. These codes calculate atomic level and transition energies as well as the oscillator strengths of each transition. The code computes atomic level populations and spectra for LTE and non-LTE plasmas and calculates the ionisation fraction, level populations, wavelength dependant emission and absorption and if the plasma length has been specified, the optical depth can also be output. The code also includes the ability to model broadening of discrete transitions that includes contributions from Stark, natural and Doppler broadening mechanisms.

First the plasma element is selected and the particular plasma model is used. There is a choice of four different models. These are as follows:

1) *Backlighter K-shell Spectroscopy.* A model that includes atomic levels with K-shell vacancies for Ne-like through He-like ions.

2) *Emission K-shell Spectroscopy*. A model that includes very detailed atomic level structures for Li-like ions and higher ionization stages. Only ground states of lower ionization stages are included.

3) *Emission Visible/UV/EUV Spectroscopy*. A model that includes levels over a relatively broad range of ionization stages.

4) *Low Temperature Spectroscopy*. Includes very detailed atomic level structures for ionization stages up to IV and only ground levels for the remaining ionization stages.

For the simulations used in this thesis the low temperature spectroscopy model is used. For higher plasma temperatures where three times ionised species become important the full Visible/UV/EUV model is used to ensure a correct ionisation balance. This was only required on occasion as, for the most part, the plasma under consideration in this thesis is made of neutral atoms and singly and double ionised species. The other models are more appropriate for high temperature plasma spectroscopy.

Next the simulation type is specified. There is a choice whether to run a steady state or a time dependant calculation. The plasma geometry, electron distribution, units of density and plasma size are specified and the option of including an external radiation source is also specified. For the simulations presented later the slab geometry is used as opposed to spherical or zero width, the electron distribution is chosen as Maxwellian, the density is specified in terms of an ion density and the plasma size is described by its length. An external radiation source is not included. After this the single cell plasma ion density and temperature and the plasma length are specified. This can be setup as a grid for the calculation to be performed for a range of different values for two of the three parameters. A collisional radiative (non – LTE) atomic level population model is chosen and the spectral region is set over which the calculation will run. The code can also calculate the

contribution to the total emission or absorption from the various absorption mechanisms and also the contribution from each ion stage.

The simulation is then run and depending on the element, the number of grid points specified and the size of the spectral grid the code can take anywhere between a few seconds and several hours to run. When completed, the emission and absorption spectra can be viewed using a spectral viewer post processor application contained within the code. The line ratios and ionisation fraction and populations can also be viewed using similar post processor applications.

3.6 References

[1] I. Langmuir and H.M. Mott-Smith, *Gem. Electr. Rev.*, **26**, 731 (1923)

[2] D.W. Koopman, Physics of Fluids, **14, 8**, 1707 (1971)

[3] *'Characterisation of laser produced plasma'*, B. Doggett, PhD thesis (2006)

[4] http://www.esrf.eu/computing/scientific/xop2.1/extensions.html

[5] http://www.prism-cs.com/Software/PrismSpect/PrismSPECT.htm

[6] http://www.prism-cs.com/Software/AtomicData/AtomicData.htm

Chapter 4: Optical emission and absorption in nanosecond laser produced plasma

In this chapter the optical emission from the early stage of the laser ablation plasma was measured in an attempt to characterise the ablation process at early times. For a laser operating at $\lambda = 1064$ nm (Nd:YAG) and a fluence of 1.5 J cm^{-2}, the temporal variation in the spectral emission from silver plasma was recorded. The emission was compared to calculations using a spectral synthesis code to extract the density and temperature. The expansion model described in chapter 2 was used to estimate the plasma size so opacity effects could be included.

From this initial study, it was observed that the early emission is continuous. After a short delay, line spectra due to atomic transitions appear. In chapter 2 it was described how the absorption properties of laser ablation plasma are unclear so an attempt was made to confine the expansion of plasma to hold it in its initial high density state. This will be advantageous for a future experiment that will measure the plasma absorption. This is described in the second section of this chapter.

The third section describes a measurement of the plasma absorption made using the dual laser produced plasma technique with a novel target geometry.

4.1 Optical characterisation of silver laser ablation plasma

4.1.1 Optical emission from silver laser ablation plasma

The temporally resolved optical emission was measured for 1064 nm ablation of silver in vacuum at a laser fluence of 1.5 J cm^{-2}. The laser angle of incidence was 45° and the emission was measured normal to the target surface. Figure 4.1 shows a timing diagram of when the measurements were made with respect to the laser pulse. Time zero was chosen at the onset of the plasma emission which will be early in the laser pulse temporal profile. The camera gate time, Δt for this experiment was 10 ns and is shown on the diagram by the shaded area. The solid black line is the laser pulse temporal profile and the pulse duration was measured to be 13 ns using a fast photodiode.
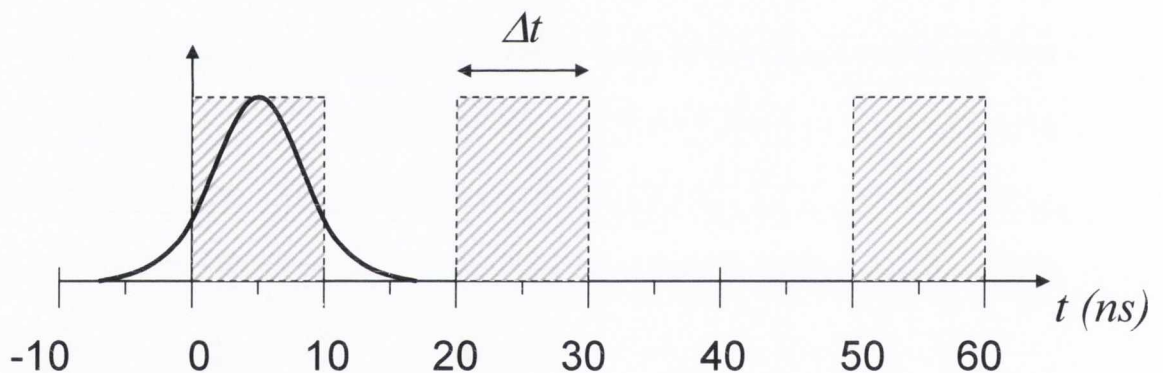

Figure 4.1 Timing diagram showing the laser pulse duration (≈13 ns) compared to the gating time of the camera.

Figure 4.2 shows optical emission spectra in the region 320 – 850 nm for early times. The absolute spectral radiance is plotted as a function of wavelength and three sets of separate spectra are shown in each plot corresponding to different grating angles. This enabled the recording of the emission from the near UV to the near IR. Figure 4.1 shows the measured spectra for 0 and 20 ns. For the measurement at 0 ns the plasma emission is a broad continuum.
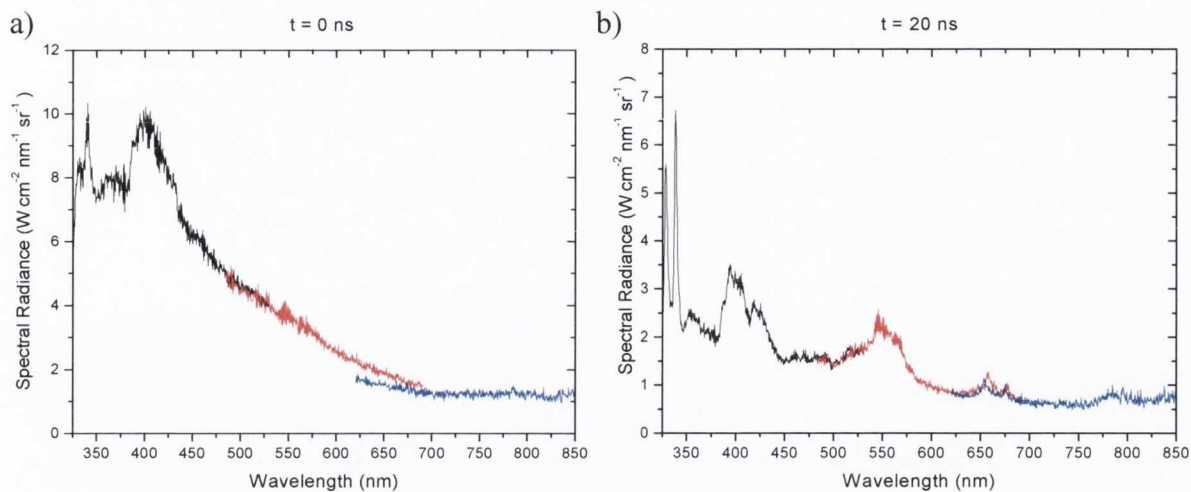
72

Figure 4.2 Spectral radiance emitted from plasma at (a) 0 and (b) 20 ns with respect to laser emission.

It is assumed that the plasma will begin emitting early in the pulse duration so that the spectrum shown in Fig. 4.2 (a) represents the total emission during most of the laser pulse duration. The physical reason for the continuous profile is unclear and will be discussed later in this chapter. In Fig. 4.2 (b) the continuum emission is still present but several spectral features begin to emerge. The line transitions at 328 and 338 nm are transitions from the $4d^{10}$ 5p level to the ground state, $4d^{10}$ 5s, in Ag I. The spectral feature in the 375 – 450 nm range is most likely made up of several broadened lines arising from Ag I and Ag II transitions. This is also likely to be the case for the feature observed between 500 – 600 nm. A simplified energy level diagram for Ag I is shown in Fig. 4.3 indicating the main transitions.

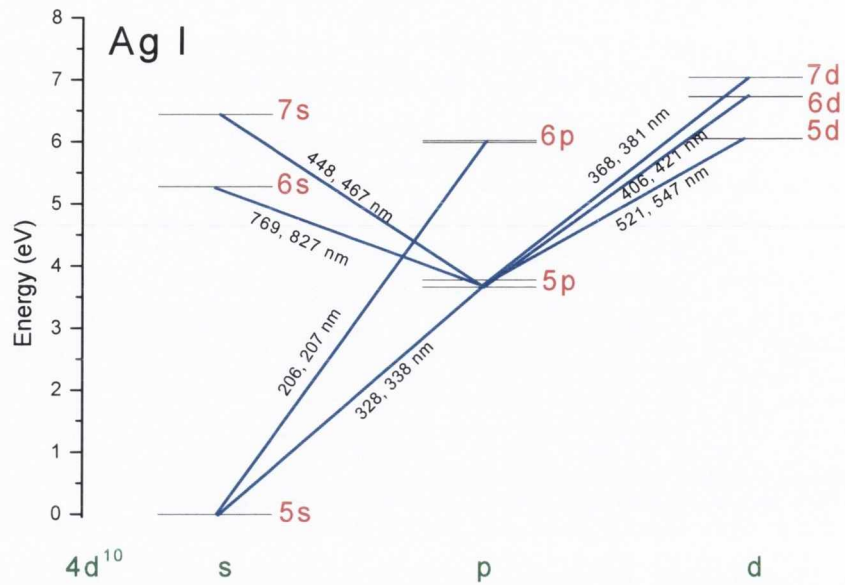**Figure 4.3 Simplified energy level diagram for Ag I showing the most important radiatively linked levels.**

The simplified energy level diagram in Fig. 4.3 shows the levels that can give rise to emission in the spectral region that is measured. The 6p – 5s transition is also shown but this transition falls outside our range of measurement. Table 4.1 describes the transitions that can arise between the levels shown in Fig. 4.3.

Wavelength (nm)	Configuration Lower level - Upper level		$g_1 : g_2$	A_{21} (s^{-1}) (NIST)	A_{21}(s^{-1}) (Kurucz)
206.1	$4d^{10}5s: {}^2S_{1/2}$	$4d^{10}6p: {}^2P_{3/2}$	2 : 4	3.1×10^6	1.2×10^7
207.0	$4d^{10}5s: {}^2S_{1/2}$	$4d^{10}6p: {}^2P_{1/2}$	2 : 2	1.5×10^6	1.1×10^7
328.1	$4d^{10}5s: {}^2S_{1/2}$	$4d^{10}5p: {}^2P_{3/2}$	2 : 4	1.4×10^8	1.0×10^8
338.3	$4d^{10}5s: {}^2S_{1/2}$	$4d^{10}5p: {}^2P_{1/2}$	2 : 2	1.3×10^8	4.7×10^7
368.3	$4d^{10}5p: {}^2P_{1/2}$	$4d^{10}7d: {}^2D_{3/2}$	2 : 4	-	9.7×10^6
381.1	$4d^{10}5p: {}^2P_{3/2}$	$4d^{10}7d: {}^2D_{5/2}$	4 : 6	-	1.0×10^7
405.6	$4d^{10}5p: {}^2P_{1/2}$	$4d^{10}6d: {}^2D_{3/2}$	2 : 4	-	8.6×10^5
421.1	$4d^{10}5p: {}^2P_{3/2}$	$4d^{10}6d: {}^2D_{5/2}$	4 : 6	-	8.8×10^5
421.3	$4d^{10}5p: {}^2P_{3/2}$	$4d^{10}6d: {}^2D_{3/2}$	4 : 4	-	1.5×10^5
447.6	$4d^{10}5p: {}^2P_{1/2}$	$4d^{10}7s: {}^2S_{1/2}$	2 : 2	-	3.7×10^4
466.8	$4d^{10}5p: {}^2P_{3/2}$	$4d^{10}7s: {}^2S_{1/2}$	4 : 2	-	7.3×10^4
520.9	$4d^{10}5p: {}^2P_{1/2}$	$4d^{10}5d: {}^2D_{3/2}$	2 : 4	7.5×10^7	2.7×10^7
546.5	$4d^{10}5p: {}^2P_{3/2}$	$4d^{10}5d: {}^2D_{5/2}$	4 : 6	8.6×10^7	2.8×10^7
547.2	$4d^{10}5p: {}^2P_{3/2}$	$4d^{10}5d: {}^2D_{3/2}$	4 : 4	1.4×10^7	4.7×10^6
768.8	$4d^{10}5p: {}^2P_{1/2}$	$4d^{10}6s: {}^2S_{1/2}$	2 : 2	-	6.0×10^6
827.4	$4d^{10}5p: {}^2P_{3/2}$	$4d^{10}6s: {}^2S_{1/2}$	4 : 2	-	9.6×10^6

Table 4.1 Important radiative transitions for Ag I.

From the table above a considerable number of transitions may be observed in the spectral range shown in Fig. 4.1. The energy level data for Ag I was taken from the tables of Moore [1] and the A_{21} values were taken from the NIST spectral database [2]. Only values of A_{21} for the strongest transitions were given here. Pickering and Zilio [3] give a list of f values for Ag I transitions that are taken from calculations performed by Kurucz [4]. A_{21} values calculated from this data are shown in the last column of table 4.1. However, there still

remains a lack of experimentally measured transition probabilities for Ag I transitions which makes interpretation of the spectra difficult. There is even less data available for Ag II, especially in the spectral region of interest here.

For later times as the plasma begins to expand and cool, broadened line emission is observed in the observed spectra. Figure 4.4 shows the spectra recorded at 50 and 80 ns.
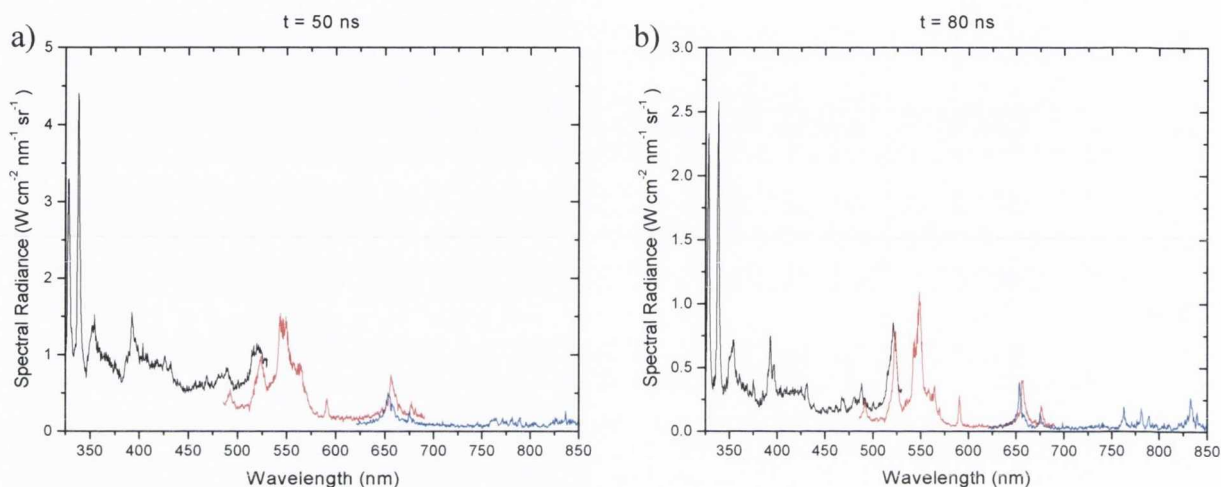

Figure 4.4 Optical emission spectra at (a) 50 ns and (b) 80 ns.

The 5d – 5p lines in Ag I are now resolved as well as lines at 354, 392, 491, 589 and 653 nm. It is unclear which transitions these lines are due to as they do not correlate with any of the Ag I transitions in table 4.1. The NIST database lists Ag II transitions at 391, 392 and 395 nm but there are none in close proximity to the other lines mentioned above. These unknown transitions may be due to target contamination. The appearance of several features in the region 750 – 850 nm could be due to the 6s – 5p transitions in Ag I. Transitions in Ag II, where several lines in the 800 – 850 nm regions are given in the NIST database, may also contribute in this region. The optical emission for 100 to 200 ns is shown in Fig. 4.5.
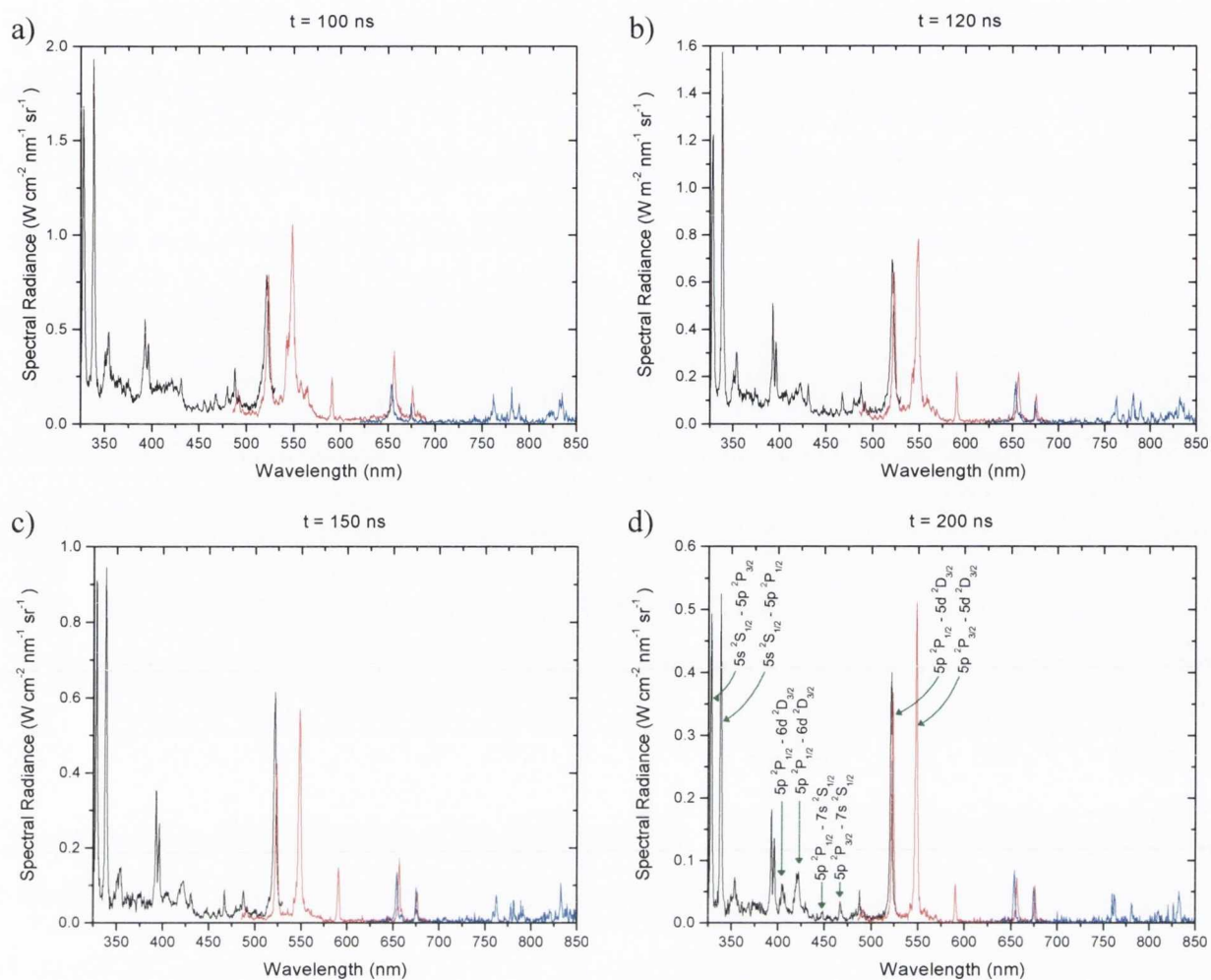
Figure 4.5 Optical spectra for (a) 100 ns (b) 120 ns (c) 150 ns (d) 200 ns. In (d) the configurations are given for the transitions that are present in table 4.1.

The Stark broadening is reduced significantly as the system evolves until at late times the broadening is determined by the instrument width. At a time of 500 ns (not shown) the 5d - 5p transitions for Ag I have a line width of 1.4 nm. This is taken as an estimate of the resolution of the system giving a resolving power of ≈370 at 520 nm. The maximum resolution attainable with the spectrometer was quoted in chapter 3 as 0.7 nm. However, for the optical imaging system used in this experiment the spectrometer acceptance angle is under filled. This leads to a reduction in the resolution as the grating is not fully illuminated.

4.1.2 Plasma expansion and spectral calculations

For a given delay after the laser pulse at which the emission measurements are made, the plasma will have expanded with respect to the previous measurement. The rate of expansion will influence the plasma size, density and temperature as a function of time. To extract the average temperature and density of the plasma from the measured emission spectra the PrismSPECT spectral synthesis code will be used to fit the spectral emission. The code takes temperature and density as inputs, and if opacity is to be included, the plasma length, in the direction of the measurement, must also be specified. To estimate the plasma size the Anisimov gas expansion model that was described in chapter 2 is used. The model requires the initial plasma dimension, the average energy per particle and the adiabatic ratio of the plasma to calculate the temporal evolution of the plasma position in each expansion direction.

The initial estimates of the plasma shape are made as follows. The initial in-plane dimensions of the plasma are taken as the laser spot dimensions on the target. The laser spot was measured to be 1.75 x 1.25 mm giving a value for the initial plume radii, X_0 and Y_0 of 875 and 675 μm respectively. The initial plume thickness can also be estimated using the following procedure. During the laser pulse the plasma formed will undergo one-dimensional expansion with a forward velocity equal to the speed of sound, c_s. The distance travelled at the end of the laser pulse, and therefore the plasma thickness, is found from $Z_0 = c_s \tau_l$, where τ_l is laser pulse duration. The speed of sound can be estimated from the following equation.

$$c_s = \left(\frac{\varepsilon_i}{m_p}(\gamma-1)\gamma \right)^{\frac{1}{2}}$$

(4.1)

ε_i is the average energy per particle and γ is the adiabatic index of the expansion which is equal to the ratio of specific heats. For an ideal gas $\gamma = 5/3$ but a value of 1.25 has been proposed for a low temperature plasma [5] and a value close to this was inferred experimentally [6]. For this analysis $\gamma = 1.25$ is adopted and a value of ε_i was determined from the ion time of flight (TOF) which was measured using a Langmuir ion probe. The ion TOF for ablation of Ag, at the same conditions as the optical emission measurements were made, is shown in Fig. 4.6.
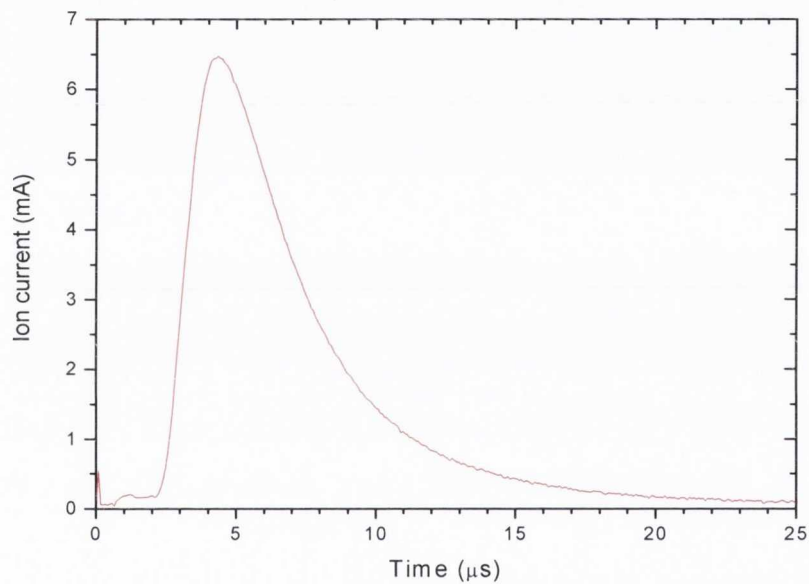

Figure 4.6 Ion TOF recorded by the Langmuir ion probe for 1064 nm, 1.5 J cm^{-2} ablation of Ag.

The probe position is at 9 cm from the target and the arrival time of maximum ion flux at the probe is 4.32 μs. Assuming constant velocity the ion energy at the peak TOF, $E_{peak} \approx$ 243 eV. Although this assumption is not strictly true, it can be seen that the initial acceleration phase lasts for a short time ($\sim$ ns), compared to the expansion time above (μs). For $\gamma = 1.25$ the average energy per particle $\varepsilon_i = E_{peak}/3.9$ giving $\varepsilon_i \approx 62$ eV. Inserting this value into Eq. 4.1 and working through, a value of $Z_0 = 55$ μm is found. The Anisimov model can then be used to calculate the expanding plasma position and shape early in time.

The input conditions into the model are as following: $X_0 = 875$ μm, $Y_0 = 675$ μm, $Z_0 = 55$ μm, $\gamma = 1.25$ and $\varepsilon_i = 62$ eV. Running the model the plume position in each dimension can be found and this shown in Fig. 4.7.
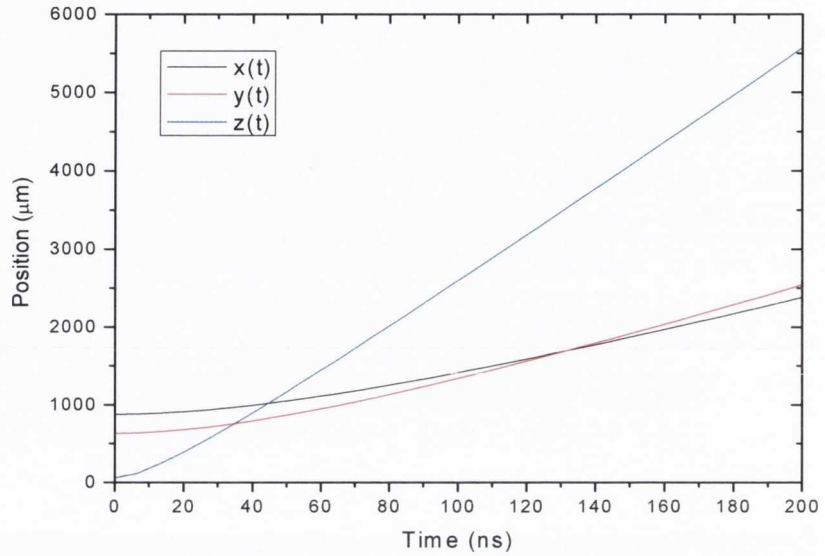

Figure 4.7 Calculated plume positions as a function of time in each spatial dimension.

Figure 4.7 gives an estimate of the plasma thickness (blue) as a function of time that is relevant to when the emission measurements are made. An estimate of the temporal variation of the average density can also be made. The average ablated depth was measured to be ~ 4 nm using the mass loss technique described in chapter 2. A rotating Ag target was ablated for 48,000 shots under identical conditions to the measurements above. It was found that 76 ng was removed per shot. This equates to $\approx 4.2 \times 10^{14}$ atoms ablated per shot. From the ion signal in Fig. 4.6, an estimate of the total ions in the plume can be made from $Y=Y(0)2\pi d^2/k_{zx}k_{zy}$ where Y is the total ion yield and $Y(0)$ is the ions number/cm^2 normal to the target at a probe distance, d of 9 cm. k_{zx} and k_{zy} were found from the final values of $z(t)/x(t)$ and $z(t)/y(t)$ in the plasma expansion simulation (see Fig.4.9). It was found that 2×10^{14} ions were ablated. This value is less than the total number of atoms as expected.

It is assumed that the number of atoms in the plume remain constant so that if we know the plume dimensions, an estimate of the average plasma density can be made. The data in Fig. 4.7 is used to find the evolution of the plasma volume. The density is shown in Fig. 4.8.
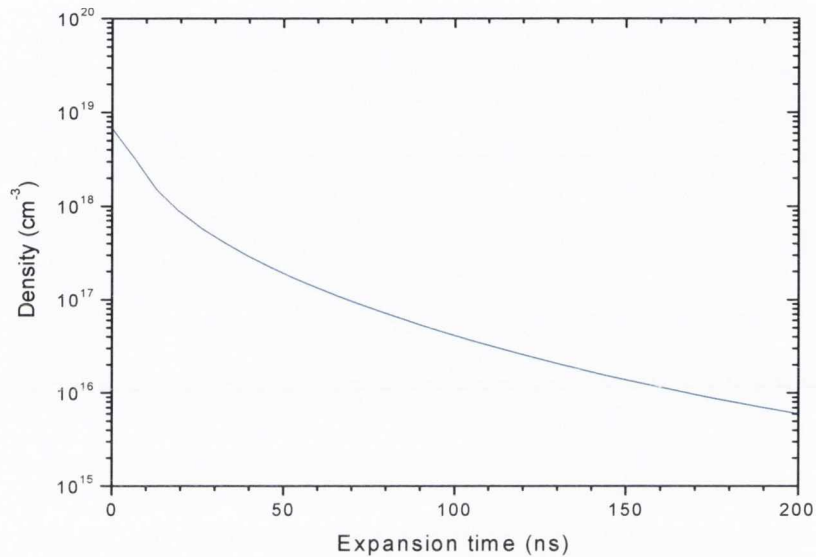

Figure 4.8 Calculated variation of the average plasma density with time.

On the timescale of interest, the average plasma density is shown to drop by nearly three orders of magnitude. Considering Fig. 4.7 again, but for extended times, it can be seen from the calculation that the plume reaches a distance of 9 cm, the probe position, at a time of 3 μs. This agrees reasonably well with the plume front arrival time from the ion TOF (Fig. 4.6). The plume dimensions at late times are shown in Fig. 4.9.
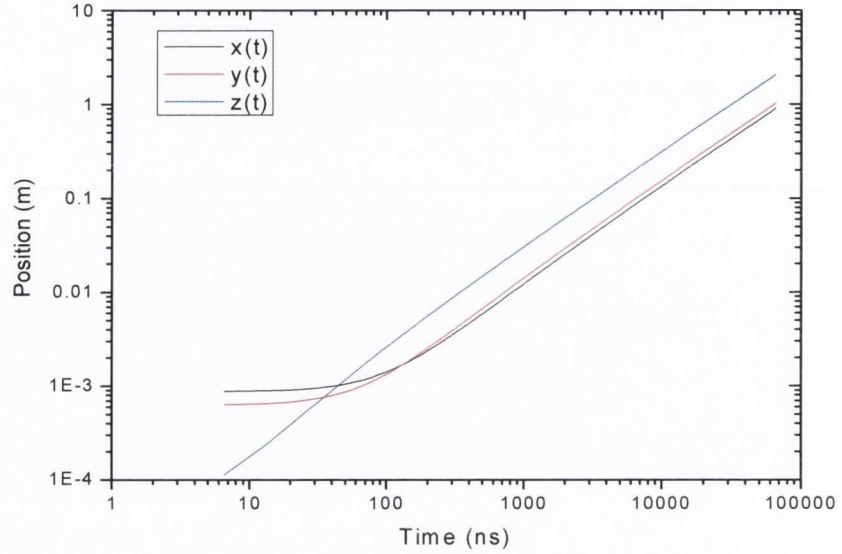
Figure 4.9 Calculated plume dimensions as a function of time.

It can also be seen from Fig. 4.9 that the acceleration phase of the plume expansion lasts for around 300 ns after which it becomes inertial. This is small compared to the plasma expansion time, indicating that the inaccuracy in assuming constant velocity to find the peak TOF energy will not be significant. The initial estimates of the average plasma density and length, at which the measurements are made are given in Table 4.2. These values can be input into the model and the temperature can be left as a free parameter that is varied to fit the experimental spectra.

Another way to infer the plasma density is to measure the line widths and calculate the plasma electron density using the following equation [7]:

$$\Delta\lambda = 2\omega\left(\frac{n_e}{10^{16}}\right) \tag{4.2}$$

$\Delta\lambda$ is the line full width at half - maximum, ω is the line width parameter due to electrons and n_e is the electron density.

Time (ns)	Average plasma density (cm^{-3})	Plasma length (μm)
0	6.7x10^{18}	55
20	8.7x10^{17}	537
50	1.7x10^{17}	1227
80	6.1x10^{16}	2149
100	3.7x10^{16}	2717
120	2.3x10^{16}	3293
150	7.8x10^{15}	4263
200	5.8x10^{15}	5636

Table 4.2 Estimates of the average plasma density and length from the model.

Djenize *et al.* [8] have measured values of 0.024 and 0.0262 nm for ω for the 5p – 5d, J = 1/2 - 3/2 (521 nm) and 3/2 – 5/2 (546 nm) transitions respectively. For their analysis they have measured ω for an electron density of 6.6x10^{16} cm^{-3} so that the denominator in Eq. 4.2 should be adjusted to account for this. The temperature at which the measurement was made was 1.5 eV. The above analysis yields a value of n_e but without knowledge of the plasma ionisation, the ion density cannot be estimated. Instead the code can be run using temperature and ion density values that give an electron density value that agrees with that extracted from the experimentally measured line widths. Table 4.3 gives the measured line widths and corresponding electron density values as a function of time delay. These values were extracted for the 5d - 5p transition at 521 nm. Due to the quasi-continuous nature of the emission spectrum at 0 and 20 ns electron density values could not be inferred.

Time (ns)	Line width (nm)	Electron density (cm^{-3})
50	12.8	1.76×10^{19}
80	5.4	7.43×10^{18}
100	3.8	5.23×10^{18}
120	3.2	4.4×10^{18}
150	2.5	3.44×10^{18}
200	2.2	3.03×10^{18}

Table 4.3 Electron density values inferred from measured line widths (521 nm) as a function of time.

In table 4.3 and for 50 ns n_e is found to be close to 2×10^{19} cm^{-3}. At 200 ns, when the line width is significantly reduced $n_e \approx 3 \times 10^{18}$ cm^{-3}. The ion densities, at these times, found from the expansion analysis are 1.7×10^{17} and 5.8×10^{15} respectively. This level of ionisation is not consistent with low temperature plasma indicating that one or both of the above analysis maybe invalid. Eq. 4.2 only includes the electronic contribution to the broadening. There is an additional term in this equation that is inserted to account for the ionic contribution to broadening [9]. There are no tabulated values for the ion broadening parameter for the above Ag I transition and in general it does not contribute appreciably to the line width and is neglected. For comparison with code calculations it was decided to run the code for values of temperature and ion density that give the, or close to the correct electron density as given in table 4.3. This was done as these values represent an experimental measurement whereas the plume expansion analysis relies heavily on the expansion model. This model has not been validated for ablation plume expansion at very early times when the plume has not reached the inertial phase. The plasma thickness calculated using the expansion model will be used as input to the code calculation but these values will be treated as a starting point that will be varied to match the measured spectra.

An average temperature can also be found from analysing the spectral line ratios for transitions that originate from excited levels with a significant energy level difference. This technique, when done for several sets of spectral lines, is known as the Boltzmann plot method [9, 10]. It requires the presence of local thermodynamic equilibrium [11] in optically thin plasma. It could not be applied here as there is only strong line emission from the 5d - 5p transition in neutral Ag. The strong 5p - 5s emission lines represent a transition to the ground state which can be strongly influenced by optical opacity and therefore cannot be used for temperature estimation.

Running the code to fit the measured spectra, it becomes clear that the electron density estimates, found from the 5d-5p (521 nm) line widths, are too large to reproduce the observed line profiles. In all cases a lower electron density value was found to fit the line profile. This indicates that either the line broadening treatment in the code is not very accurate for Ag or that the broadening parameter given in Ref. 8 is misleading. Either way reducing the electron density value, by changing the input temperature and ion density, leads to a more accurate representation of the measured 5d-5p line profiles. Adjusting the plasma thickness brings the calculated line intensity into reasonable agreement with the measured values. Table 4.4 lists the code input conditions that yield good fits to the measured 5d-5p spectra for some of the measurements made. These fits to the measured spectra are shown in Fig. 4.10.

Time (ns)	Ion density (cm^{-3})	Temperature (eV)	Electron density (cm^{-3})	Plasma length (μm)
50	1.5×10^{18}	1.2	1.37×10^{18}	50
100	8.5×10^{17}	0.8	4.2×10^{17}	50
150	5.5×10^{17}	0.7	1.84×10^{17}	50
200	5×10^{17}	0.65	1.2×10^{17}	100

Table 4.4 Spectral code inputs for fitting of experimentally measured spectra at various times.
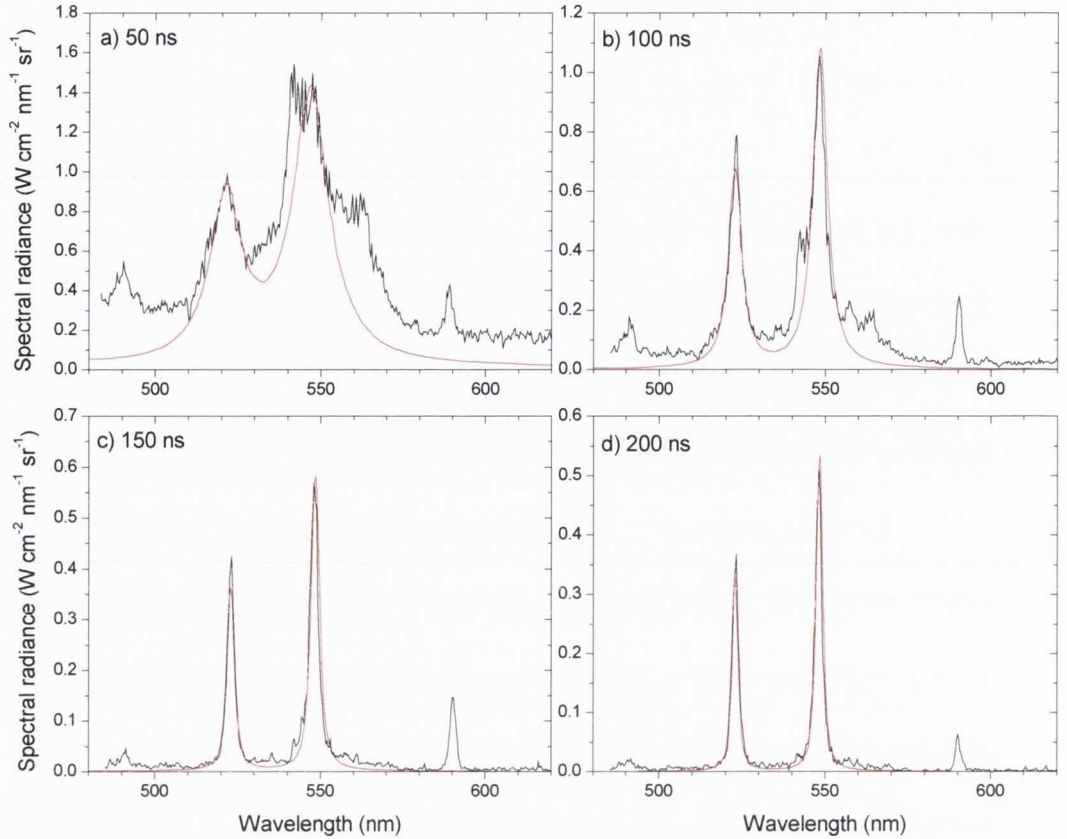
Figure 4.10 Comparison of the calculated emission spectra to measured spectra for a) 50 ns b) 100 ns c) 150 ns and d) 200 ns. The plasma conditions for the calculated spectra are given in table 4.4.

From table 4.4 it can also be seen that the plasma thickness needs to be reduced significantly for the measured intensity to be close to the calculated intensity. If the values in table 4.4 are compared to those predicted by the expansion model (table 4.2) there is a large discrepancy. It has been previously shown from hydrodynamic modelling of nanosecond laser ablation that large temperature and density gradients can be present in the ablation plasma [12]. So even though the total ablation plume length may be large, the plasma element responsible for the emission in the region we observe is thinner, thus the values used to fit the experimental spectra are equivalent to an effective plasma thickness. Sherrill *et al.* [13] constructed a two component plasma model; a hot core surrounded by a cool exterior which was required to obtain agreement between measured and calculated

spectra. Although reasonably good fits were found for the spectral regions shown in Fig. 4.10 there was poor agreement for the other spectral features shown in Fig. 4.4 - 4.5. This shows that knowledge of the plasma structure and hence detailed hydrodynamic modelling are required for accurate calculation of plasma spectra over a large wavelength range.

For very early times (0 and 20 ns) the plasma emission is continuous. In fact the emission at 0 ns, which in effect is the measured emission during the laser pulse, is a clean, featureless continuum. To reproduce the continuum emission the density and temperature values input into the code must be pushed to very high values, typically about 5×10^{19} cm^{-3} and 3 eV respectively. The corresponding electron density for these conditions is 8×10^{19} cm^{-3}. Figure 4.11 shows the calculated emission spectrum at these conditions and for a plasma thickness of 1 and 5 μm. Also shown is the measured spectrum at 0 ns. There is good agreement indicating that at high density plasma exists during the laser pulse and emits a broad continuous spectrum. The origin of this spectrum will be discussed in the next section.
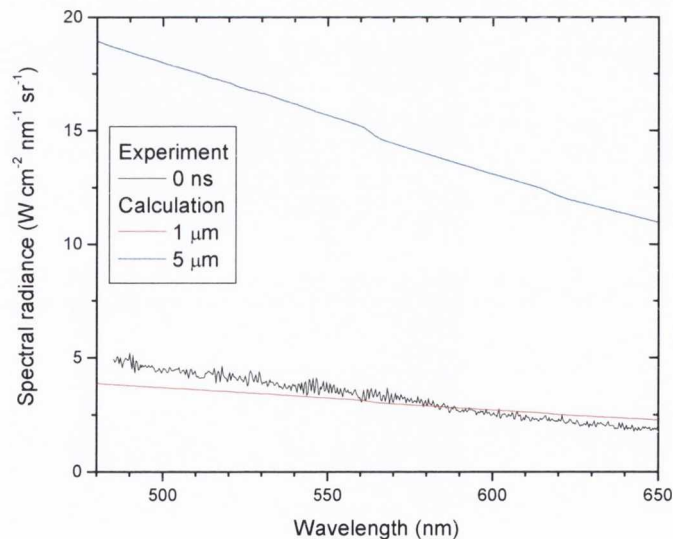

Figure 4.11 Comparison of the continuous spectrum measured at 0 ns to the calculated emission spectrum for $n_i = 5\times10^{19}$ cm^{-3}, $T_e = 3$ eV and a plasma thickness of 1 and 5 μm.

4.2 Confined laser ablation

It can be seen in the previous section that there is a rapid drop in density as the plasma begins to expand. It is a considerable technical challenge to make accurate measurements of the plasma conditions in its initial dense state. The analysis in the previous section indicates that after only 50 ns the average density has dropped by more than an order of magnitude. To study the plasma in its initial dense state, the forward expansion was restricted by placing a transparent cover over the target. The cover was a glass slide that was transparent to the laser pulse and was placed a distance of 50 μm from the target surface. Ablating the target in this geometry allows for plasma to be formed in the gap between the target and cover. Due to confinement, the plasma density remains high for much longer than in normal laser ablation. Figure 4.12 shows an image depicting confined laser ablation.
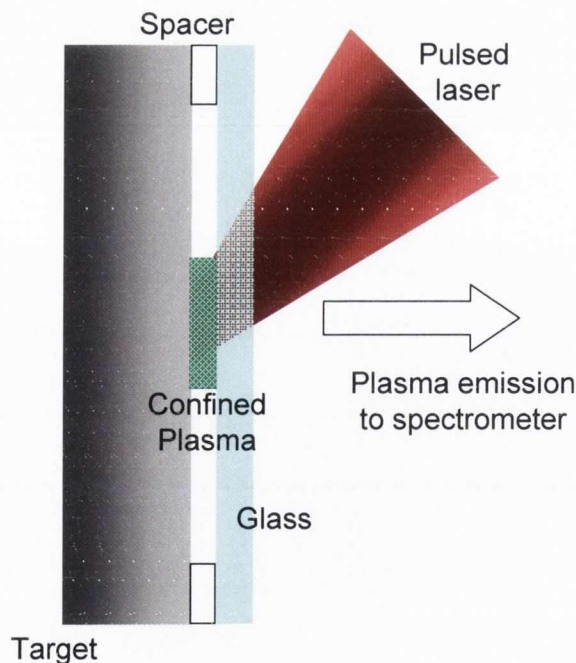

Figure 4.12 Laser ablation in a confined geometry.

Confined laser ablation was previously used by Wark and co-workers [14, 15] to produce strongly coupled dense plasma. In these studies, optical emission spectroscopy combined

with hydrodynamic and spectral modelling was used to analyse the plasma. They found that in the confining geometry uniform plasma was obtained at electron densities of ~ 10^{19} cm^{-3} and temperatures in the range of $1 - 10$ eV. The plasma remained in this state for several hundred nanoseconds compared to tens of nanoseconds for the free ablation case.

4.2.1 Optical emission from silver spatially confined laser ablation plasma

Laser ablation plasma was formed in the confined geometry for the same conditions as the free ablation experiment described in the last section. The optical emission for plasma created at 1.5 J cm^{-2} is shown in Fig. 4.13 for four different time frames. For early times the emission was measured in the $325 - 850$ nm region, while at later times measurements were made in the region between $325 - 700$ nm.
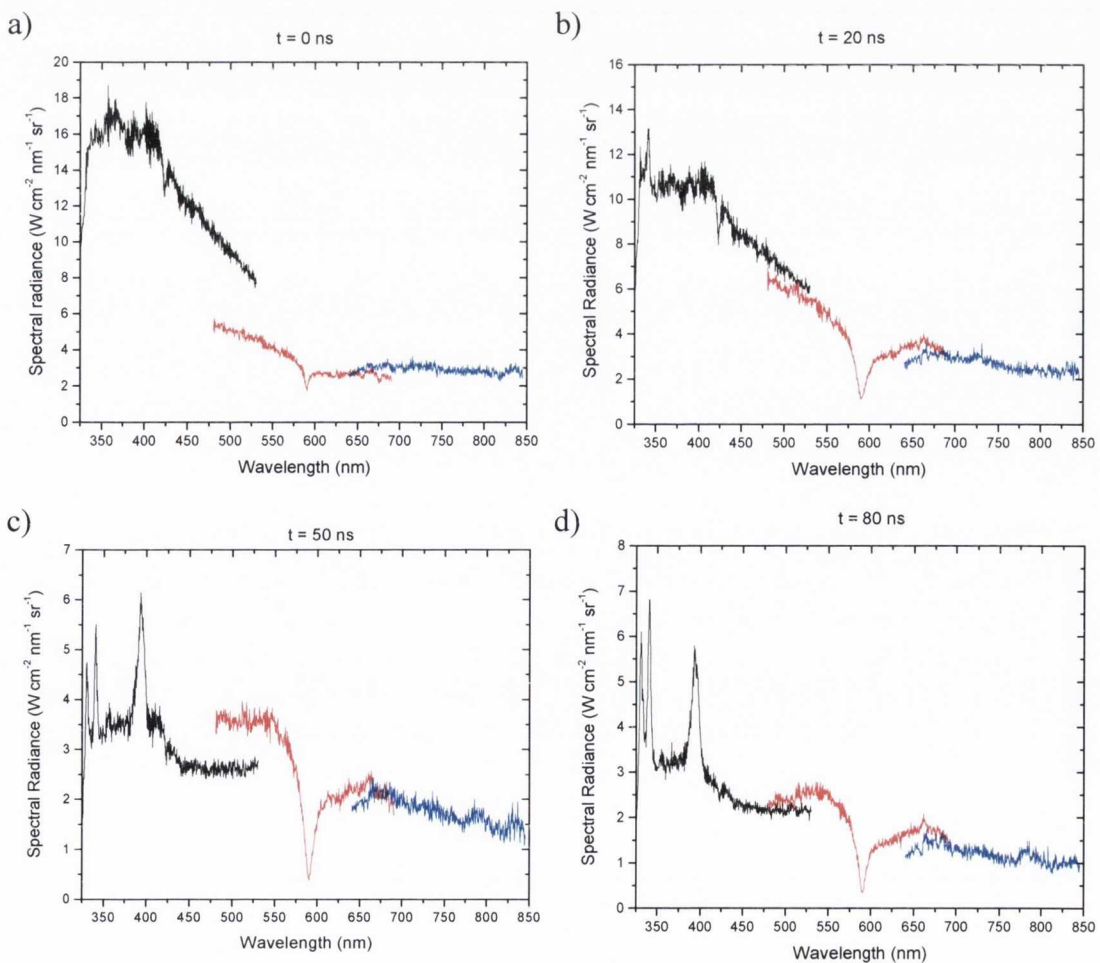

Figure 4.13 Optical emission from spatially confined laser ablation plasma for different times after the onset of emission (a) 0 ns (b) 20 ns (c) 50 ns (d) 80 ns.

The emission at early times is continuous and the broad emitted spectrum lasts longer than in the free ablation case. Some shot-to-shot variation between measurements made in different wavelength regions is evident. A broad absorption feature is present around 589 nm and this is attributed to absorption by a thin layer at the plasma glass interface. The plasma temperature will be sufficiently high to modify the walls of the confining glass [14]. Soda–lime glass was used which contains a large amount of silicon (> 70% SiO_2), sodium (~ 15% Na_2O) and calcium (~ 10% CaO). There is a strong transition in Na I at 589 nm involving the ground state and the first excited level (3s – 3p). There is also a significant difference in the melting and vaporisation temperatures of sodium compared to the two other main components of the glass. Therefore, it is reasonable to assume that this feature is due to sodium removed from the confining cover. The absorption feature is not due to a strong silver transition as the same feature is present when the silver target was replaced by an aluminium target.

As time evolves, the emitted intensity falls yet the spectrum remains continuous in nature until around 200 ns. The main energy loss mechanism will be heat conduction through the confining walls. At 50 and 80 ns some spectral features emerge from the continuum. The 5p – 5s transitions in Ag I are observed as before. The origin of the feature at 392 nm is not clear. The NIST database gives a transition at this wavelength in Ag II ($4d^85s^2$ – $4d^95p$) but does not give a transition probability making it difficult to know whether the appearance of the line would be likely. It does not correspond to any important transitions in the elements that make up the glass. At much later times than for free ablation, the continuum emission subsides and the appearance of broadened Ag I transitions is observed. Fig. 4.14 shows the emission at 250 and 300 ns after the laser pulse. The emission is similar to that observed around 50 and 80 ns in the free ablation case, indicating denser plasma at longer times.
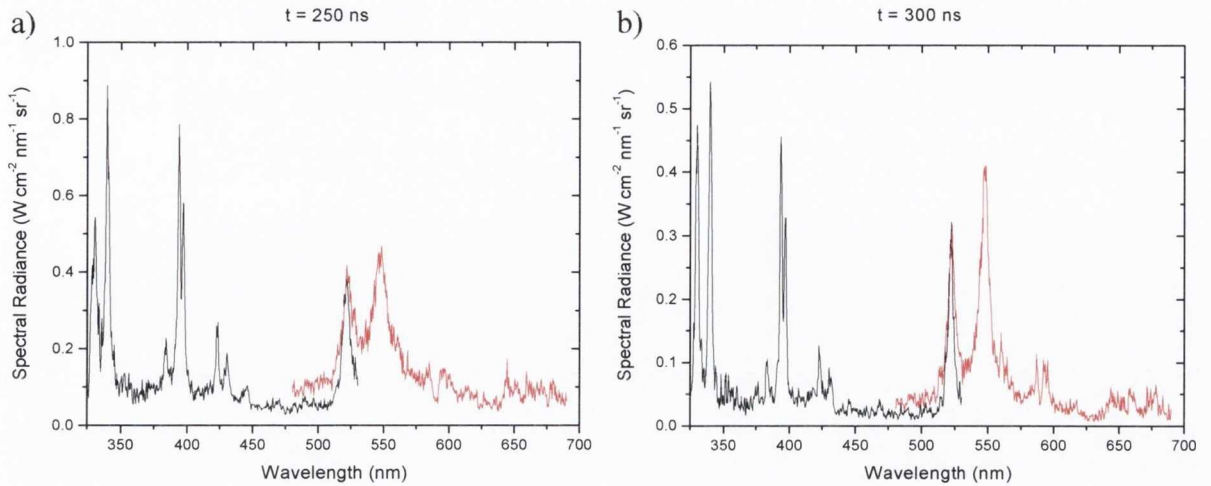
Figure 4.14 Emission at late times from confined silver laser plasma (a) 250 ns (b) 300 ns.

Previous researchers have observed similar emission profiles for confined aluminium plasma [15]. In their study the ion density was about 7×10^{18} cm^{-3} which was inferred from their measured electron density value. The laser intensity used here is about 1×10^8 W cm^{-2} where in Ref. 15 it was an order of magnitude higher. They attributed the broad emission to line broadening due to high density by comparing their line profiles to a spectral model that used line width parameters calculated by Griem [16]. The spectra in Fig. 4.14 were fitted using the spectral code in the same way as the previous section. It was found that for the 250 ns spectrum an ion density of 5×10^{18} cm^{-3} and a temperature of 0.8 eV. The corresponding electron density was 1.3×10^{18} cm^{-3} and a plasma thickness of 8 μm was used in the simulation to match the intensity. As before this indicates that temperature and density gradients will exist in the plasma. For the spectrum measured at 300 ns, good agreement was found with the spectral code for an ion density of 3×10^{18} cm^{-3} and a plasma temperature of 0.75 eV. This gave an electron density value of 7.1×10^{17} cm^{-3} and a plasma thickness of 10 μm was used for the simulation. If the above values are compared to those in table 4.4 it can be seen that the plasma produced during confined laser ablation is more dense at later times. Figure 4.15 compares the calculated spectra to the measured spectra for 250 and 300 ns.
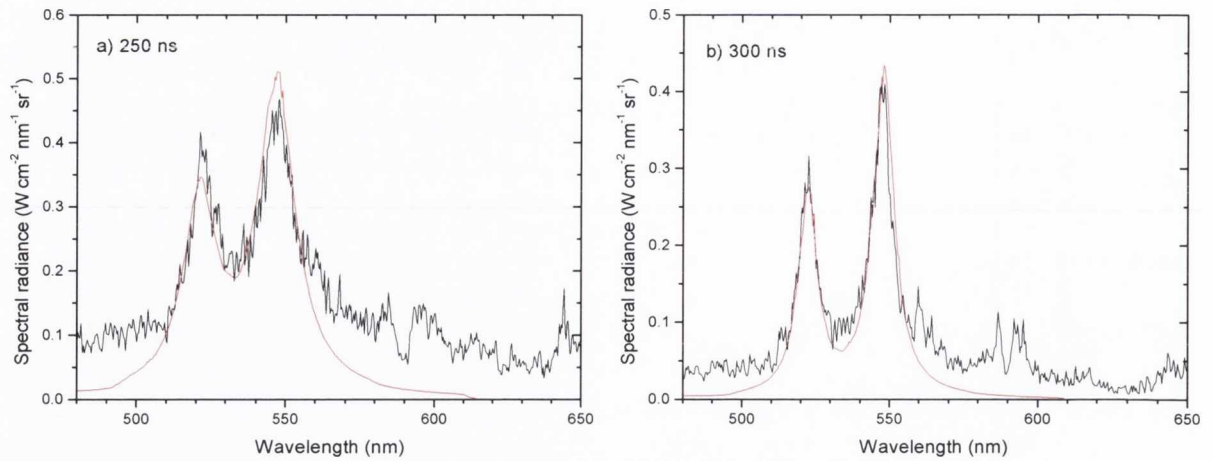
Figure 4.15 Comparison of the calculated emission spectra to spectra measured during confined laser ablation at a) 250 ns and b) 300 ns. For the 250 ns calculation the ion density, temperature and thickness are 5×10^{18} cm^{-3}, 0.8 eV and 8 μm. For the 300 ns calculation the corresponding values are 3×10^{18} cm^{-3}, 0.75 eV and 10 μm.

The origin of the broad continuum emission, observed when plasma is formed in the confined geometry, is of interest as it is an intense broadband source that would be ideal for probing the absorption properties of low temperature plasma. One possible explanation for the observed emission profile is that perhaps the hot laser irradiated surface is also emitting and as the plasma is optically thin, the superposition of plasma and surface emission is recorded. For free ablation, rapid plasma expansion leads to cooling of the plasma and the target surface cools due to heat conduction. For confined laser ablation, it may be the case that the target surface is kept at a high temperature due to plasma confinement. For both the confined and free plasma, the observed emission at early times seems to be blackbody like and to explore this idea further the emission from a blackbody is calculated and compared to the experimental measurement. The spectral radiance L_B (W m^{-2} nm^{-1} sr^{-1}) of a blackbody at temperature, T, can be found from the following equation [17];

$$L_B(\lambda,T) = 10^{-9} \left(\frac{2hc^2}{\lambda^5} \right) \frac{1}{e^{hc/\lambda kT} - 1} \qquad (4.4)$$

Blackbody emission was calculated for a few different temperatures and is compared to the confined plasma emission at 20 ns and the free plasma emission at 0 ns. This is shown in Fig. 4.16.
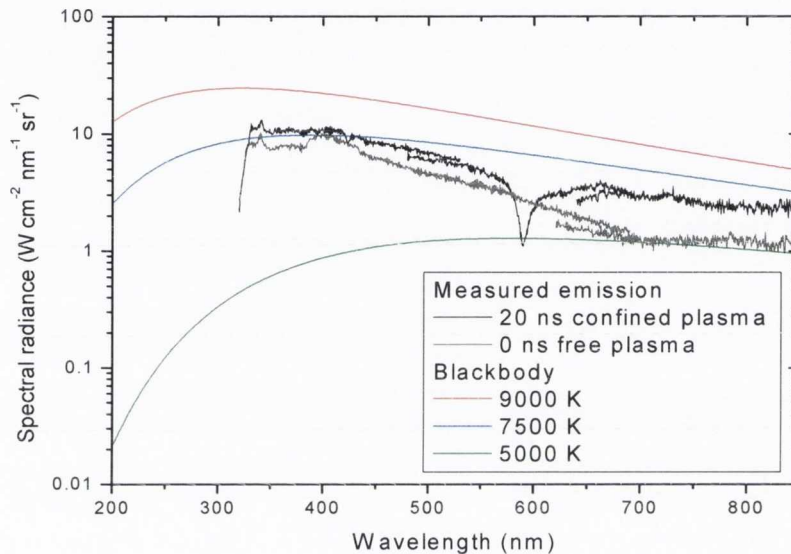

Figure 4.16 Comparison of plasma emission measured during confined laser ablation to a blackbody calculation for a few different temperatures.

Figure 4.16 indicates that the measured emission profile in both ablation geometries, at early times, is close to that of a blackbody at a temperature of several thousand Kelvin. It may be the case that the continuum emission is from the hot liquid surface or that the plasma is emitting like a blackbody. From the spectral calculations the plasma is optically thin so that the latter seems unlikely. At temperatures of several thousand Kelvin the target material will be in a vapour state. Therefore, it seems the broadband emission profile at early times is due to dense plasma. As the density is increased the observed spectral lines broaden significantly. For very high density plasma, merging of several emission lines to form a continuum is possible and this was put forth as the origin in Ref 15. As the electron density is quite high, and from Fig. 4.11 is close to 1×10^{20} cm^{-3}, bremstrahlung emission

could also contribute to a continuum emission profile. A follow on experiment is described in a future section to repeat the plasma emission measurements in a more controlled and reproducible manner to clarify exactly the main origin of the continuum emission. Also, an extension to this proposed experiment is described to measure the spectral resolved absorption of confined laser ablation plasma.

4.3 Optical absorption measurement using a dual laser produced plasma

To measure the optical absorption in laser ablation plasma in the fluence region near the ablation threshold a dual laser plasma technique was used. The first pulse formed the laser plasma which emits broadband emission as shown in the previous two sections. This emission is used as a light source to probe the absorption of a second laser produced plasma that was formed on a porous target. This target has an array of closely spaced holes and it was expected that the plasma expansion, during the laser pulse, will cover the holes. A schematic diagram of the apparatus is shown in Figure 4.17.
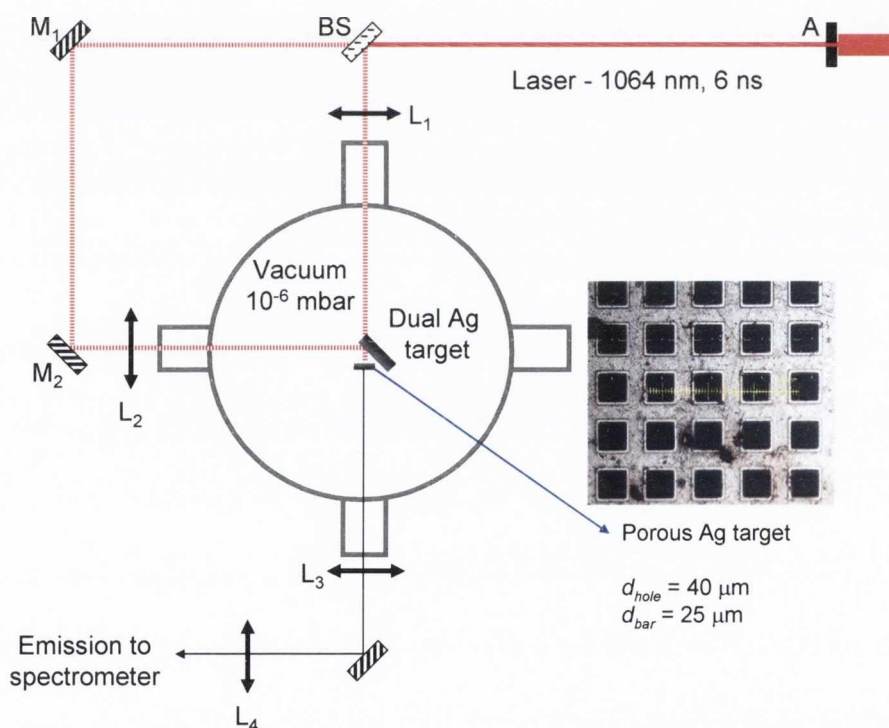

Figure 4.17 Experimental setup used for plasma absorption measurements. Also shown is the porous ablation target used.

A 1064 nm Nd:YAG laser operating at around 6 ns was used to produce both plasmas involved in the experiment. A non-polarising beam splitter (BS) was used to produce the two synchronized laser beams. The first beam was imaged onto a semi-transparent Ag

coated target consisting of an array of 40 μm holes separated by about 65 μm. This target was fabricated by coating a commercially available transmission electron microscopy support grid with silver. Figure 4.18 shows a close up of the laser target setup.
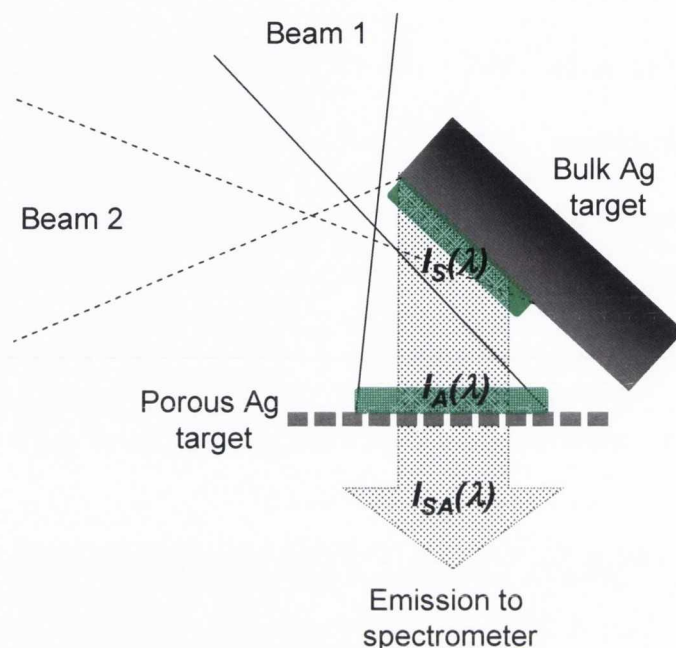

Figure 4.18 Dual target setup showing solid silver target (light source) and silver coated semi transparent target.

An aperture (A) placed in the first beam was imaged on to the semi-transparent target using lens L1 (f = 20cm). Imaging a small portion of the Gaussian laser beam ensured relatively uniform irradiation. This optical setup produced a demagnification of 3 which, in turn, gave a spot size of about 0.005 cm^2 and an average fluence of 1 J cm^{-2}. Lateral plasma expansion at about the sound velocity should be sufficiently rapid to ensure that the holes are covered with plasma during the laser pulse. The second beam was incident at 45° on another Ag target, placed 10 mm from the first. Here the laser spot size was 0.004 cm^2 and the fluence 2 J cm^{-2}. The wavelength-dependent transmission of the continuum emission of this plasma through the plasma produced on the semi-transparent target was measured using the ICCD camera and optical spectrometer described in the experimental section. The emission was imaged onto the spectrometer slit using two 10 cm focal length

96

lenses (L3 and L4) and an overall demagnification of 3. The lateral position of lens L4 was adjustable to allow scanning of the plasma image across the slit to maximise the signal. The emission spectrum of the source plasma was measured through the semi-transparent target with and without the absorber plasma present. The self-emission of the absorber plasma in the absence of the source plasma was also recorded. All spectra were averaged over 10 shots. From these three spectra the spectral absorption of the absorbing plasma was deduced. The ablation depth per pulse was measured by the mass loss technique described in chapter 3.

Figure 4.19 shows the various spectra recorded in the region 450 – 625 nm. $I_S(\lambda)$ is the emission spectrum of the source plasma measured through the semi-transparent target without absorber plasma, and $I_{SA}(\lambda)$ is the same spectrum with the absorber plasma present. $I_A(\lambda)$ is the self-emission of the absorbing plasma in the absence of the source. $I_S(\lambda)$ and $I_A(\lambda)$ are similar, though higher laser fluence on the source target makes $I_S(\lambda)$ more intense.
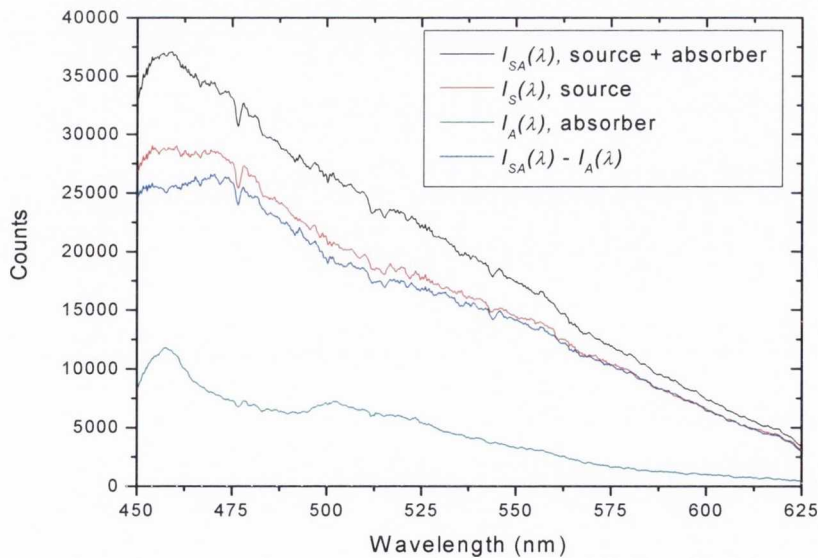

Figure 4.19 Plasma emission for both the emission and absorber plasmas in the dual laser plasma experiment.

The spectral transmission, $T(\lambda)$, of the absorbing plasma was calculated as follows:

$$T(\lambda) = \frac{I_{SA}(\lambda) - I_A(\lambda)}{I_S(\lambda)} \qquad (4.5)$$

This is shown in Figure 4.20. In the region 450 – 540 nm, the absorption falls from 10 to 5%, and at around 600 nm the absorption is negligible. The transmission is related to the net absorption cross-section σ by the following equation:

$$T = \exp(-\sigma N d) \qquad (4.6)$$

where N is the atom/ion density in the absorber plasma and d is the thickness of the plasma layer.
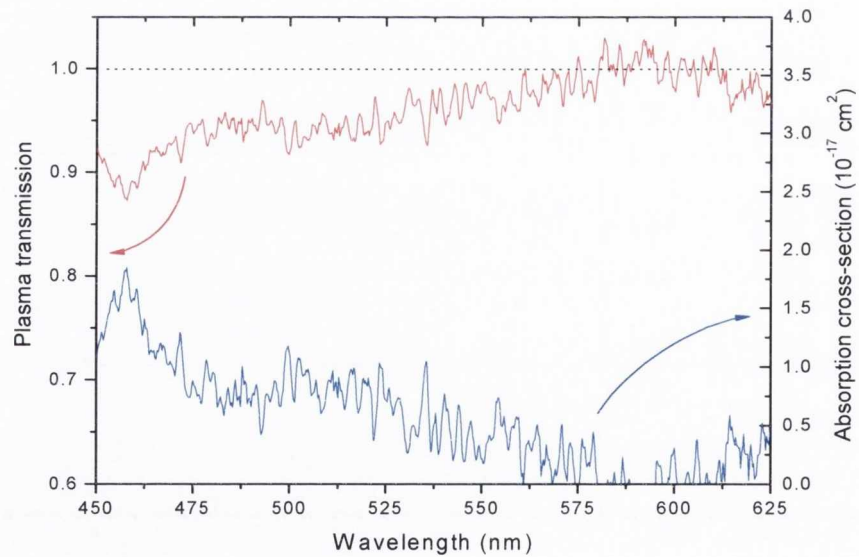

Figure 4.20 Measured plasma transmission and absorption cross section in visible region.

Since the expansion of the vapour during the laser pulse is one-dimensional, the product Nd is equal to the product of the atom density in the solid N_s and the ablation depth d_s. For Ag, $N_s = 5.866 \times 10^{22}$ cm^{-3}. The measured mass loss is 16 ng per pulse and yields an

ablation depth of 3 nm. Taking into account that ablation occurs on only 0.42 of the irradiated area of the semi-transparent target, it is estimated that the areal particle density, $Nd = 7.4 \times 10^{15}$ cm^{-2}. Using Eq. 4.6 the absorption cross-section was calculated and is also shown Fig. 4.20. In the region 450 – 540 nm, $\sigma = (0.5 - 1.5) \times 10^{-17}$ cm^{2}.

To consider which absorption mechanisms make significant contributions to the net absorption, we have calculated the optical absorption for our plasma conditions using the PrismSPECT code. The code was run in non-LTE mode using the plasma atom/ion density n_i, electron temperature T_e and the plasma thickness d as input parameters. The plasma thickness at the end of the laser pulse was estimated in the same way as in the first section of this chapter. The ion TOF signal was recorded for ablation of a bulk Ag target for the conditions under which the absorber plasma is formed. The peak time of flight was 6.6 μs and the probe was positioned at 9 cm. The peak energy is 104 eV which gives $\varepsilon_i \approx 27$ eV for $\gamma = 1.25$. Inserting this into Eq. gives a value of $c_s = 2750$ m s^{-1}. Taking the laser pulse duration as 6 ns, $Z_0 = 16$ μm. This value is smaller than the optical emission experiment but the laser pulse duration is less than half of what was before and c_s is less due to the lower fluence used. Using the value of $Nd = 7.4 \times 10^{15}$ cm^{-2} derived from the ablation depth measurement gives a value of $n_i = 4.6 \times 10^{18}$ cm^{-3} for the plasma atom/ion density. PrismSPECT was run using this value of density, $Z_0 = 16$ μm and several different values of temperature to calculate the total absorption cross-section, σ_{total}. The calculated cross sections are shown in Fig. 4.21 and compared to the experimental measurement. The calculation indicates that the plasma is of low temperature (1 eV) but there is poor agreement. There is a large absorption feature at 457 nm that the code does not account for. Due to the limited atomic data for Ag, it is hard to understand the origin of this feature. It does not correspond with any transition in Ag I while there is an Ag II transition listed at 462 nm ($4d^9 5p - 4d^8 5s^2$). This particular transition is not present in the code calculations.
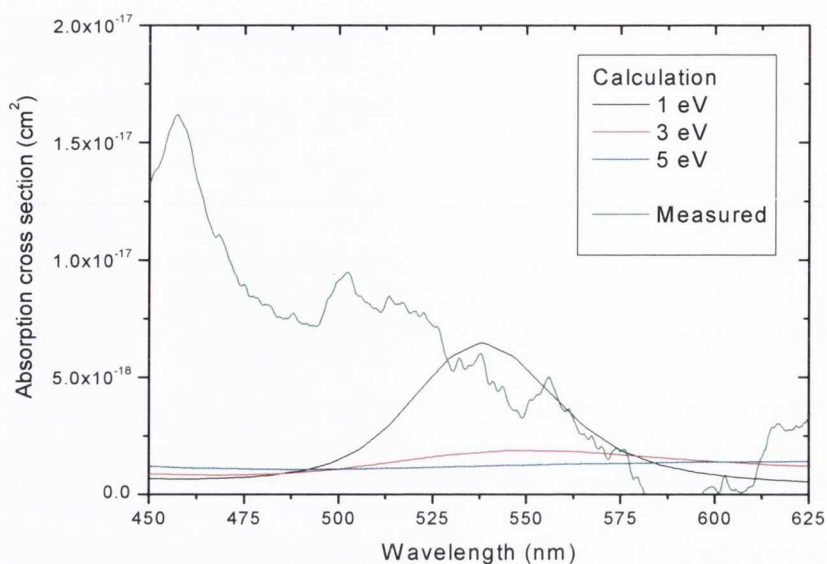
Figure 4.21 Comparison of the calculated and measured optical absorption cross section. The measured data has been smoothed compared to the same dataset presented in Fig. 4.23.

At low values of temperature, the calculated absorption spectra are quasi continuous while at higher temperatures, a complete continuum absorption is observed but at values that are lower than for low temperature. At a temperature of 1 eV the absorption peak is due to the 5d – 5p transition in neutral Ag. At a plasma temperature of 3 eV, a similar but weaker absorption feature is present but is instead due to transitions in Ag II. The code indicates that the transition responsible is $4d^9 6d – 4d^9 6p$ (545 nm). This transition is not listed in the tables of Moore or in the NIST database. At higher temperatures, the absorption is due to transitions in Ag III and IV. The laser fluence used here is close to threshold so it is unlikely that the temperature is sufficiently high to reach these ionisation stages. Again, it is not clear why the calculated and measured spectrum differ so much. One physical reason could be that assuming the lateral plasma expansion during the laser pulse will cover the holes is not fully satisfied. To cover a hole, the element of plasma must travel the distance of half the hole size. This equates to 20 μm and using the speed of sound value found from the ion signal indicates it will take the plasma at least several nanoseconds to travel this distance. This is not insignificant when compared to the laser pulse duration and the

100

camera gate time used. Therefore the holes in the transparent target may only be partially covered during the measurement.

The code also calculates the relative contribution from each of the absorption mechanisms described in chapter 2. Although the calculation and measurement compared rather poorly, the calculation can indicate which of the mechanisms is more efficient. Figure 4.22 shows the calculated spectrum at 1 eV and the contribution from bound - bound, bound-free and free-free transitions are shown. Bound-bound transitions are shown to dominate the absorption. This is an important point as the contribution of bound - bound transitions is rarely included in computational models that calculate laser absorption and radiative transfer in the plasma. For dense low temperature plasma that is formed during laser ablation the broadening is substantial so that this will have an effect over a large spectral region. Future detailed modelling of the optical properties of laser produced plasma will need to include a detailed treatment of broadened bound - bound transitions.
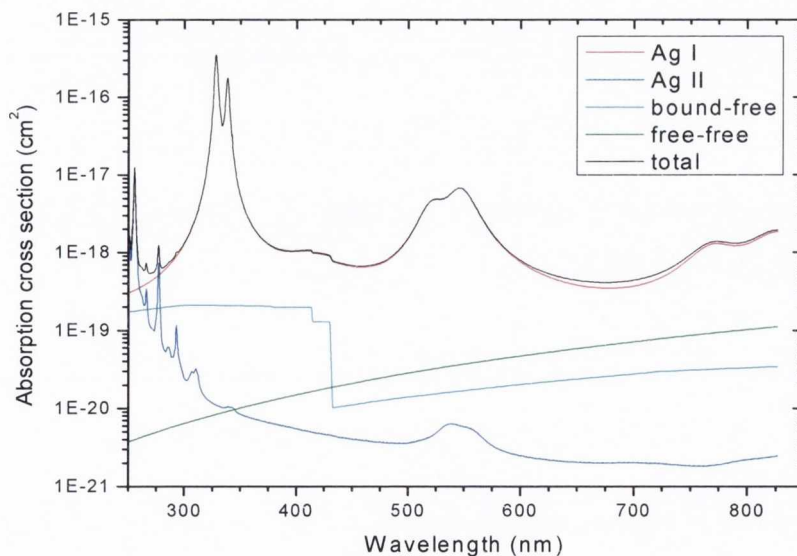

Figure 4.22 Contribution of various absorption mechanisms to overall absorption cross section.

4.4 References

[1] C.E. Moore, *Atomic Energy Levels*, Natl. Bur. Stand. (U.S.) Circ. 467, Vol. III (1958)

[2] Yu. Ralchenko, A. E. Kramida, J. Reader and NIST ASD Team (2008), *NIST Atomic Spectra Database* (version 3.1.5), Available online: http://physics.nist.gov/asd3, National Institute of Standards and Technology, Gaithersburg, MD (2009)

[3] J. C. Pickering and V. Zilio, *Eur. Phys. J. D*, **13**, 181 – 185 (2001)

[4] R. L. Kurucz, Atomic Spectral Line Database, Available online: http://www.pmp.uni-hannover.de/cgi-bin/ssi/test/kurucz/sekur.html, (2009)

[5] Ya. B. Zel'dovich and Yu. P. Raizer, *Physics of Shock Waves and High Temperature Hydrodynamic Phenomena* (Dover, New York, 2002)

[6] T. N. Hansen, J. Schou and J. G. Lunney, *Appl. Phys. A*, **69**, S601-S604 (1999)

[7] N. M. Shaikh, S. Hafeez, M. A. Kalyar, R. Ali, and M. A. Baig, *J. Appl. Phys.*, **104**, 103108 (2008)

[8] S. Djenize, A. Sreckovic and S. Bukvic, *Spectrochim. Acta B*, **60**, 1552 – 1555 (2005)

[9] N. M. Shaikh, B. Rashid, S. Hafeez, S. Mahmood, M. Saleem, and M. A. Baig, *J. Appl. Phys.*, **100**, 073102 (2006)

[10] S. S. Harilal, B. O'Shay, M. S. Tillack and M. V. Mathew, *J. Appl. Phys.*, **98**, 013306 (2005)

[11] *Principles of Plasma Spectroscopy*, H. R. Griem, Cambridge University Press (2005)

[12] M. S. Qaisar and G. J. Pert, *J. Appl. Phys.*, **94**, 3 (2003) 1468 - 1477

[13] M. E. Sherrill, R. C. Mancini, J. Bailey, A. Filuk, B. Clark, P. Lake, and J. Abdallah, *Phys. Rev. B*, **76**, 056401 (2007)

[14] G. R. Bennett, J. S. Wark, D. J. Heading, N. C. Woolsey, H. Ne, R. Cauble, R. W. Lee and P. Young, *Phys. Rev. E*, **50**, 3935 - 3942 (1994)

[15] D. J. Heading, G. R. Bennett, J. S. Wark and R. W. Lee, *Phys. Rev. Lett.*, **74**, 3616 – 3619 (1995)

[16] *Spectral Line Broadening by Plasmas*, H. R. Griem, Academic Press Inc. (1974)

[17] *Spectrophysics: Principles and Applications*, A. P. Thorne, U. Litzen and S. Johansson, Springer (1999)

Chapter 5: Plume dynamics during femtosecond laser ablation of a metal target

In this chapter the expansion dynamics of the ablation plume produced by femtosecond laser ablation of nickel are investigated. In the first section, the spatial profile of the laser beam is explored. The ablation target was positioned at the laser focus which was different to the imaging setup used for nanosecond laser ablation. The laser profile is examined to see if it could be approximated as a Gaussian and the beam dimensions on the target are found. The peak laser fluence used in the experiment could then be found.

In section 2 femtosecond laser ablation plume dynamics is studied and both the plasma and nanoparticle plumes are considered. The expansion properties of both plume components are compared with the Anisimov gas expansion model. In section 3 an irradiation scheme involving two pulses separated on ps time scales is used to influence the ablation process. The change in the ablation plume is considered as a function of delay between pulses and the physical reasons for a change in the plume condition are considered.

5.1 Laser beam spatial profile

The spatial profile of the laser pulse used for this experiment is non - uniform. The laser pulse was focused onto the target surface which was placed at the beam focus. This is different from the nanosecond experiments where an aperture was used to select a uniform portion of the beam which was then imaged onto the target. To calculate the laser fluence correctly for a non - uniform beam, knowledge of the beam spatial profile is necessary. For this experiment we make the assumption that the spatial profile of laser fluence on the ablation target can be described by a Gaussian profile. This assumption will be validated and we will calculate the maximum peak fluence that can be used. If we consider a pure Gaussian beam profile, on a 2-D surface with axes x and y, that is non-circularly symmetric and with radii $w_x(z)$ and $w_y(z)$ the intensity, $I(x,y)$ is given by

$$I(x,y) = I_0 \exp\left(-2\left(\frac{x^2}{w_x^2(z)} + \frac{y^2}{w_y^2(z)}\right)\right)$$ (5.1)

z is the distance along the plane of propagation and the beam focus position is designated z_0. I_0 is the maximum intensity at the centre of the beam. Figure 5.1 depicts the propagation of a Gaussian beam.
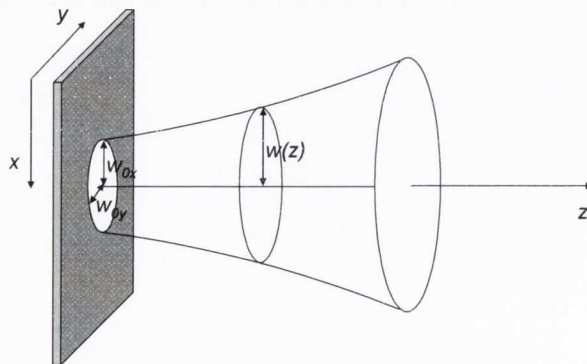

Figure 5.1 Image depicting the propagation of Gaussian beam.

If the laser pulse duration τ_l is constant over the entire beam, then we can re-write this expression as one for the fluence distribution, $F(x,y)$ at the beam focus ($z=z_0$):

$$F(x,y) = F_0 \exp\left(-2\left(\frac{x^2}{w_{0x}^2} + \frac{y^2}{w_{0y}^2}\right)\right) \tag{5.2}$$

w_{0x} and w_{0y} are the major and minor beam waist radii at z_0 and F_0 is the peak fluence. Figure 5.2 shows a spatial profile calculated using Eq. 5.2 with $F_0 = 1$.
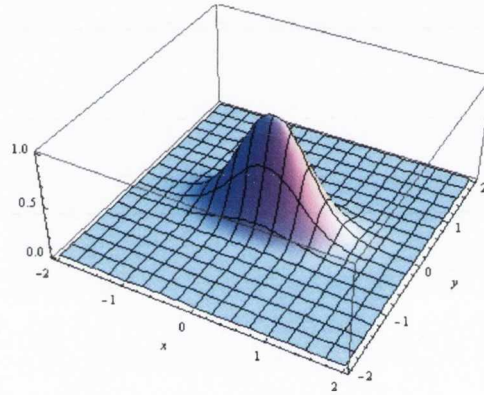

Figure 5.2 Fluence distribution of a pure Gaussian beam.

Integrating the fluence distribution over the x-y plane gives the laser pulse energy E.

$$E = \int_{-\infty}^{\infty}\int_{-\infty}^{\infty} F_0 \exp\left(-2\left(\frac{x^2}{w_{0x}^2} + \frac{y^2}{w_{0y}^2}\right)\right) dxdy = \frac{1}{2}F_0 \pi w_{0x} w_{0y}$$

An expression for the peak fluence, F_0 can then be found.

$$F_0 = \frac{2E}{\pi w_{0x} w_{0y}} \tag{5.3}$$

105

Considering that a fluence threshold for ablation exists, a threshold pulse can be defined as the one that starts ablation at its very centre (peak). If we define the energy of the threshold pulse as E_{th}, the spatial distribution of its fluence is:

$$F(x,y) = F_{th,0} \exp\left(-2\left(\frac{x^2}{w_{0x}^2} + \frac{y^2}{w_{0y}^2}\right)\right)$$

(5.4)

where

$$F_{th,0} = \frac{2E_{th}}{\pi w_{0x} w_{0y}}$$

(5.5)

The locus where the fluence falls below the threshold fluence defines an ellipse with radii x_{th} and y_{th}, centred at the pulse peak position, according to the following equation:

$$F_{th} = F_0 \exp\left(-2\left(\frac{x_{th}^2}{w_{0x}^2} + \frac{y_{th}^2}{w_{0y}^2}\right)\right)$$

(5.6)

Therefore, assuming x_{th} and y_{th} as the measured radii of the elliptical ablation spot on the target, $X_{th} = 2x_{th}$ and $Y_{th} = 2y_{th}$ where X_{th} and Y_{th} are the measured spot diameters. Figure 5.3 shows a Gaussian profile above a threshold value of $0.2F_0$ to demonstrate this idea.
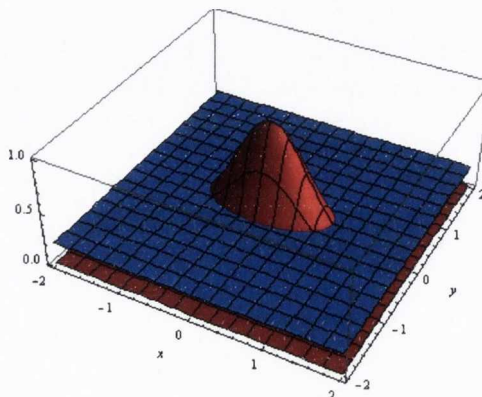

Figure 5.3 Fluence distribution of a Gaussian beam over a threshold value of $0.2F_0$.

Since Eq. 5.6 holds for each point of the ellipse it is valid also for the two coordinates $(x_{th},0)$ and $(0,y_{th})$. Working through for X_{th} and Y_{th} we get:

$$X_{th} = \sqrt{2w_{0x}^2 ln\left(\frac{F_0}{F_{th}}\right)} = \sqrt{2w_{0x}^2 ln\left(\frac{E}{E_{th}}\right)}$$

(5.7)

$$Y_{th} = \sqrt{2w_{0y}^2 ln\left(\frac{F_0}{F_{th}}\right)} = \sqrt{2w_{0y}^2 ln\left(\frac{E}{E_{th}}\right)}$$

One can also consider the beam spot area, $\sigma_0 = \pi w_{0x} w_{0y}$ and the threshold beam spot area, $\sigma_{th} = \pi x_{th} y_{th} = \pi (X_{th} Y_{th}/4)$, so the following relation is also valid.

$$\sigma_{th} = \frac{\sigma_0}{2} ln\left(\frac{E}{E_{th}}\right)$$

(5.8)

Eq. 5.7 and 5.8 can be used to fit the experimental data for the elliptical ablation spot dimensions as a function of the pulse energy E. If a linear dependence exists between the square of the spot diameter and the $ln(E)$ then the beam can be considered Gaussian. To check this for our experimental setup, where the laser used was operating at a wavelength of 527 nm and pulse duration of 250 fs, the minor and major diameters of the ablation spots were measured as a function of energy. This was done under several different conditions. Firstly, burns were made on a fresh Ni surface as a function of energy. This was done for both 2 shot and 10 shot exposures. Secondly, single shot burns were made on laser burn paper and finally, the size of craters formed by ablation of a stationary Ni target for a fixed time, were measured to extract the laser spot size as a function of energy. Figure 5.4 shows a laser ablation spot on Ni for (a) 2 shots (b) 10 shots and (c) for an ablation

107

crater where 132 shots were used. The laser fluence used was 0.7 J cm^{-2} and the images were recorded using an optical microscope.
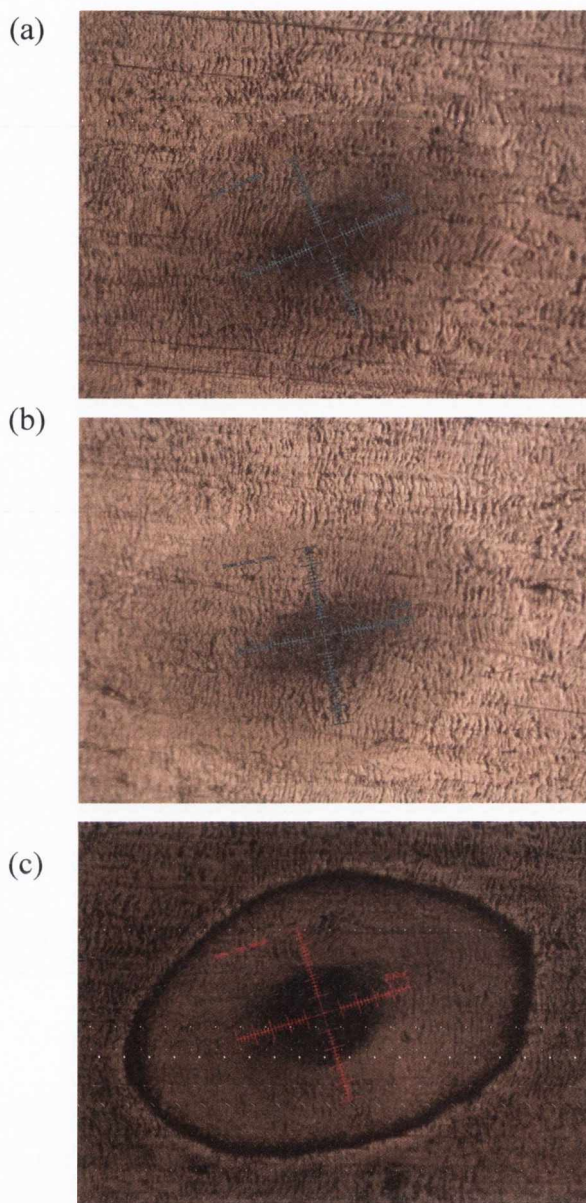
(a)

(b)

(c)

Figure 5.4 Optical microscope images of the ablation spots formed on Ni for E = 424 μJ and for (a) 2 shot (b) 10 shot and (c) 132 shot exposure.

The minor and major diameters were then found from the images and a plot of X_{th}^2 and Y_{th}^2 vs. $ln(E)$ was made to show that the beam is well described by the Gaussian analysis above and to extract the beam spot radii w_{0x} and w_{0y}. These are shown below.
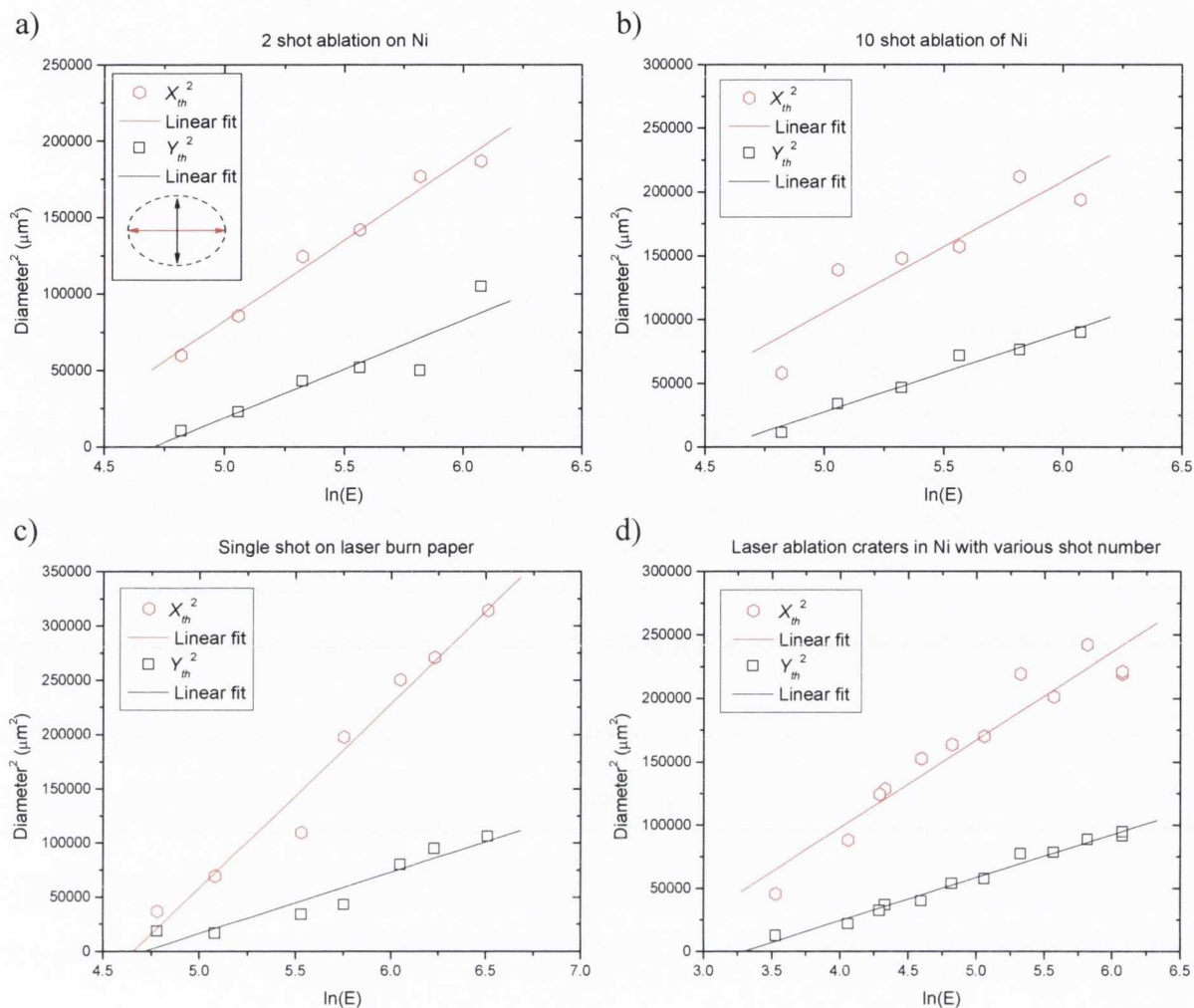
Figure 5.5 Plots of the diameter^2 vs. the ln(E) for the minor (black) and major (red) axis of the ablated spots from a) 2 shots on Ni b) 10 shots on Ni c) single shot on laser burn paper and d) laser drilled craters.

For each set of measurements a value of w_{0x} and w_{0y} can be found from the slope of each linear fit and the damage threshold, E_{th}, can be found from the intercept. The above plots show that the beam used in our experiment agrees with Eq. 5.7 and the Gaussian analysis above can be used to find the fluence used in the experiment. Table 5.1 summarises the values extracted from the data presented in Fig. 5.5

	Minor axis (Y_{th})		Major axis (X_{th})	
	w_{0y} (μm)	E_{th} (μJ)	w_{0x} (μm)	E_{th} (μJ)
2 shot - Ni	179	110	230	68
10 shot - Ni	176	95	227	53
1 shot - paper	168	111	291	106
Craters - Ni	131	14	187	27

Table 5.1 Summary of beam spot parameters extracted from the beam spot analysis.

From table 5.1 consistent values are found for w_{0x} and w_{0y} from the 2 and 10 shot ablation on Ni and the single shot on burn paper. The exception to this is the value for w_{0x} found from the single shot on burn paper. This value is larger than that found from the ablation on Ni measurements. The reason for this is unclear but could be due to a change in angle of incidence of the laser pulse. The value of E_{th} found during this measurement is also significantly larger than the corresponding values found from measurements on Ni. The analysis of the ablation crater diameters ((d) in Fig.5.5) also produced different results from the 2 and 10 shot analysis. The cause for this is most likely due to the fact that when the craters were being formed a different number of shots were used to form each crater. The shot number used was chosen in such a way to ensure a sufficiently deep crater was formed that could be easily measured using white light interferometry (chapter 3). The shot number was changed from 132 to 1650 when the laser energy was changed from the maximum output energy to the minimum energy used. It is well known from laser machining of materials that multiple pulses on a surface can change the damage threshold E_{th}. This is known as an 'incubation' effect [1]. One can account for this effect by treating E_{th} in Eq. 5.7 as being dependant on the shot number N. The shot-number-dependent threshold energy, E_{th}^{N} can be found from the following equation;

$$E_{th}^{N} = E_{th}^{1} N^{s-1}$$
(5.9)

E_{th}^{1} is the damage threshold for one shot and s is the incubation factor that determines the degree of incubation. For $s = 1$ there is no incubation effect. The ablation spot diameter can then be determined by substituting Eq. 5.9 into Eq. 5.7 which gives:

$$X_{th}, Y_{th} = \sqrt{2w_0^2 \ln\left(\frac{E}{E_{th}^1 N^{s-1}}\right)} = \sqrt{2w_0^2 \ln\left(\frac{EN}{E_{th}^1 N^s}\right)} \qquad (5.10)$$

In the equation, above X_{th} and Y_{th} are as before and w_0 corresponds to w_{0x} or w_{0y} depending which axis, x or y, is being considered. Taking a value of $s = 0.94$ [2] and plotting X_{th} and Y_{th} vs. $ln(EN/N^{0.94})$ values of $w_{0x} = 192$ μm and $w_{0y} = 135$ μm were found for the beam radii. These values are not very different from the non - incubation analysis and are the beam dimensions are still much smaller than those found with the low shot number measurements. This indicates that the incubation analysis doesn't account for the change in diameter during crater formation. This could possibly be due to the value of s we are using as there is only a small variation in N/N^s, which changes from 1.22 to 1.35, as the shot number is increased from 132 shots (max. fluence) to 1650 (min. fluence used), as the laser fluence is decreased. Other researchers [3] have used different values for s for different elements but extracting the value of s for our experiments is beyond the scope of this thesis. If we apply the incubation model to the 10 shot ablation spots on Ni, the resultant values for the beam waist radii are the same as before but the damage threshold values are in better agreement with the value extracted from the 2 shot measurements. This shows that for low shot number N, the incubation model can account for the change in the ablation spot with changing N. As a result of this we have chosen to adopt the beam parameters extracted from the 2 shot ablation spots on Ni because, when the incubation analysis is invoked, the 2 and 10 shot data give very similar results. The single shot burns on paper are not used as the Ni measurements will be closest to our experimental situation

111

and although the value of w_{0y} from this dataset agrees with that from the 2 shot on Ni dataset, the value of w_{0x} does not. For the measurements on craters the values are very different and cannot be accounted for by the simple incubation model so this dataset is not considered. Table 5.2 shows the adjusted values found when the incubation analysis was applied.

	Minor axis (Y_{th})		Major axis (X_{th})	
	w_{0y} (μm)	E_{th} (μJ)	w_{0x} (μm)	E_{th} (μJ)
2 shot - Ni	179	115	230	61
10 shot - Ni	176	109	227	71
1 shot - paper	-	-	-	-
Craters - Ni	135	43	192	22

Table 5.2 Summary of the beam spot parameters found by including the incubation effect.

From the dataset from Fig. 5.5 (a), values of 230 μm for w_{0x} and 179 μm for w_{0y} were found. The corresponding values for E_{th} are 61 μJ and 115 μJ respectively. It is somewhat surprising that these two values would be so different perhaps indicating that the Gaussian approximation is less well satisfied in one dimension compared to the other. This is reflected in all the data sets in Fig. 5.5 except maybe for dataset (c) where the effect is not as pronounced. The angle of incidence of the laser pulse is 45° so that the pulse will be elongated along one direction, the x axis in this case. In a Gaussian or near Gaussian beam profile the damage threshold value should be the same when both axes are considered. Instead of looking at the minor and major diameters separately the threshold spot area is considered and compared to Eq. 5.8 to determine whether a linear relation exists and to extract w_{0x}, w_{0y} and E_{th}.
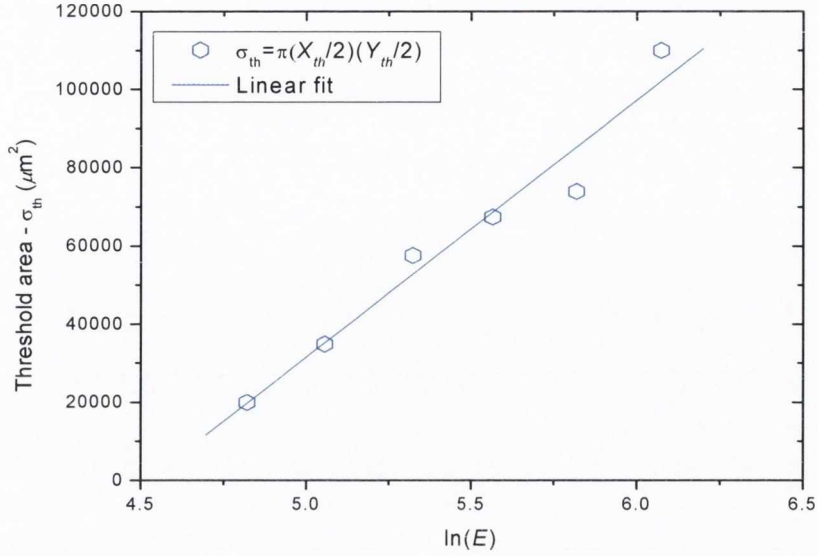
Figure 5.6 Beam threshold area vs. ln(*E*) for the 2 shot on Ni dataset as presented in Fig. 5.5 (a).

The value of the beam spot area, σ_0 and the damage threshold, E_{th} can be found from the slope and intercept of the linear fit above. From the fit above $\sigma_0 \approx 131{,}450 \ \mu m^2$ and $E_{th} = 92 \ \mu J$. If we consider that $X_{th} = Y_{th}/\cos(45°)$ then the spot radii can be found and are as follows; $w_{0x} = 243 \ \mu m$ and $w_{0y} = 172 \ \mu m$ which are close to the values extracted from analysing each axes separately as in Fig. 5.5 (a). The spot area σ_0 in cm^2 is $1.3 \times 10^{-3} \ cm^2$ and Eq. 5.3 can be used to find the peak laser fluence. For the experimental setup used in the following experiments, the maximum on target energy is $\approx 500 \ \mu J$ which gives a maximum peak fluence, $F_p \approx 0.75 \ J \ cm^{-2}$.

5.2 Ablation plume dynamics during femtosecond laser ablation of nickel

5.2.1 Ablation depth measurements

The maximum ablation depth was measured using a scanning white light interferometer that was described in chapter 3. Figure 5.7 shows a white light interferometry map of the ablation crater produced by 231 laser shots with 260 μJ each, where the maximum fluence in the centre of the ablation spot was $\approx$ 0.4 J cm^{-2}.
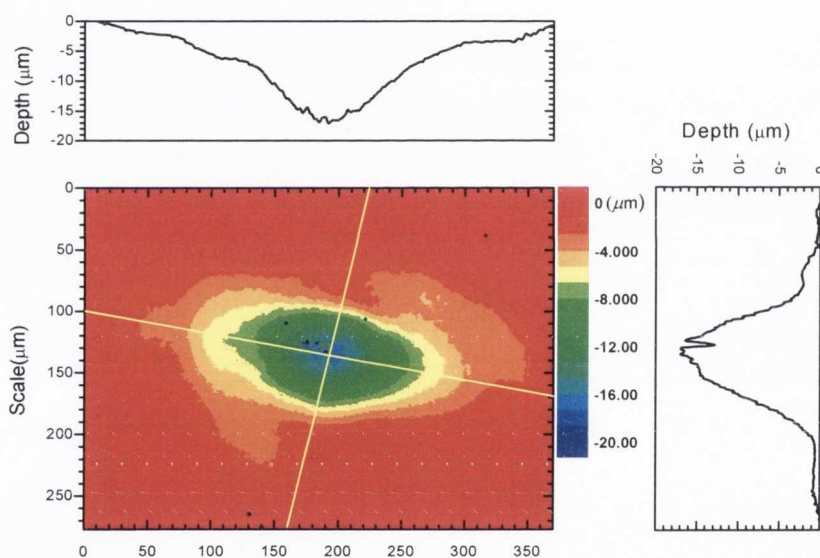

Figure 5.7 Surface profile of a crater formed from ablation at $F_p \approx$ 0.4 J cm^{-2}. The number of shots used in this case was 231 at 33 Hz.

The maximum ablation depth per pulse for the above case is $\approx$ 75 nm. Figure 5.8 shows the fluence variation of the maximum ablation depth. It is well established that in ULA the mechanisms governing the ablation depth depend on the laser fluence, F. Close to the ablation threshold the depth distribution of temperature in the material is related to the optical absorption of the laser, while at higher fluence it is necessary to account for electronic heat diffusion [4].
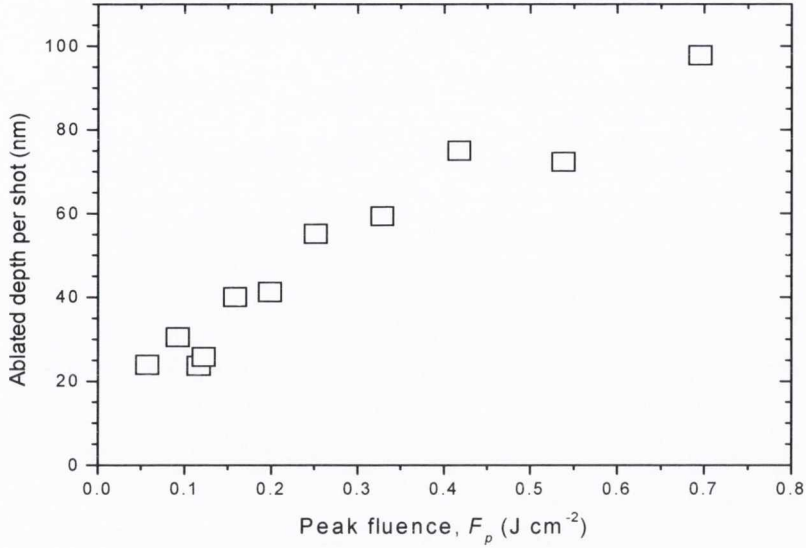
Figure 5.8 Experimentally measured maximum ablated depth as a function of peak laser fluence.

Two different models have been formulated to describe the ablated depth dependence on laser fluence for femtosecond ablation. The model of Nolte *et al.* considered a solution to the two temperature model of heat diffusion [4] which yields a logarithmic dependence of the ablation depth on the applied laser fluence. For low fluence, where the depth is determined by the optical absorption of the laser, the ablated depth per pulse is given by:

$$d_{opt} = \delta \ln\left(\frac{F}{F_{th}}\right) \qquad (5.11)$$

where δ is a the optical absorption depth and F_{th} is the threshold fluence for ablation. For nickel, our material of interest, $\delta = 13.5$ nm. The threshold fluence can be estimated from $F_{th} = E_c\delta/(1-R)$. For nickel this value is 0.15 J cm^{-2}. As $R = 0.51$ is the reflectivity of the nickel at the laser wavelength and for p-polarisation. E_c is the critical energy per volume required for ablation and is set equal to $\rho\Omega_{vap}$ where density ρ is the density (for Ni, $\rho = 8,910$ kg m^{-3}) and Ω_{vap} is the latent heat of vaporization ($= 6.45 \times 10^6$ J kg^{-1}). For Ni $E_c =$

5.75x10^{10} J m^{-3}. At higher fluence, electronic heat conduction becomes significant and the ablation depth is described by:

$$d_{heat} = l \ln\left(\frac{F}{F_{th}}\right)$$ (5.12)

Here l is the effective heat penetration depth and is given by:

$$l = \left(\frac{k_e}{C_i} \tau_a\right)^{\frac{1}{2}}$$ (5.13)

where k_e is electron thermal conductivity, C_i lattice heat capacity respectively and τ_a is the duration of the laser ablation. In the Nolte interpretation τ_a is taken to be equal to the electron-phonon coupling time. The value of l for nickel found from Eq. 5.13 is 10.5 nm which is smaller than the optical absorption depth. This is contrary to the model interpretation where the value of l is deemed to be larger than δ resulting in two different fluence regimes. It seems that taking the ablation time, τ_a, to be equal to the electron phonon coupling time is incorrect and given that the coupling time for nickel is small (5 ps), this results in an unreasonable value of l. In Nolte's original study copper was the material under investigation and the value of l used in their study was 60 nm which was much larger than their value of δ so that their interpretation matched their observed experimental trend.

Vestentoft and Balling [5] have also considered the ablated depth dependence on the laser fluence. In their study, they have simplified the two temperature equations to a single heat diffusion differential equation for which the following solution is well known.

$$T(z,t) = \frac{2(1-R)F}{C} \left(\frac{C}{4\pi k_c t} \right)^{\frac{1}{2}} \exp\left(-\frac{Cz^2}{4\pi k_c} \right) \tag{5.14}$$

Solving the above equation for the time at which the maximum temperature is reached at a given depth in the target an equation for the maximum ablated depth can be found that is linearly dependant on the laser fluence.

$$d_{heat} = \sqrt{\frac{2}{\pi e}} \frac{(1-R)F}{\rho \Omega_{vap}} = \delta \sqrt{\frac{2}{\pi e}} \frac{F}{F_{th}} \tag{5.15}$$

Figure 5.9 shows the calculated ablation depth using the Vestentoft and Balling model and compares it to the experimental data.
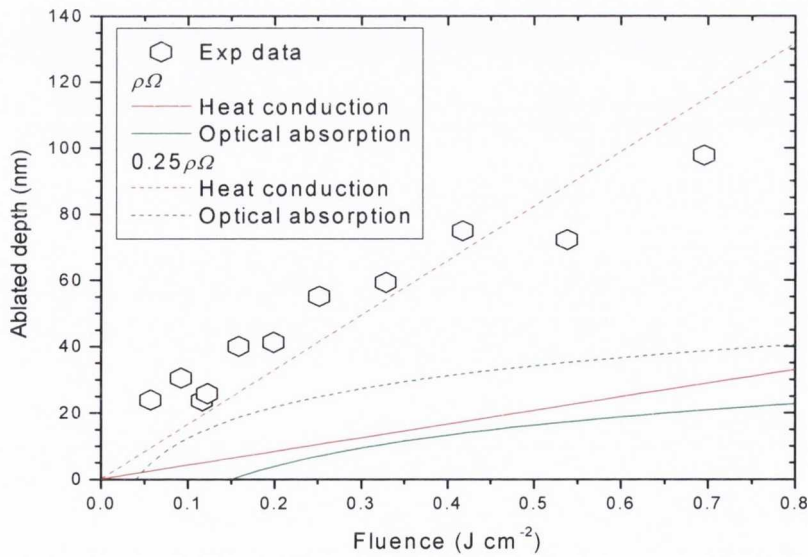

Figure 5.9 Comparison of ablation models to experimental data. The data points are the experimentally measured maximum ablation depth as a function of peak fluence. The solid and dashed lines are the calculated depths which are described in the text.

In Fig. 5.9 the calculated depth (solid lines) for the optical absorption (green) and heat conduction (red) equations are shown. The model estimates fall significantly below the

experimental measurements. The critical energy loading, E_c for ablation may be lower than the value given by the heat of vapouristion. Reducing the value of R increases the calculated depth, but even considering total absorption of the laser pulse is not sufficient to reproduce the experimental values. If the value of E_c is reduced the calculated depth will increase. To account for the measured data the value of E_c must be reduced to about $0.25\rho\Omega_{vap}$. This calculation is shown in Fig 5.9 by the dashed lines. The estimated value of F_{th} will change as a result of the reduced value of E_c so that F_{th} now becomes 0.04 J cm^{-2}. This value agrees with the value quoted by Amoruso [6]. The fluence variation of ablation depth measured here is similar to measurements in Ref 6, which were close to the predictions of a Molecular Dynamics simulation.

It seems that both models in their basic form underestimate the measured ablation depth. To vaporise a layer of depth, d, complete separation of all the atoms is required. To do this, the energy input needed into the layer will be cohesive energy times the number of atoms in the layer. It is now understood that ablation is not atomic but multi-component and that most of the ablated material is released as nanoparticles, so less energy is required to ablate the layer. It is not clear from the data which of the two types of dependence, linear or logarithmic, is more appropriate to use. In light of the molecular dynamic modeling of the ablation mechanisms this point is perhaps no longer relevant. Other models based on high intensity laser irradiation such as that by Carusso and Gratton [7] also underestimate the ablation depth when compared against our experimental measurements. Their model, although developed for very high fluence ablation, can be used to estimate the temperature of the ablated material. For the fluence range used in this study this model predicts a temperature in the range of 1.5 – 7 eV.

5.2.2 Plasma plume expansion

The plasma part of the ablation plume was measured by recording the ion signal using the negatively-biased Langmuir probe. Figure 5.10 (a) shows ion signals recorded as a function of angle θ away from the target normal for peak fluence, $F_p \approx 0.6$ J cm^{-2}. As expected for an Anisimov-type expansion, the amplitude of the ion signal and the expansion velocity fall as the detection angle is increased. Figure 5.10 (b) shows the fluence variation of the ion time of flight. As the fluence is increased, the ions signal increases accordingly and in general, the time of flight of the peak signal is reduced indicating a faster expansion.
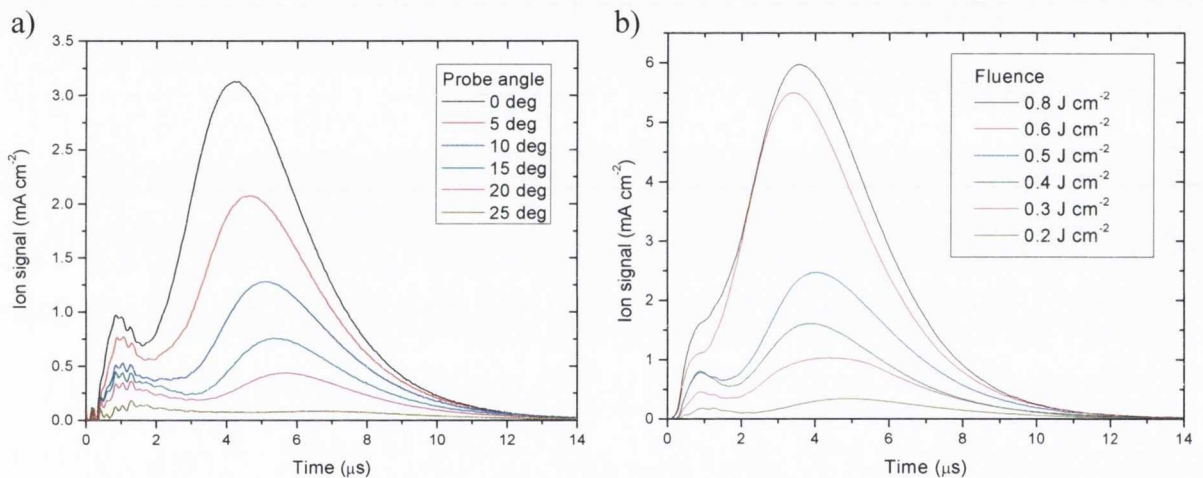

Figure 5.10 (a) Ion time of flight signals as a function of probe angle for $F_p \approx 0.6$ J cm^{-2}. (b) Ion time of flight signals as a function of laser fluence measured normal to the target surface.

There are two components in the ion signal: a small amplitude fast signal followed by a much larger slower signal. The second component is due to Ni ions formed when target regions near the surface are ablated as plasma. The nature of the faster peak is less clear, but it has been previously observed and assigned to low-Z contamination of the target surface [8]. To see if this is the origin of the fast signal in our experiment the following tests were carried out. With the laser running at 33 Hz the signals are as in Fig 5.10. However, when the target rotation is turned off the fast signal disappears. It seems that ablation on the same spot at 33 Hz is sufficient to keep the surface contamination

below our detection limit. Again with the target stationary, if the laser is blocked for five minutes and then unblocked, the first shot produces a large amplitude fast peak. The amplitude falls below detection over the next few shots. This behavior would seem to suggest that the contamination may derive from the vacuum chamber rather than the target itself. We also investigated the possibility of estimating the ion mass of the fast peak by orienting one of the probes parallel to the plasma flow directly and comparing the signal ratios of the two probes for the two peaks. Recent work [9] has shown that for a negatively-biased planar probe lying parallel to the plasma flow the ion current varies as $(V_b/m_i)^{1/2}$, where V_b is the bias voltage and m_i is the ion mass. Then comparing the parallel-to-perpendicular signal ratios for the two peaks shows the ion mass for the fast peak is due to material with a lower mass than Ni. It can also be noted from Fig. 5.10 that the fast signal falls less rapidly with increasing angle when compared to the main peak, indicating a wider angular distribution.

To simplify the analysis of the TOF signals, the contamination peak was removed by fitting the overall signal with the two pulse functions shown in Fig. 5.11 (a) and then subtracting the fast signal. The angular variation of average ion energy is shown in Fig. 5.11 (b) for $F_p = 0.6$ J cm^{-2}.
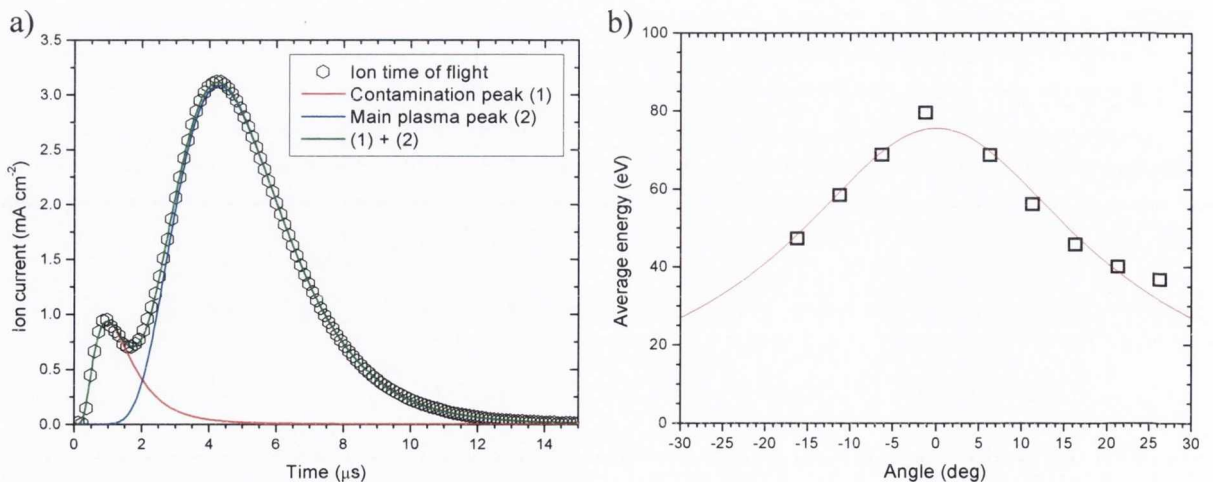

Figure 5.11 (a) Ion time of flight normal to target for ablation at a fluence of 0.6 J cm^{-2}. The time of flight is resolved into two separate components. (b) The average ion energy as a function of probe angle calculated by considering the main component of the TOF.

The average ion energy normal to the target is greatest indicating a forward peaked expansion in agreement with the Anisimov interpretation. The average ion energy for the fluence variation of the ion signal (Fig. 5.10 (b)) was also calculated. The average energy at a low fluence of 0.1 J cm^{-2} was 35 eV. At a maximum fluence of 0.8 J cm^{-2} this value increased to around 100 eV. The ion energy distribution and average energy dependence on laser fluence in the normal direction are shown if Fig. 5.12 (a) and (b).
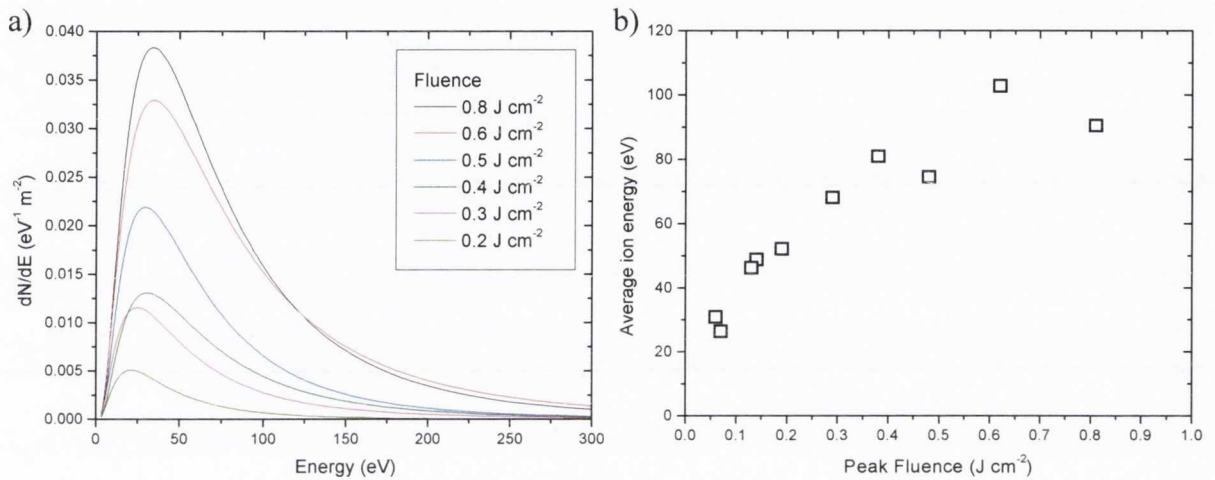
Figure 5.12 (a) Ion energy distributions as a function of peak fluence. (b) Average ion energy calculated from the ion energy distributions.

The TOF signals were integrated to find the net ion charge collected by the probe. The angular variation of this quantity is plotted in Fig. 5.13 for both the faster (a) and slower signals (b). As noted above, the distribution of the faster lower-Z signal is wider. A similar effect has been observed in ns laser ablation of LiNbO$_3$ where the Li had a wider distribution than Nb [10].
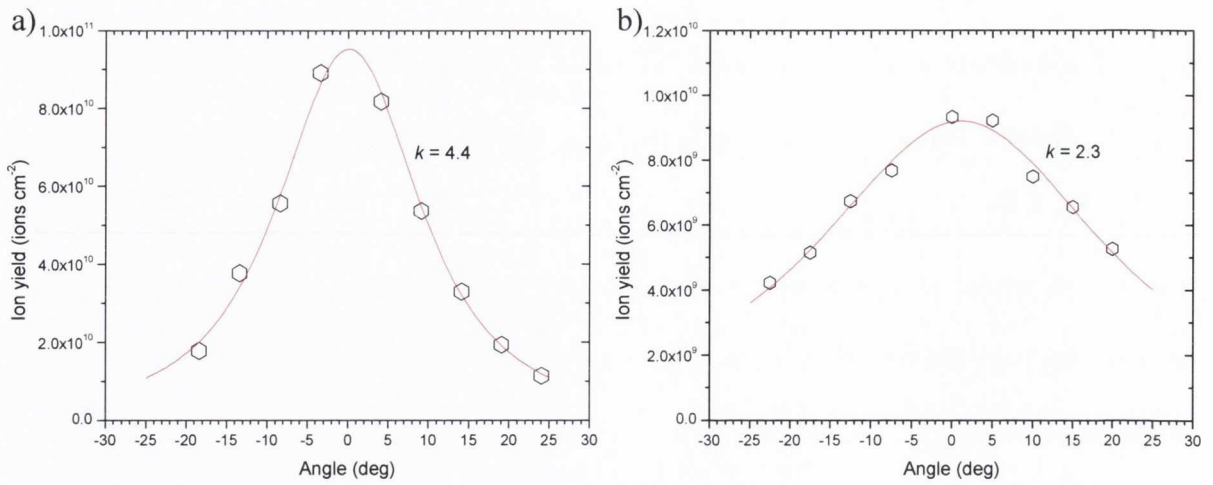
Figure 5.13 (a) Angular variation of the ion yield for the main Ni plasma component. (b) The angular variation of the ion yield for contamination component of the ion TOF.

Fitting the angular distributions to Eq. 2.21 (chapter 2), values of $k_{zy} \approx 4.4$ for the aspect ratio of the main ion component and 2.3 for the contamination component were found. In fact the angular distribution for the integrated overall signal is very close to that of the main peak on its own. Figure 5.14 shows how k_{zy} and the FWHM of the integrated ion signal vary with F_p. Near threshold $k_{zy} \approx 3.6$ but increases to ≈ 4.7 at 0.8 J cm^{-2}.
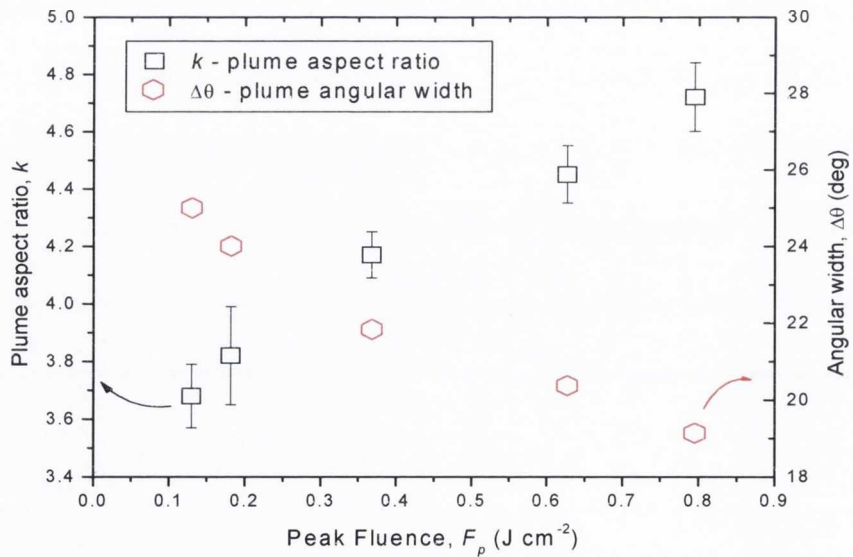

Figure 5.14 Plume aspect ratio, k and angular width $\Delta\theta$ as a function of peak laser fluence F_p.

By comparing the measured k-values of the plasma part of the ablation plume with the predictions of the Anisimov model, we can estimate the thickness of the plasma layer when

122

the adiabatic expansion commences. Figure 2.10 showed how k_{zy} depends on the layer thickness Z_0 and the value of the adiabatic constant γ for a gas cloud with a lateral dimension ratio of $Y_0/X_0=0.5$ ($X_0=200$ μm). These values were chosen to match the dimensions of the ablation spot at 0.6 J cm^{-2} for this experiment. The region corresponding to our measurements lie approximately between $k = 3 - 5$. The k-value depends strongly on γ, the value of which is rather uncertain. However, taking $\gamma = 1.25$ suggests that $Z_0 \approx 100 - 1000$ nm. The value of Z_0 for 0.6 J cm^{-2} can be estimated according the following scenario. During the laser pulse, the energy is deposited within the optical absorption length with minimal heat diffusion. Thus, at the end of the pulse the energy density near the surface will be ≈ 15 eV per atom. In the next phase electron conduction will run concurrently with the propagation of a rarefaction wave at the sound velocity ($c_s \approx 2 \times 10^3$ m s^{-1}) into the target, and the vapour will move away at a maximum velocity of $2c_s/(\gamma-1)$. The transit of the rarefaction wave through a region of the target will terminate heat conduction into the target from that region. Taking the thickness of target material which is transformed to vapour to be 15 nm, the rarefaction wave will reach the inner boundary of this layer after about 7 ps. At this time the layer is ≈ 135 nm thick, which agrees with the estimate from the shape of the plasma plume. These estimates are broadly consistent with MD simulation of ULA ablation of Ni at 0.6 J cm^{-2} by Amoruso et al. [6]. This simulation showed that a layer at 5 nm below the target surface commences to evolve adiabatically at about 10 ps.

It is also of interest to consider in detail the shape of the ion TOF signal. The Ni ion signal in the forward direction at 0.6 J cm^{-2} is shown in Fig. 5.15. The ion energy at the TOF corresponding to maximum ion flux is 74 eV. This value corresponds to an energy per particle $\varepsilon_p = 17$ eV in an Anisimov-type expansion with $\gamma = 1.25$. Using these values, the calculated TOF signal is narrower than we observe. This is shown in Figure 5.15. This may suggest that the initial plume is inhomogeneous with respect to energy per particle. Perhaps it is not surprising that the initial plasma plume is somewhat inhomogeneous when

we consider that as the rarefaction wave moves into the heated target regions lying deeper will unload with lower energy density than regions closer to the surface.
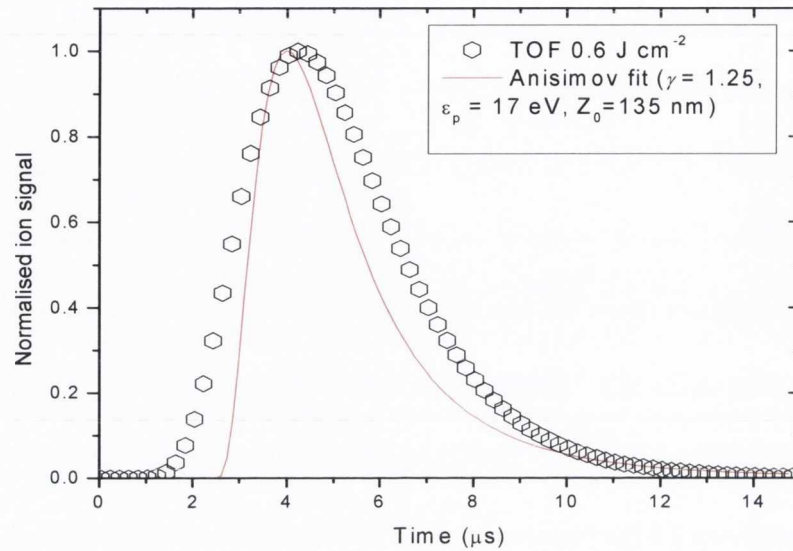

Figure 5.15 Ion TOF signal fitted using Anisimov model. The data points are the measured TOF at 0.6 J cm^{-2}. The fit is a calculation for an average energy per particle of 17 eV found from the measured ion TOF.

5.3.3 Nanoparticle plume dynamics

The angular distribution of the overall ablation plume was recorded by making a deposit on a curved transparent substrate located at 7.7 cm from the target and measuring the spatial distribution of thickness by optical transmission. This technique is described in chapter 3. The number of laser shots was varied according to the fluence used. Figure 5.16 (a) shows the angular variations of film thickness for 118,800 shots at 0.15 J cm^{-2} and 15,840 shots for $F_p = 0.7$ J cm^{-2}.
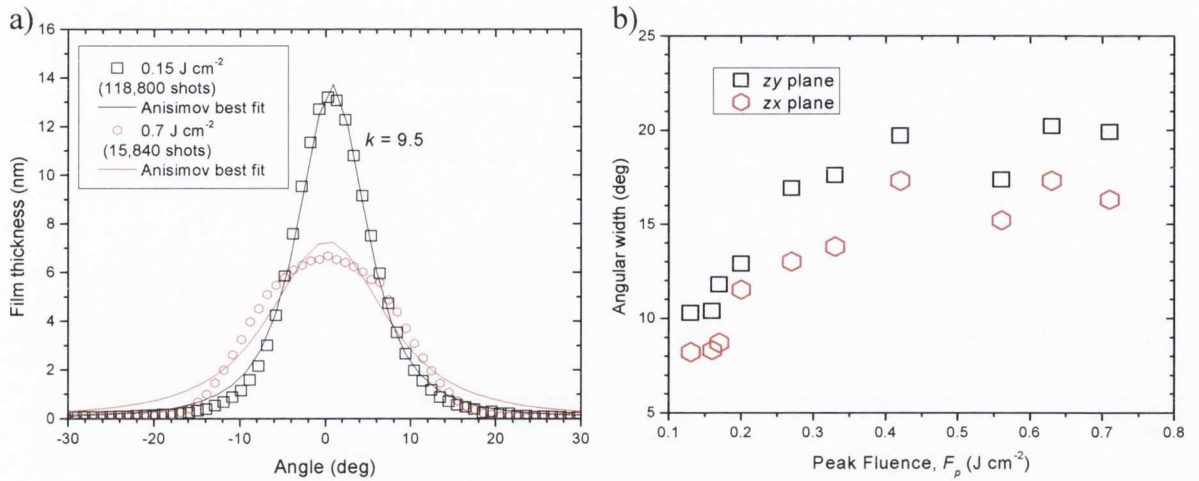
Figure 5.16 (a) Angular distribution of deposited material for a fluence of 0.15 (black) and 0.7 J cm^{-2} (red). The solid lines are best fits to the respective data sets using Eq. 2.21. (b) The angular width of the deposits, in the *zy* and *zx* plane, as a function of the F_p.

The graph also shows fits using the distributions expected for an Anisimov-type expansion. The fit for the lower fluence case is very good and yields a k_{zy} value of 9.5 which is larger than the value of 3.7 for the plasma plume at the same fluence. This behaviour is maintained up to fluence values of ≈ 0.3 J cm^{-2}. The fit to the thickness distribution for the high fluence case yields a value of $k = 5.6$ but the distribution does not correlate well with the Anisimov fit. With the deposition technique we can measure the distribution in both the *zx* and *zy* planes. Figure 5.16 (b) shows a plot of the FWHM angular width, $\Delta\theta$, of the deposit as a function of peak laser fluence. The distributions are slightly wider in the *zy* plane reflecting the fact that the minor radius of the elliptical ablation spot lies along the *y*-axis. The angular widths increase with fluence in the region 0.1 to 0.4 J cm^{-2} then remain rather constant.

Before discussing the physical process that may cause the fluence behaviour of the deposition, it is useful to examine to how the ablated material is partitioned between ionised and non-ionised material. Since the angular distributions of both the ion flux and the deposition are known we can calculate the ion yield and the deposition yield as a function of laser fluence; this is shown in Fig. 5.17.
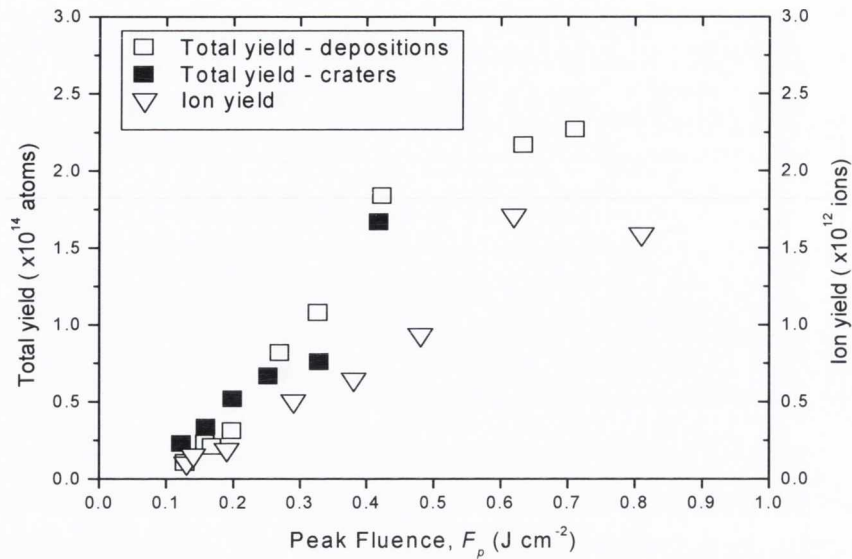
125

Figure 5.17 The ion yield and the total ablation yield as a function of F_p. For the total yield data is included from analysis of the craters and the deposits. High fluence data points for the crater analysis are not included because at higher energies not all of the ablation crater could be imaged.

This figure also shows the fluence variation of the number of ablated atoms. This was determined by integrating the crater depth maps to find the volume removed and then dividing by the number of laser shots. There is agreement between the ablation yield and the overall deposition; it seems that all the ablated material is deposited. The ion yield corresponds to < 1% of the ablated material, irrespective of the laser fluence used.

There are no reports on the physical description of the expansion of the NP material produced in ULA to dimensions much larger than the ablation depth or spot size. It is not clear if an Anismov - type description is appropriate, or what value of the adiabatic index should be used. Nevertheless, we can note that near the ablation threshold the angular distribution of deposition fits closely to the Anisimov profile. It can also be noted that the ion yield is much less than the total deposition, consistent with the earlier conclusion that the ablated material is predominately comprised of NPs. Thus we can assume that the angular distribution of the deposition is close to that of the NPs.

126

Considering the fit to the deposition at 0.15 J cm^{-2}, the ablation depth at this fluence is $\approx$30 nm. MD simulation of ULA indicates that when the material at the limit of ablation undergoes phase decomposition the overall density of the NP material is a few times lower than solid density, and the thickness of the NP layer is roughly equal to a few times the ablation depth. Taking 100 nm for this value, Fig. 2.10 implies that γ is approximately 1.25 for $k = 9.5$. This is the same value that was applied to the ions but the physical reason why the same γ could apply to both plumes is not clear or even if it is valid to do so.

The reason for the change in the angular distribution of the deposition observed above 0.3 J cm^{-2} (Fig. 5.16) is not obvious at this stage; however, the following can be offered as a possible explanation. The ion energies measured by the ion probe are sufficient to cause self-sputtering of the growing film. This effect will be most pronounced in the centre of the profile where the ion energies are highest; which would act to flatten the profile, as is observed. However, it seems that the ion fraction is too small to cause an observable effect. We might also consider if the pressure in the plasma plume can influence the expansion of the NP plume as it emerges from the ablation spot. The pressure at any point in the plume, $p(x,y,z,t)$ can be found from Eq. 2.18 from the Anisimov model. If we consider the point at which adiabatic expansion begins ($X,Y,Z = X_0,\ Y_0,\ Z_0$) the pressure equation reduces to the following form:

$$p = \frac{\varepsilon_p N}{0.72 X_0 Y_0 Z_0} \tag{5.16}$$

Knowing the ion yield, the energy per ion at 0.6 J cm^{-2}, and taking an estimate of plasma dimensions at the onset of the adiabatic expansion, the pressure due to the ions at the inner surface of the plasma is about 3 GPa. This can be compared with the critical pressure of Ni which is $\approx$ 1.1 GPa, which is indicative of the pressure in the NP material at

this time [11]. Thus we can expect that the pressure due to the plasma will have an influence on the hydrodynamic evolution of the NP material. The number of ions and the energy per ion both increase sharply as the fluence is raised from the ablation threshold to 0.6 J cm^{-2}. Thus, perhaps it is not surprising that we begin to see an influence of the plasma pressure on the NP expansion in this fluence range, though detailed hydrodynamic modelling will be necessary to confirm this conjecture. It should also be mentioned that in recent hydrodynamic modelling [12] of double-pulse ULA it was observed that absorption of the second pulse in the nascent atomic plume produced by the first produces a plasma which generates a pressure pulse that acts to impede the outflow of underlying target material and thus reduces the ablation depth.

5.3 Double pulse femtosecond laser ablation of nickel

With the aim of making femtosecond laser ablation a flexible material fabrication technique it will be necessary to influence the ablation process to exert an active control over the ablated species. To date there have been some studies that have looked at changing the ablation conditions, but it was observed that the nature of material removed, specifically the size distribution of emitted nanoparticles, does not change much. In a previous study, Amoruso *et al.* [13] deposited nanoparticles using single pulse femtosecond laser ablation and changed the laser wavelength (353, 527, 800 and 1054 nm), the pulse duration (100, 300 and 900 fs) and the laser fluence during femtosecond ablation and studied the deposits using atomic force microscopy. It was found that there was little change in the nanoparticle mean size, no matter what ablation conditions were used. It is therefore of interest to develop or study techniques that can induce a change in the ablation products.

The study of femtosecond laser ablation using a pair of collinear pulses with controlled separation is receiving increasing attention due to the interesting effects which arise both in the properties of the laser produced plasma, in the morphological features of the ablation craters and the possibility to modify the ablation products. Double pulse (DP) irradiation has been also used in experiments aiming to elucidate the ablation mechanisms involved in fs laser ablation. Most of these studies deal with ablation of a silicon (Si) target, while DP ablation of metals has been less investigated. Different features of the ULA process, such as ion yield, plasma emission intensity or ablation depth, can be used to investigate how DP irradiation affects the plasma plume and the efficiency of the ablation process. Depending on the time delay between the pulses, the second pulse may interact with a modified target surface or with the ablated material produced by the first pulse. Since different physical processes, such as electron-lattice relaxation and hydrodynamic

expansion, occur on different time scales, the time delay between the pulses can influence the final properties of the ULA products.

Several experimental studies of DP ULA of Si have been carried out. For example, Spyridaki *et al.* used time of flight mass spectrometry to study the increase in the number of ions measured for two pulse ablation of Si [14]. They also noted that DP ablation yields a much smoother ablation crater. This was attributed to efficient energy coupling of the second pulse to the melted layer produced by the first acting to prevent the ripple formation which occurred for single pulse ablation. Using emission spectroscopy, Hu *et al.* observed that a second delayed pulse causes an increase of the ion emission from Si [15]. Again it was suggested that this increase was due to enhanced absorption of the second pulse at the molten surface produced by the first. Scuderi *et al.* studied DP ablation of titanium and looked at the effect of delay on the nanoparticle production by making time resolved measurements of nanoparticle plume emission [16]. They observed a considerable drop in this emission signal at delays ≈ 1 ns which was attributed to interaction of the second pulse with the nanoparticulate matter leaving the target after the plasma component has expanded sufficiently to be optically thin to the second pulse. Semerok and Dutouquet studied DP ablation for short delays and for a range of laser pulse durations [17]. They found that the ablation depth was effectively doubled with the addition of a second delayed pulse for delays <1 ps. For longer delays, the ablation depth decreased, until at 100 ps the depth was comparable to, if not slightly smaller than, that observed for single pulse (SP). In the range $0.1 - 2$ ps, this behaviour did not depend on the laser pulse duration, nor did the ablation efficiency. Plasma shielding was suggested as the cause. Noel and Hermann measured the spatially resolved atomic/ionic and nanoparticle emission from a DP ablation plume as a function of delay [18]. With increasing delay, beyond the electron-lattice thermalisation time, the plasma emission species increases while the nanoparticle emission decreases. Recently Amoruso *et al.* studied the role of laser polarization during DP

130

ablation of aluminium and copper and found that more efficient ion generation occurs for p polarization [19], which was attributed to resonance absorption of the second pulse in the material ablated by the first. These various studies have enabled some understanding of DP laser ablation, though most of the experiments examine one specific feature of the DP process, such as ablated depth or ablation plume dynamics. It seems that a study that examines the behaviour of several features may be useful.

In this section we describe the results of a study of DP ablation of a Ni target where both the ablation plume characteristics (ion flux and angular distribution) and target ablation depth have been measured. For a fixed value of fluence, the effect of varying the delay between pulses has on the ablation process was studied. The experimental setup used is the same as the previous section but a Michelson interferometer is inserted into the beam path to produce a pair of identical laser pulses separated by a delay, Δt which can be varied from ≈ 1 picosecond to about a nanosecond. The presence of the Michelson interferometer affected the laser pulse profile so that final beam intensity profile was no longer Gaussian, which was evident from the ablation crater profiles. The average laser fluence was calculated using Eq. 5.4. The maximum energy of each pulse in the modified setup was $\approx$ 85 μJ and the ablation spot area was $\approx 6 \times 10^{-4}$ cm^2, found from imaging the ablated craters using an optical microscope. For DP ablation the average fluence for each pulse in the pulse pair is 0.14 J cm^{-2}. This value corresponds to a little less than one quarter of the maximum SP fluence attainable. To compare against DP ablation, measurements were also made using single pulses where one of the beam path lengths in the Michelson interferometer was blocked. Figure 5.18 shows an optical microscope image of the ablation crater formed with a delay of 1 ps. The area was found by measuring the minor and major crater diameters as a function of delay and finding an average value. The crater dimensions did not depend strongly on the delay between pulses.
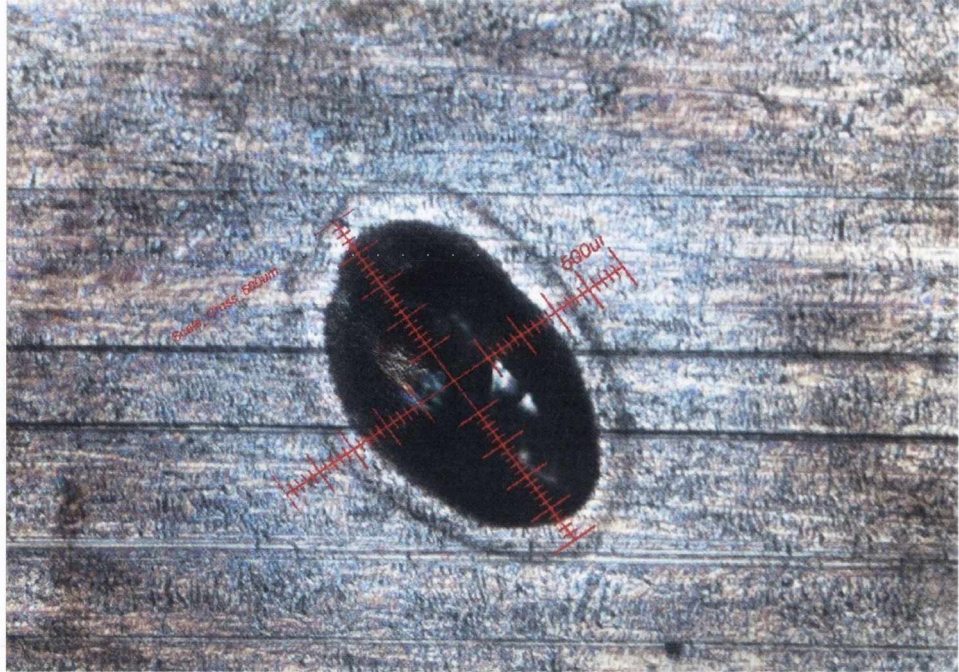
Figure 5.18 Optical microscope image of the ablation crater formed from DP ablation with a delay of 1 ps and using 2970 shots.

A maximum fluence value of 0.14 J cm^{-2} was obtained for each individual pulse in the pulse pair. As with the SP experiment, a Langmuir probe was used to characterise the plasma part of the ablation plume. The ablation depth per pulse was found by using white light interferometry to measure the depth of ablation craters formed during ablation for a fixed number of pulses.

5.3.1 Ablation depth measurements

Figure 5.19 shows the depth distributions, as measured using the white light interferometer for a few different values of delay. Fig. 5.19 also shows the depth profile along the major radius of the elliptical crater. The white data points in the surface profile maps are points on the target surface which were not measured due to non reflection of the probe beam.
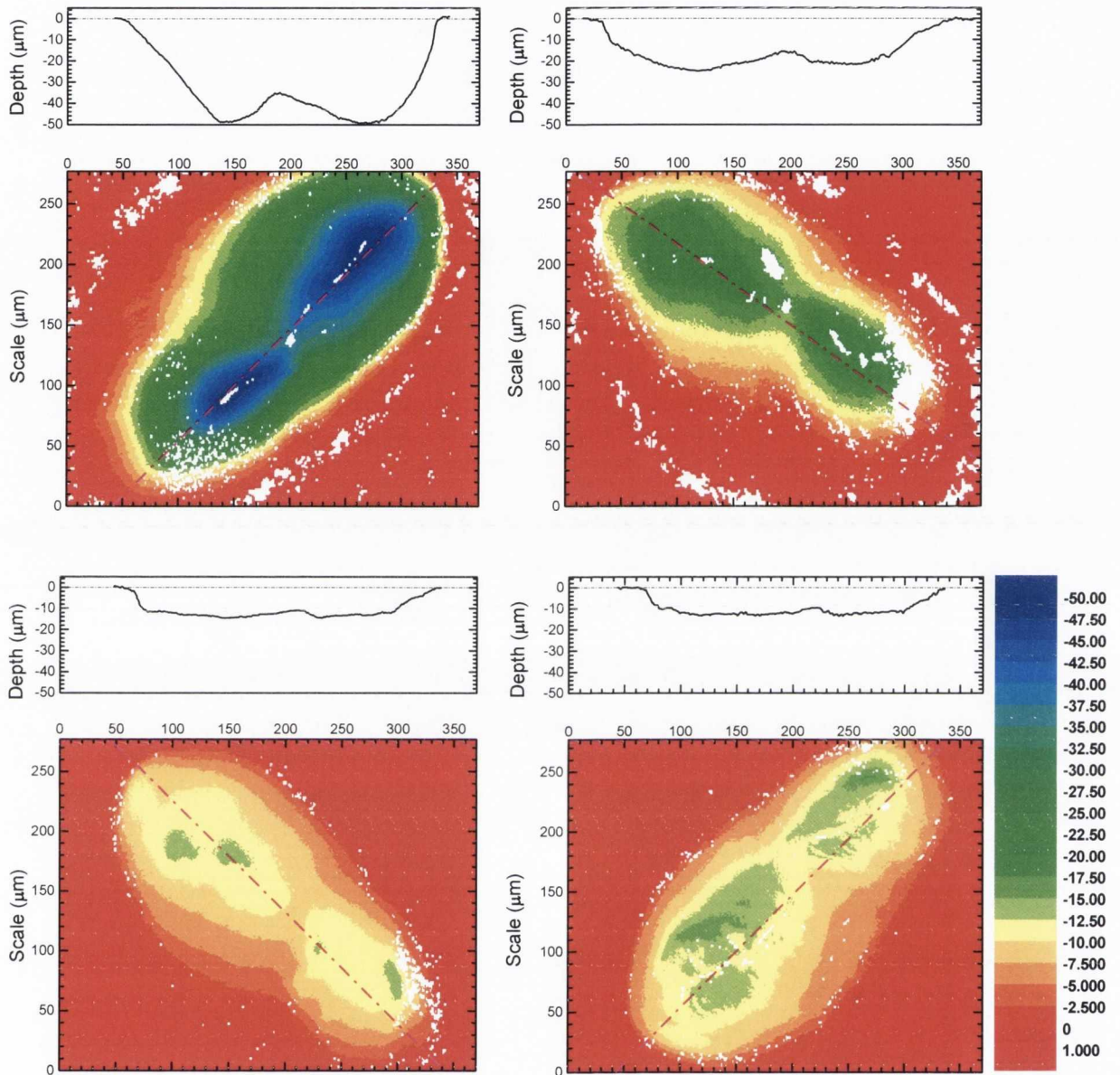
Figure 5.19 Surface profiles of the ablation craters formed from DP ablation with a pulse delay of (a) 5 ps (b) 20 ps (c) 100 ps (d) 500 ps.

Crater depth profiles were measured for a range of delays and these are shown in Fig. 5.20. The depth profile for a SP irradiation is shown in the first panel. In the second and third panel the DP profiles are shown for increasing delay. The second panel show the profiles for small delays where an increase in the depth is observed. The third panel shows profiles

for large values of delay where the depth becomes smaller than the SP value. It can also be seen the depth profiles are significantly smoother for larger delays.
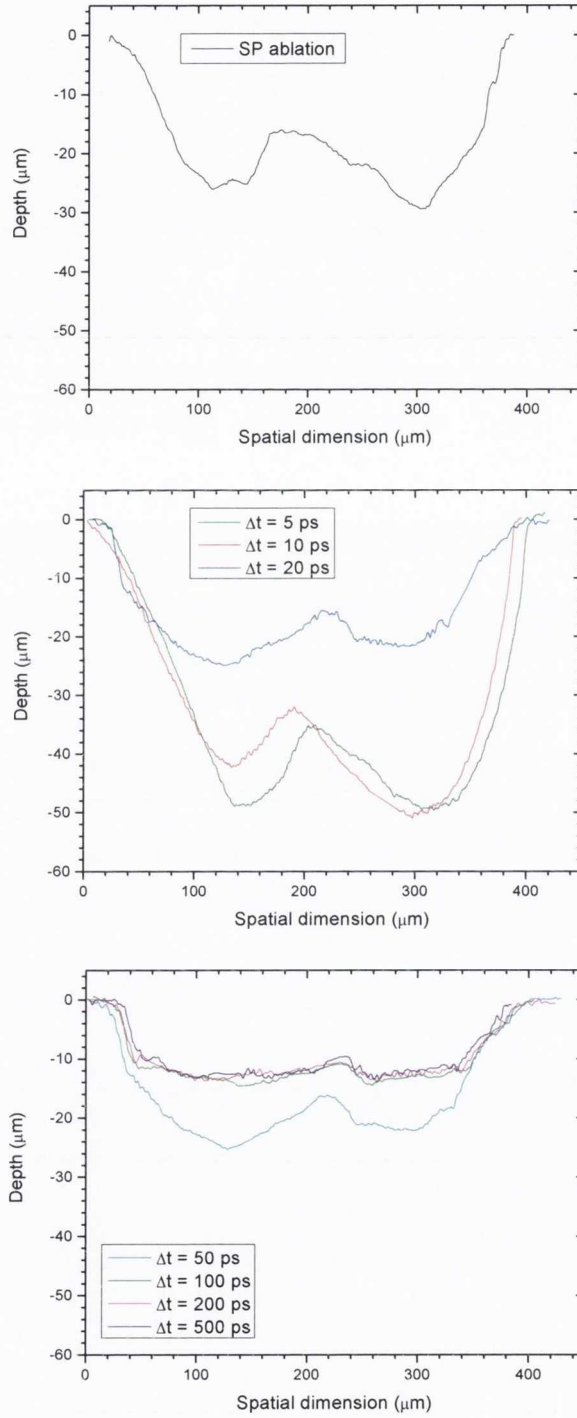
Figure 5.20 Depth profiles, taken along the major axis of the ablation craters, as a function of delay between pulses.

Using the data obtained from the surface profile measurements the total ablated volume and maximum ablated depth could be found for a given pulse delay Δt. This data is presented in Fig. 5.21. From Fig. 5.19 – 5.21 it is obvious that there is a clear dependence of the amount of ablated material on Δt.
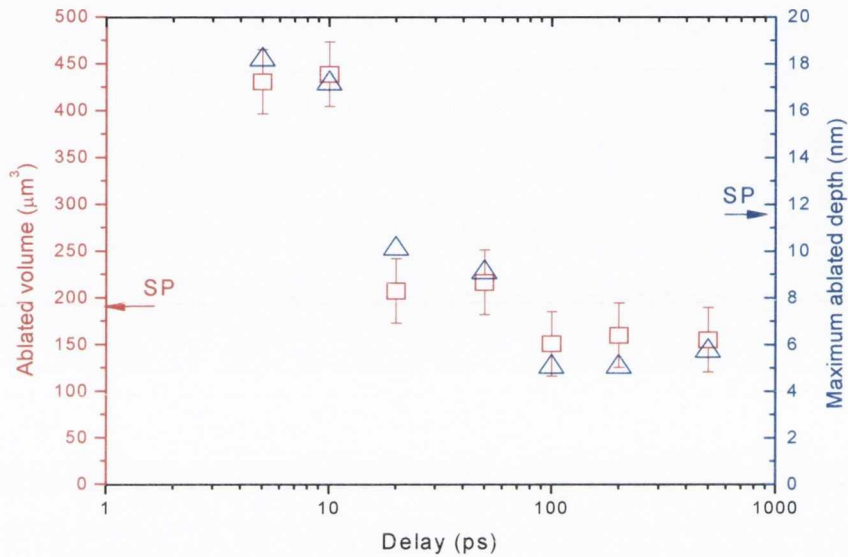
Figure 5.21 Ablated volume and maximum ablated depth as a function of delay.

For short delays, the ablation volume and depth are more than twice the SP values. As Δt is increased beyond ≈ 10 ps the volume and depth are progressively reduced, falling somewhat less than the SP value for $\Delta t \geq 100$ ps. The electron phonon time is about 5 ps which is close to the delay value where there is a distinct drop in the amount of ablated material. As shown in Fig. 5.20, this reduction in ablated volume is coincident with a dramatic change in the shape of the ablation crater: from a shape which reflects the beam intensity profile at short delay to a shallower flat-bottomed crater at long delays. Thus, it seems that the action of the second pulse is to preferentially suppress ablation in the higher fluence regions of the beam spot.

5.3.2 Langmuir probe measurements of plasma expansion

The influence of a second delayed pulse on the expansion dynamics of the ionized ablated material was investigated using the Langmuir probe to record the ion TOF signals at different angles, θ, away from the target normal and for different delays of the second pulse. Fig. 5.22 shows the ion signals along the target normal ($\theta = 0°$) for different delays and a signal for SP ablation is also shown for comparison.
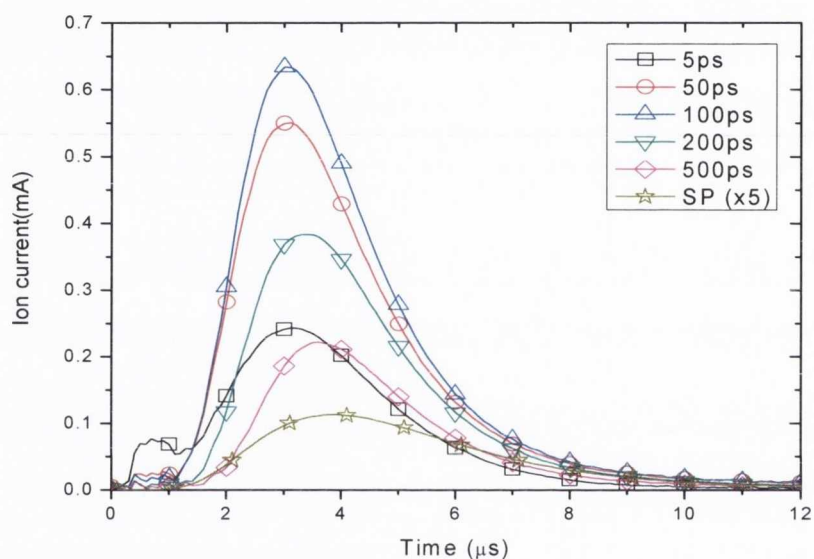

Figure 5.22 Ion signals for a range of delays. A SP ion signal (x5) is shown for comparison.

For all values of delay, the addition of the second pulse leads to a large increase of the amplitude of the ion signal. Both the amplitude and, to a lesser extent, the TOF at the peak are dependent on the delay. The average ion energy was calculated from the TOF signals. For SP the average energy is 22.5 eV. For DP at small delays the average energy rises to 35 eV. The average energy decreases as the delay is increased, such that at $\Delta t = 500$ ps it is about equal to the SP value, even though the amplitude of the ion signal is still several times larger than for SP ablation. The ion energy distribution and the average energy as a function of delay are shown in Fig. 5.23
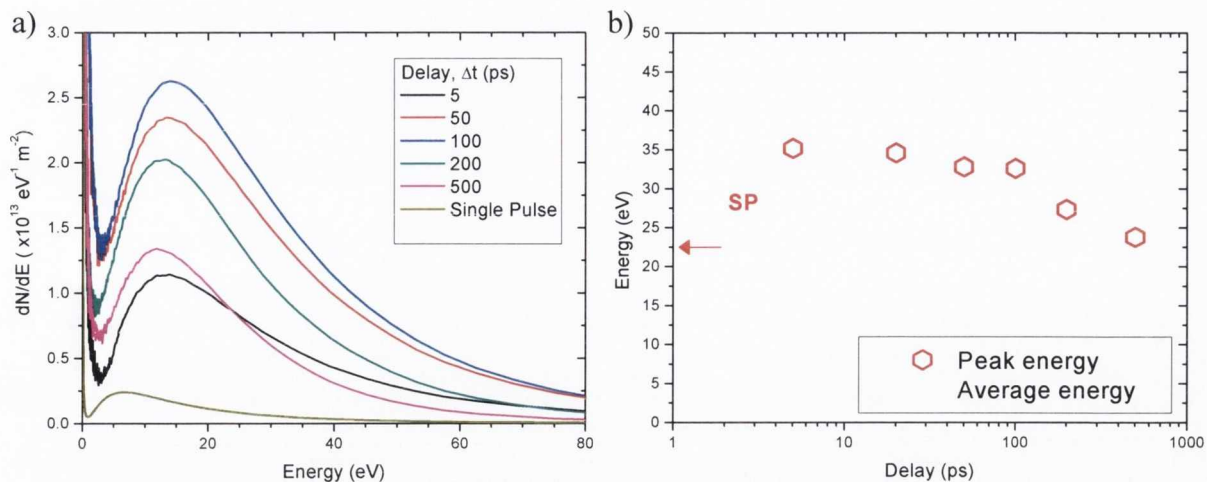
Figure 5.23 Ion energy distributions as a function of delay (a) and corresponding average energy (b).

The ion signals in Fig. 5.22 were integrated to see how the ion yield in the normal direction depends on delay. This is plotted in Fig. 5.24 which includes additional data points corresponding to signals not shown in Fig. 5.22. The arrow indicates the ion yield for SP.
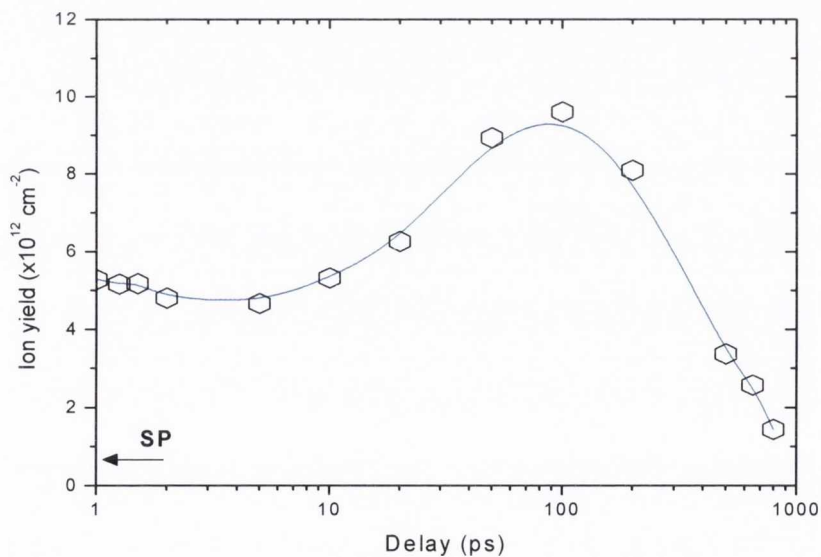

Figure 5.24 Ion yield, normal to the target, measured by the probe for a range of delay. The blue line is a guide for the eye.

At short delays (1 ps < Δt < 10 ps) the DP ion yield is almost constant, it starts to increase at ≈10 ps, reaches a maximum at ≈100 ps, and then falls at longer delays, eventually to below the short delay case for delays >300 ps. This behaviour is very similar to that

previously reported for DP ablation of copper and aluminium [19]. Looking at the ablation depth (Fig. 5.21) and ion yield data (Fig. 5.24) together, it can be seen that the range of delay (10 ps < Δt < 100 ps) over which the ablation depth is reduced is closely correlated to the enhanced ion yield.

To see if the second pulse has any influence on the shape of the ion plume, the angular distribution of the ion yield for a range of delays was measured. For example, Fig. 6(a) shows the angular distributions of ion yield for SP and for DP at Δt =50 ps.
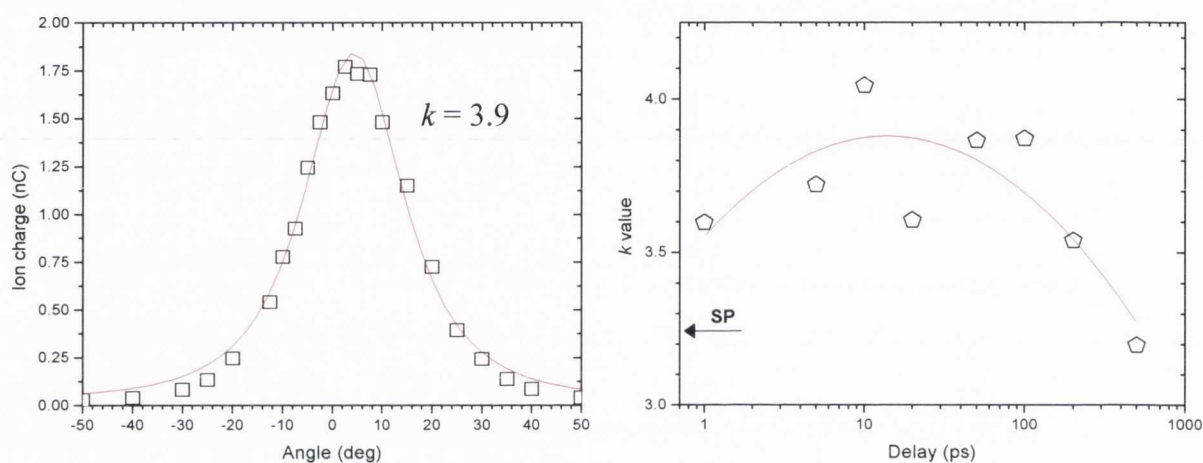

Figure 5.25 (a) Angular distribution of ion charge measured by the probe for delay of 50 ps. (b) Variation of plume aspect ratio with delay. The corresponding SP value is provided by the arrow and the red line is a guide for the eye.

For clarity the distributions have been normalized to the same maximum value. In both cases the distributions are strongly peaked in forward direction (θ=0^0), and the DP distribution is somewhat narrower. The distributions have been fitted using Eq. 2.21. From Fig. 5.25 (a), it can be seen that this expression provides a good description of the shape of the LPP expansion for both SP and DP irradiation. The variation of k with Δt for DP irradiation is plotted in Fig. 6(b); the SP value is also shown. For DP irradiation at short delays, k is higher than for SP. It increases further as the delay is extended to ≈10 ps, and finally falls back to the SP value at ≈500 ps.

138

5.3.3 Interpretation of results

Our experimental observations point to a rather complex interplay between the different mechanisms involved in DP fs ablation as well as their influence on the overall relaxation dynamics of the excited target material and the final ablation depth. The nature of the optical interaction of the second pulse will depend on how the near-surface region of the target has evolved since the delivery of the first pulse, and thus on the delay, Δt, between the pulses. The discussion in the previous section has outlined how modelling and experiments show that ULA is characterized by complex decomposition mechanisms and that mixture of vapour and clusters is produced by ablation process. While a clear picture of fs ablation is emerging for the case of single pulse ablation, modelling of DP ablation has not been done. However, it is possible to discuss our observations within the framework of current knowledge of fs ablation.

For Ni the characteristic time of electron-lattice energy transfer is ≈ 5 ps [6], therefore, for delays less than this time, the second pulse interacts with an electron distribution which is not in equilibrium with the lattice. This can explain the observed constancy of the ion yield and ablation depth for $\Delta t < 10$ ps. Moreover, while the DP ion yield increases almost 7-fold with respect to SP value, for $\Delta t < 10$ ps, the ablation depth is only doubled. For $\Delta t > 10$ ps, the second pulse interacts with the cloud of atomic particles which finally forms the atomic plume at longer distance and time. This material expands at a velocity $u \approx$ few $\times 10^5$ cm/s [6]. The average density of this atomic vapour, resulting from ablation of an initial surface layer of thickness $d_0 \approx 2$-3 nm, can be estimated as $n \approx (n_s d_0)/(u \Delta t)$, $n_s = 9.1 \times 10^{22}$ cm^{-3} being the solid Ni atomic number density. At delays of 10 - 100 ps, the second pulse strongly interacts with the atomic vapour, characterized by a density $n \approx (0.5$-5$) \times 10^{21}$ cm^{-3} and a temperature $T \approx (0.5$-1$)T_c$, where $T_c = (9470 \pm 40)$ K is the critical temperature of Ni [6, 11]. Under these conditions the high density, partially ionized atomic vapour can significantly absorb the second pulse through bound-bound and bound-

free transitions as well as inverse bremstrahlung. At high density, the bound-bound transitions will be strongly Stark broadened, and will overlap to yield quasi-continuous absorption which can be much stronger than other mechanisms. This point is often overlooked in dealing with the emission and absorption properties of low temperature LPP as described in chapter 2. We have calculated the total absorption cross-section using the spectral synthesis code PrismSPECT, which models the plasma ionization, level populations, line broadening and spectral emission and absorption for a given temperature and density. The code is described in chapter 3. For example, for Ni with an atom density of 1×10^{21} cm^{-3}, and a temperature of 0.8 eV, which is close to the critical temperature, the optical absorption cross section at 527 nm (2.35 eV) is calculated to be 2.3×10^{-18} cm^2. The absorption spectrum of Ni is presented in Fig. 5.26. At these conditions the fraction of singly-ionised Ni is only 2%. The average fluence in each beam is 0.14 J cm^{-2}, which corresponds to 3.7×10^{17} photons cm^{-2}. The probability that each atom absorbs a photon from the second beam is ≈ 0.9, which corresponds to ≈ 2 eV per atom. This will produce a temperature rise of about 0.5 eV, which according to PrismSPECT, will raise the fraction of Ni$^+$ to $\approx 20\%$, thus explaining the dramatic increase in ion yield caused by the second delayed laser pulse.
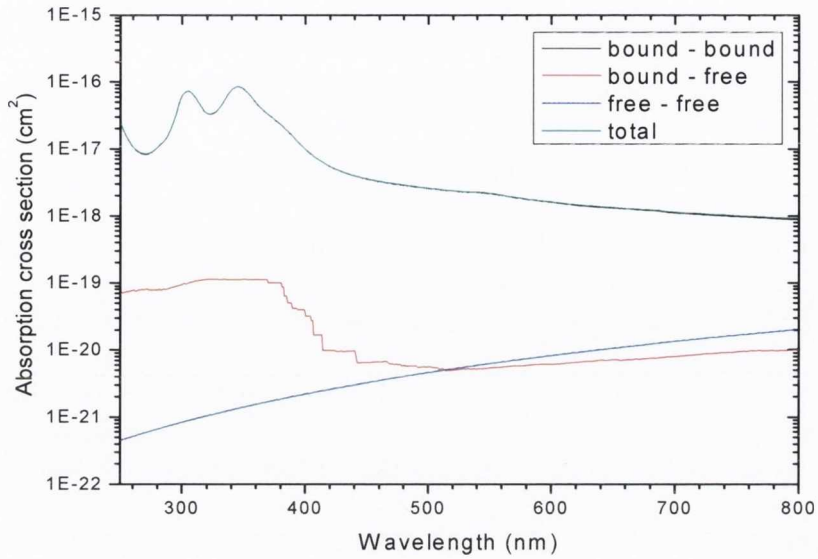
Figure 5.26 Wavelength dependent absorption cross-sections calculated for Ni plasma of density 1×10^{21} cm^{-2} and temperature 0.8 eV. The total cross section and contribution from bound-bound, bound-free and free- free are shown.

As the delay increases beyond a value around 100 ps, both the density and temperature of the atomic vapour component produced by the first pulse will decrease, the absorption cross-section at the laser wavelength will decline rapidly, and the atomic vapour layer will become almost transparent to the second laser pulse. This is reflected in the ion yield measurements where for delays longer than 100 ps the yield starts falling rapidly.

It is now clear that the delay dependence of the ablation depth in Fig. 5.21 is strongly correlated to the shielding effect of the atomic vapour produced by the first pulse. In the regime where the ionization of atomic vapour is enhanced (≈ 10 - 100 ps) and the second laser pulse is efficiently absorbed, the ablation depth falls significantly. However, at long delays ($\Delta t >100$ ps), although the absorption of the nascent atomic vapour is gradually reduced, the second pulse can still be absorbed and scattered at the front of the following vapour/cluster layer, and the ablation depth remains low, indeed at a value below the SP case.

141

These findings seem to indicate that heating of either the nascent atomic vapour, or the deeper mixed vapour/cluster layer, modifies the successive relaxation dynamics of the irradiated material, finally reducing the ablation efficiency and, consequently, the ablation depth. While this feature requires further investigation, it seems that our observation may be similar to the reduction of the ablation efficiency recently reported for low-fluence ULA of a target wetted by a thin liquid film which was studied using molecular-dynamics simulations [20]. Therein it is shown that when the thin liquid film is suddenly heated to high temperature, it relaxes along a supercritical trajectory to form a hot fluid layer above the surface of the heated target. The presence of such a high-pressure fluid layer significantly modifies the subsequent ablation dynamics such that deeper sections of heated target tend to relax back toward their initial solid state. This reduces the efficiency of material ejection and, in turn, the ablation yield. Thus it seems that in DP fs ablation when the second pulse is delayed by more than ≈ 10 ps, the rise in pressure caused by interaction of the second pulse with the nascent plume acts as a tamper which impedes the decomposition of material deeper in the target and lowers the ablation depth. As a result it seems that using double pulses with a separation of more than ≈ 100 ps may be a way of obtaining more uniform ablation craters.

Finally, the observed change of the shape of the ion plume can be explained in the context of interaction of the second pulse in the nascent plume. The higher k value observed for DP with short delay, as compared to SP, may be due to the formation of plasma over somewhat larger area when the net fluence is higher. For delays up to ≈ 100 ps efficient laser absorption of the second pulse in the nascent atomic vapour will lead to a larger area of plasma formation than for SP. For long delays we expect a gradual reduction of the absorption of the second laser pulse in the atomic vapour and k should progressively return to the SP value, which it does.

142

5.4 References

[1] J. Bonse, J.M. Wrobel, J. Krüger and W. Kautek, *Appl. Phys. A*, **72**, 89–94 (2001)

[2] Y. Jee, M.F. Becker and R.M.Walser, *J. Opt. Soc. Am. B*, **5** 648 (1988)

[3] X. Ni, C. Wang, L. Yang, J. Li, L. Chai, W. Jia, R. Zhang and Z. Zhang, *Appl. Surf. Sci.* **253** 1616–1619 (2006)

[4] S. Nolte, C. Momma, H. Jacobs, A Tunnermann, B. N. Chichkov, B. Wellegehausen and H. Welling, *J. Opt. Soc. Am. B*, **14**, 10 (1997)

[5] K. Vestentoft and P. Balling, *Appl. Phys. A*, **54**, 207-213 (2006)

[6] S. Amoruso, R. Bruzzese, X. Wang, N. N. Nedialkov and P. A. Atanasov, *J. Phys. D: Appl. Phys.*, **40**, 331-340 (2007)

[7] A. Caruso and R. Gratton, *Plasma Phys.*, **11**, 10, 839 (1969)

[8] B. Toftmann, B. Doggett, J. Schou and J. G. Lunney, *in preperation*

[9] B. Doggett and J. G. Lunney, *J. Appl. Phys.*, **105**, 033306 (2009)

[10] S. Canulescu, E. L. Papadopoulou, D. Anglos, T. Lippert, C. W. Schneider and A. Wokaun, *J. Appl. Phys.* **105**, 6, 063107 (2009)

[11] C. Cheng and X. Xu, *Phys. Rev. B*, **72**, 165415 (2005)

[12] M.E. Povarnitsyn, K.V. Khishchenko, P.R. Levashov, J. Hermann, S. Noel and T.E. Itina, Oral presentation titled *"Simulation of ultrashort double pulse laser ablation of metals"*, EMRS Spring meeting (2009)

[13] S. Amoruso, G. Ausanio, A. C. Barone, R. Bruzzese, L. Gragnaniello,
M. Vitiello and X. Wang, *J. Phys. B: At. Mol. Opt. Phys.*, **38**, L329–L338 (2005)

[14] M. Spiridaki, E. Koudoumas, P. Tzanetis, C. Fotakis, R. Stoian, A Rosenfeld, and I.V. Hertel, Appl. Phys. Lett. **83**, 1474 (2003).

[15] Z. Hu, S. Singha, Yaoming Liu and R.J. Gordon, Appl. Phys. Lett. **90**, 131910 (2007).

[16] D. Scuderi, O. Albert, D. Moreau, P.P. Pronko, and J. Etchepare, Appl. Phys. Lett. **86**, 071502 (2005).

[17] A. Semerok and C. Dotouquet, *Thin Solid Films*, **453-454**, 501 (2004).

[18] S. Noel and J. Hermann, *Appl. Phys. Lett.*, **94**, 053120 (2009).

[19] S. Amoruso, R. Bruzzese, X. Wang, and J. Xia, *Appl. Phys. Lett.*, **93**, 191504 (2008).

[20] D. Perez, L. K. Béland, D. Deryng, L. J. Lewis, and M. Meunier, Phys. Rev. B **77**, 014108 (2008).

Chapter 6: Nanostructured metal film synthesis by pulsed laser ablation

In this section we report the results of a systematic investigation of PLD in vacuum of nanostructured films of Ag. We have sought to correlate the optical absorption properties of the films with transmission electron microscopy (TEM) images of the film morphology. In particular, we have explored how the morphology and optical properties vary with equivalent thickness (areal density divided by solid density), which is controlled by the laser shot number and a quartz crystal monitor

6.1 Pulsed laser deposition of nanostructured silver films

There is currently much interest in the preparation and characterisation of nanostructured metal films with feature sizes in the range 1-100 nm. This interest is due to the many novel properties (optical, magnetic and catalytic) which arise when the dimensions of a solid material are reduced to the point where the particle contains from a few to thousands of atoms [1, 2]. Many of the techniques used for thin film deposition, such as thermal evaporation, sputtering, ion implantation, chemical vapour deposition and pulsed laser deposition (PLD), can be adapted for the preparation of nanostructured thin films. In particular, it has been shown that PLD is a relatively simple and effective nano - fabrication technique.

Previously, Afonso et al [3, 4] used PLD with a nanosecond laser, both in vacuum and a gaseous atmosphere, to prepare nanocomposite films of copper in amorphous alumina. By examining the areal density dependence of the morphology, they concluded that nucleation and growth of the metal nanoparticles is dominated by processes occurring on the substrate rather than in the gas phase. Similarly, Dolbec et al [5] used a nanosecond laser to investigate PLD of platinum nanoparticles on pyrolitic graphite. They showed that there is a power law dependence of the particle diameter on nominal thickness and that the shape of the nanoparticles depends on the energy of the ablated species. Femtosecond laser pulses have also been used for PLD of nanoparticles where various studies have observed nanoparticles in the ablation plume [6]. The physical mechanisms for this have been discussed in chapter 2. Thus, it would seem that for production of nanoparticles in vacuum, femtosecond ablation can lead to nanoparticle formation in the ablation plume but nanosecond ablation does not. The lack of nanoparticles in nanosecond ablation plume seems to be primarily due to laser absorption and heating of the ablated material much of which is mainly evaporated during the laser pulse. However, it is possible to promote

nanoparticle formation in nanosecond ablation plumes if a background gas is used to confine the expansion of the plume, allowing sufficient time for nucleation [7].

The main feature in the visible/UV optical response of a nanoparticle metal film is an absorption feature due to the surface plasmon resonance (SPR) which is a collective oscillation of free electrons confined to the metal particle. The wavelength and strength of the SPR depends on the bulk dielectric properties of both the nanoparticle and host materials as described in chapter 2. The theoretical description of the optical response of nanostructured metals can be traced back for about 100 years to the work of Mie and Maxwell Garnett. Mie theory considers the interaction of an electromagnetic wave with a homogeneous spherical particle placed in host material where the response to the field of both the particle and the host can be described using bulk dielectric functions (see chapter 2). The theory can be extended to nonspherical particles. Effective medium theories, such as that of Maxwell Garnett and Bruggeman, offer a simpler method for the computation of the optical properties of nanostructured metal films.

The nanostructured films were prepared using a KrF excimer laser (248 nm, 26 ns, 10 Hz) to ablate a rotating Ag target in a vacuum chamber at a pressure of 4×10^{-5} mbar (4 mPa). Part of the laser beam was imaged onto the target, at an incident angle of 45°, to give a spot of 0.22×0.06 cm^2 and an average fluence of 1 J cm^{-2}. Films were deposited on polymer and glass substrates placed 9.5 cm directly in front of the target. The polymer substrates were 150 nm thick Formvar films on Cu TEM support grids. A planar Langmuir ion probe of area 0.18 cm^2, biased at -32 V, was placed beside the substrate facing the target to measure the flux and energy distribution of the ion flow in the ablation plume. In addition, the ion probe also ensured reproducibility of plasma parameters. A quartz crystal monitor was used to measure the equivalent thickness of the deposited material. The number of laser shots per deposition was varied between 1,000 and 10,000 to change the equivalent thickness. The morphology of the deposits on the polymer films was examined

by TEM. Optical transmission spectra of films on polymer and glass were measured with a dual beam UV-vis spectrophotometer and an uncoated substrate was placed in the reference arm of the spectrophotometer.

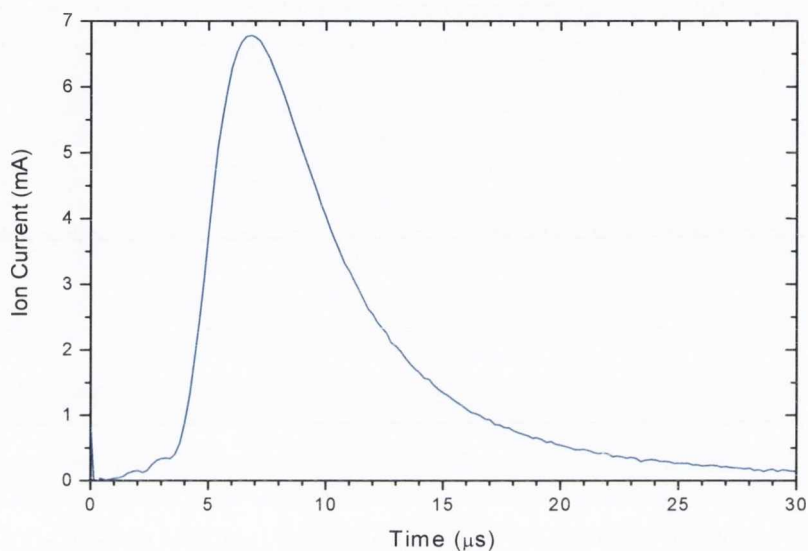The pulse of ion current measured by the negatively biased Langmuir probe during deposition is shown in Fig. 6.1.

Figure 6.1 Ion time of flight signal recorded using a planar ion probe that was biased at -32 V and placed beside the substrate.

To good approximation the ion velocity v is given by the probe-target distance d divided by the time-of-flight t. The peak of the ion signal (7.28 μs) corresponds to ion energy of 95 eV. The complete ion energy distribution function, dN/dE, is obtained from the ion current using Eq. 3.7. The energy distribution is shown in Fig. 6.2.

147
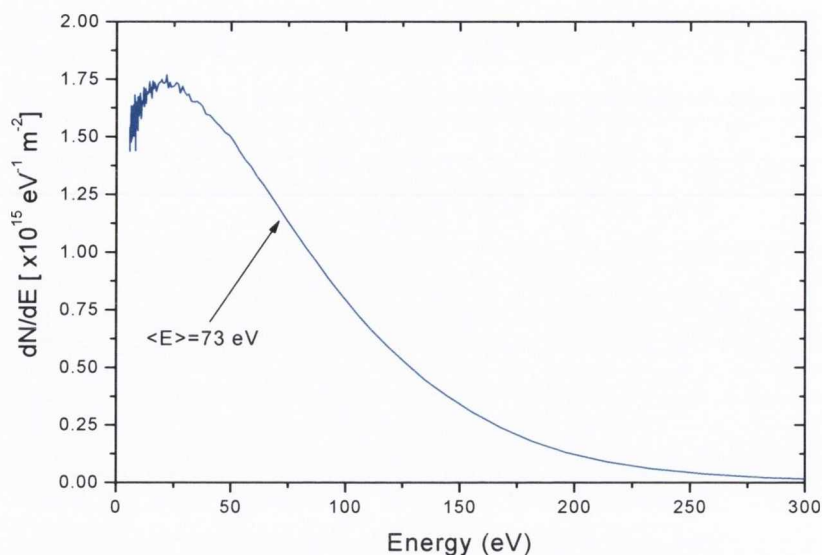
Figure 6.2 Ion energy distribution at the substrate position.

The average energy, found using Eq. 3.8, is 73 eV. Thus it can be seen that the deposition plasma is sufficiently energetic to cause significant self-sputtering of the growing film [8]. The deposition per laser shot measured on the quartz crystal monitor was 6×10^{-4} nm (or 3×10^{12} atoms cm^{-2}). Integrating the ion signal gives an ion dose of 2.3×10^{12} ions cm^{-2} per shot.

Fig. 6.3 shows TEM images of silver films deposited on Formvar with 1,000, 3,000 and 10,000 laser shots where the equivalent thicknesses are 0.53 nm, 1.37 nm and 4.4 nm respectively. The 0.53 nm and 1.37 nm films show well-separated particles that have diameters less than 7 nm. In the 4.4 nm film it can be seen that some of the particles have coalesced to form oblong structures.
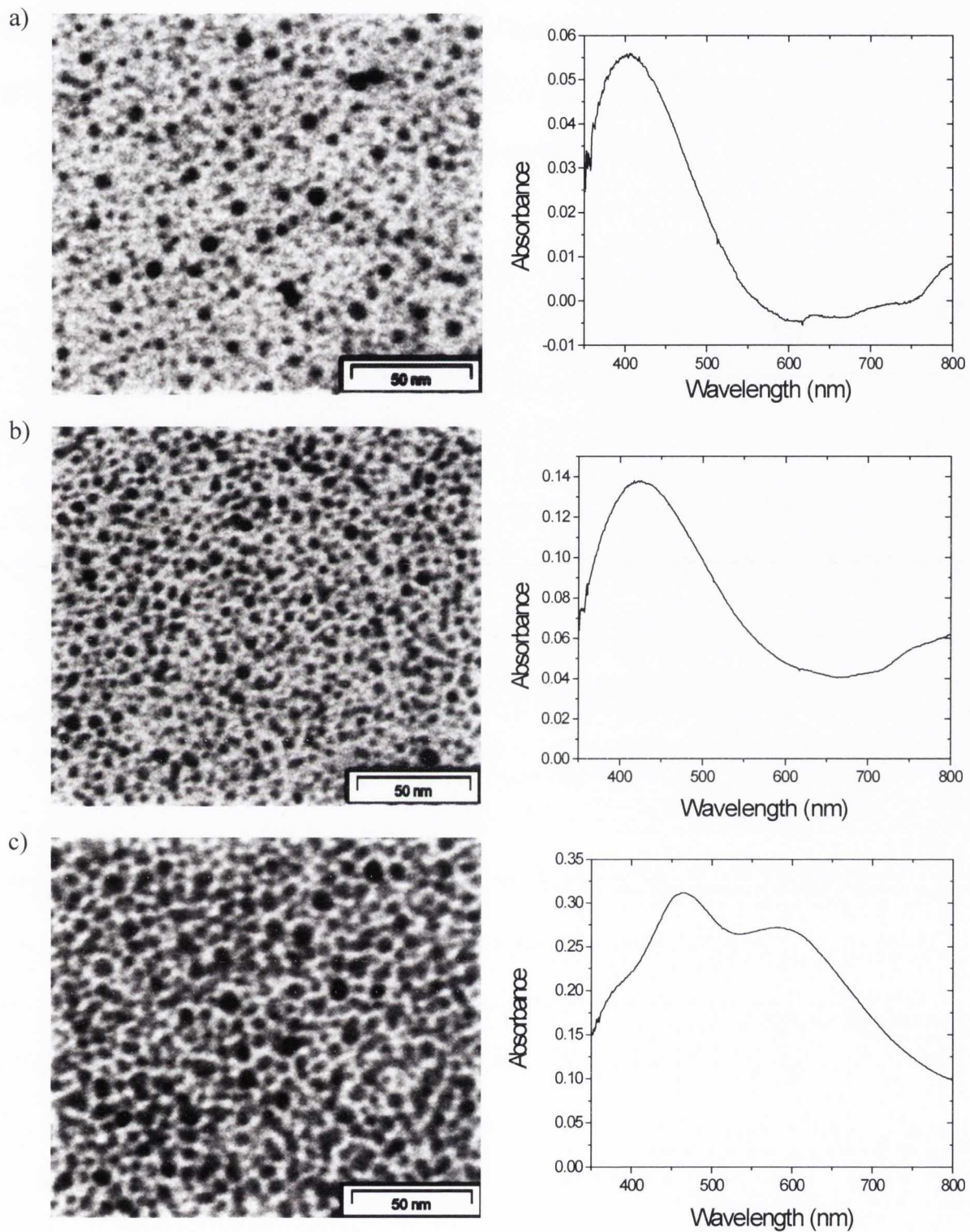
Figure 6.3 TEM images of nanostructured Ag films on Formvar for different equivalent thicknesses: (a) 0.53 nm (b) 1.37 nm (c) 4.4 nm. The dark regions correspond to Ag. Also shown are the corresponding absorbance spectra.

Figure 6.3 also shows the absorbance spectra of these films; the absorption feature due to the SPR is clearly observed. Figure 6.4 shows the absorbance spectra of films prepared under the same conditions but on glass instead of Formvar.
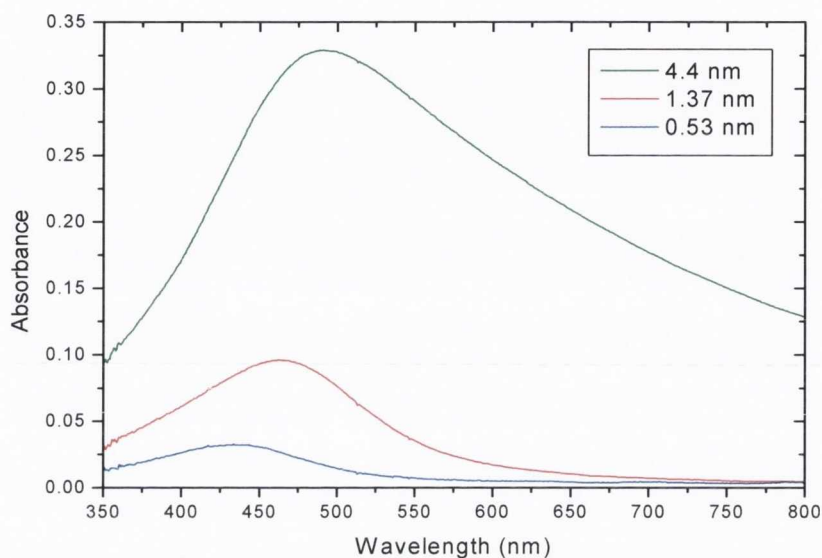

Figure 6.4 Absorbance spectra of silver films on glass for various equivalent thickness.

Again, the SPR is clearly observed and the magnitude of the peak absorption is similar to the value for deposition on Formvar, though there are some differences in the detailed structure of the two sets of absorption spectra, perhaps arising from some difference in the nature of surface diffusion on glass and Formvar. In particular, it can be seen that the 4.4 nm film on Formvar shows two peaks at 465 nm and 580 nm, while only a single peak at 490 nm is observed for the deposition on glass. The second peak at 580 nm for the films on Formvar, is probably due to the appearance of the oblong structures which show different resonant frequencies associated with the *E*-field along short and long dimensions [9].

For both Formvar and glass substrates the wavelength and absorbance of the SPR increases as the equivalent film thickness is increased. The values of peak absorbance are

nearly the same for the two substrates. However, the peak wavelength of the SPR is slightly higher for films on glass as compared to Formvar.

It is useful to explore to what extent it is possible to obtain a quantitative theoretical description of the absorption spectra of nanostructured metal films. Of the variety of theoretical methods which are described in chapter 2 we have chosen to use the effective medium theory of Maxwell-Garnett [10]. This formalism is more appropriate than the Bruggeman formalism when the volume fraction of one component is significantly less than the other. The Maxwell-Garnett expression for the average dielectric function, ε_{eff}, of a composite medium was given in Eq. 2.27. The factor 2 in Eq. 2.27 is appropriate for spherical particles. The effective dielectric function was used to find the effective refractive index of the composite medium and the absorbance was calculated using the expression for the optical transmission of a thin absorbing film on a transparent substrate, Eq. 2.27.

Figure 6.5 shows a Maxwell Garnett calculation of the absorbance spectra for a film of spherical Ag particles in air where the equivalent thickness of fully dense Ag is 1.37 nm and the volume fraction is changed from 0.1 to 0.3. The host dielectric constant ε_m was taken to be 1.625, the averaged value of the dielectric constants of glass and air. This was done in accordance with Xu *et al.* [11], to account for the fact that both glass and air constitute the host medium of the nanoparticles. The refractive index of the substrate was taken to be 1.5, and for comparison with the measurement the calculated transmission was divided by 0.96 to take account of the reflection loss at the rear surface of the substrate. The wavelength of maximum absorption moves to longer wavelength as the volume fraction is increased; a value of around $f = 0.2$ gives the same resonant wavelength as the 1.37 nm Ag film on polymer (Fig. 6.3 (b)).
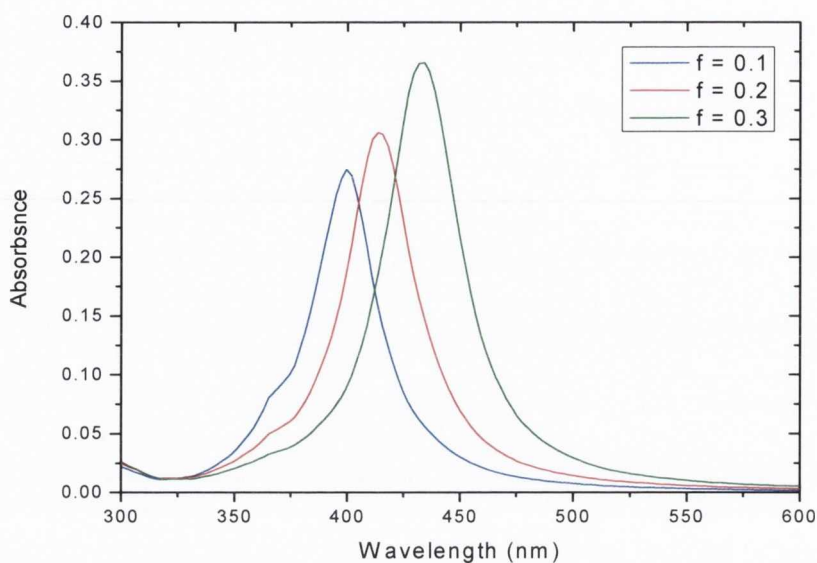
Figure 6.5 Calculated absorbance of a 1.37 nm equivalent thickness Ag film on Formvar for different volume fractions.

The width of the calculated resonance is less than the measured value, which may due to variation of the Ag volume fraction through the depth of the nanoparticle film; near the substrate all particle sizes will contribute to the volume fraction while close to the top only the largest particles will do so. It should be noted that as f approaches a value of 0.5 the limit of applicability of the Maxwell-Garnett theory is being reached, and the Bruggeman formalism may be more appropriate, particularly for films showing sign of coalescence.

6.2 Nanoparticle synthesis during confined laser ablation

During pulsed laser deposition the ion density $\sim 10^{10} - 10^{12}$ cm^{-3} and the plasma temperature can be between 0.1 and 0.5 eV depending on the substrate distance. This is significantly less than the initial density and temperature when the plasma is close to the ablation target, as we have seen in chapter 4. Figure 6.6 shows the ion density profile calculated from the ion TOF shown in Fig. 4.5 recorded at 9 cm for 1064 nm ablation of Ag at 1.5 J cm^{-2}.
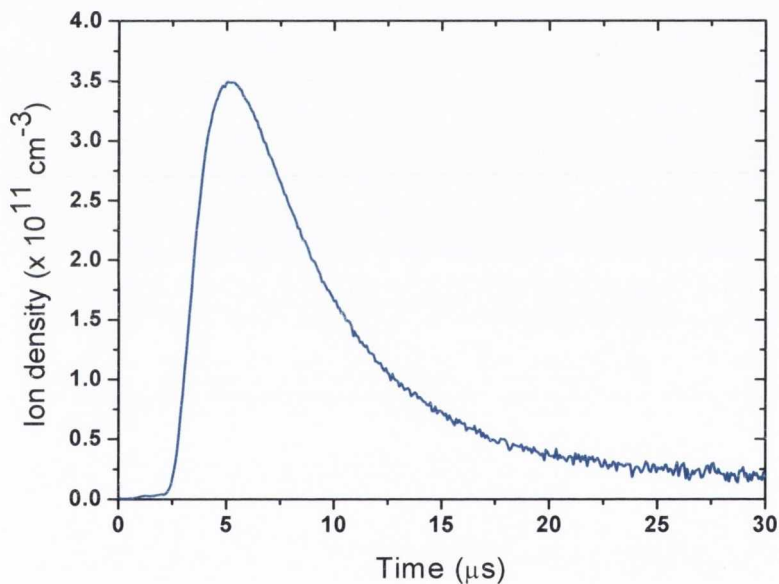
Figure 6.6 Ion density of plasma measured by Langmuir ion probe placed at 9 cm from a silver ablation target for 1.5 J cm^{-2}.

The peak ion density at the probe position is 3.5x10^{11} cm^{-3}. This is significantly less than the ion density found during confined laser ablation which was considered in chapter 4. Confined laser ablation was investigated as a technique to limit the expansion of the laser produced plasma to obtain dense long lived plasma. It is also of interest to examine the material deposited on the confining glass wall as this is essentially carrying out pulsed laser deposition (PLD) at new extreme conditions. From the plasma expansion analysis in

chapter 4, ion densities in excess of 10^{18} cm^{-3} are expected and the plasma temperature will be an order of magnitude higher than encountered in standard PLD. The deposition flux will be considerably different and it is of interest to compare films deposited in the confined geometry to PLD.

Plasma formation in the confined geometry was carried out under the same conditions as for the optical emission measurements. The laser wavelength was 1064 nm and the pulse duration was 13 ns as before. The fluence on target was 1.5 J cm^{-2} giving an irradiance of $\sim 10^8$ W cm^{-2}. A single shot was used and 76 ng of silver was removed. A scanning electron microscope (SEM) was used to image the deposits on the confining glass wall. Figure 6.7 shows three images taken using the SEM for (a) high magnification and two lower magnifications, (b) and (c).
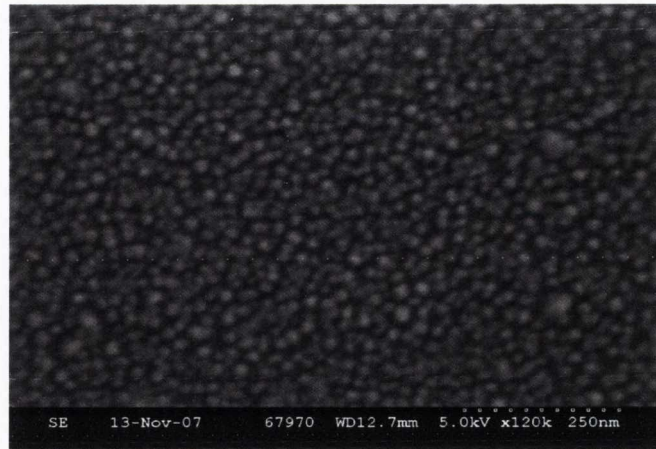
Figure 6.7 SEM images of silver deposited during confined laser ablation at 1.5 J cm^{-2} at three different magnifications. The length scale is shown in the bottom right corner.

From Fig. 6.7 (a) tightly packed nanoparticles of ≈ 25 nm in size are seen. The deposition is for one shot only so that the film equivalent thickness will be less than 4 nm which is the thickness of material ablated. From Fig. 6.7 (b) and (c) a large amount of particles of 100 –

200 nm size are observed. It is not clear at this stage if these larger particles are expelled from the target or condensed from vapour. Particulates are known to be a considerable drawback to high quality thin film growth during pulsed laser deposition and are generally seen at higher laser fluence.

The laser fluence was reduced to avoid particulate formation on the surface. Figure 6.8 shows SEM images for deposits formed at 0.5 J cm^{-2} and there is a significant decrease in the amount of larger particles that are present on the surface. The nanoparticles formed at this fluence are of size $\approx$ 50 nm and less densely packed than those observed at 1.5 J cm^{-2}.
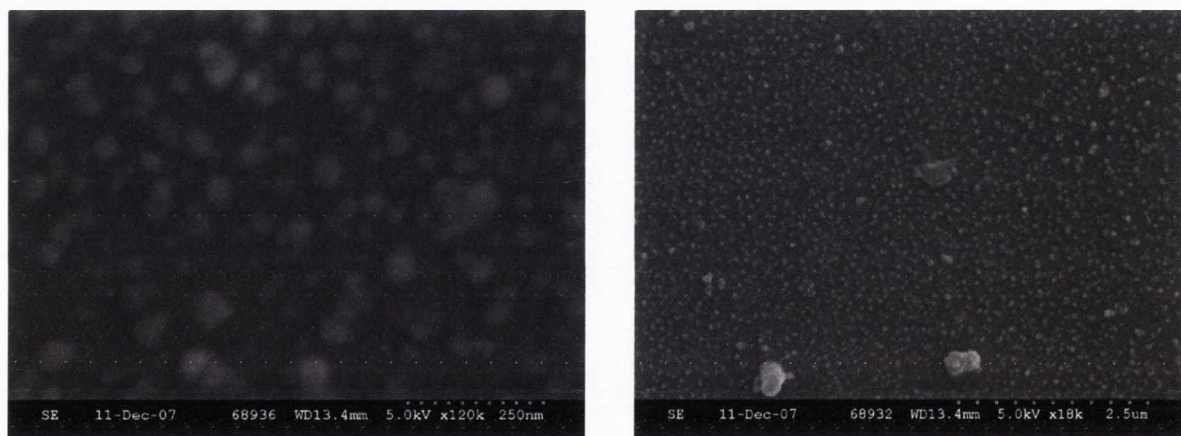
Figure 6.8 SEM images of the surface topography of deposits during confined laser ablation at 0.5 J cm^{-2}.

The UV-Vis optical absorption spectrum of the confined ablation deposits was measured and the surface plasmon resonance feature was observed indicating the presence of silver nanoparticles. Figure 6.9 shows the optical absorption spectrum from silver deposited in the confined geometry at three different fluence values.
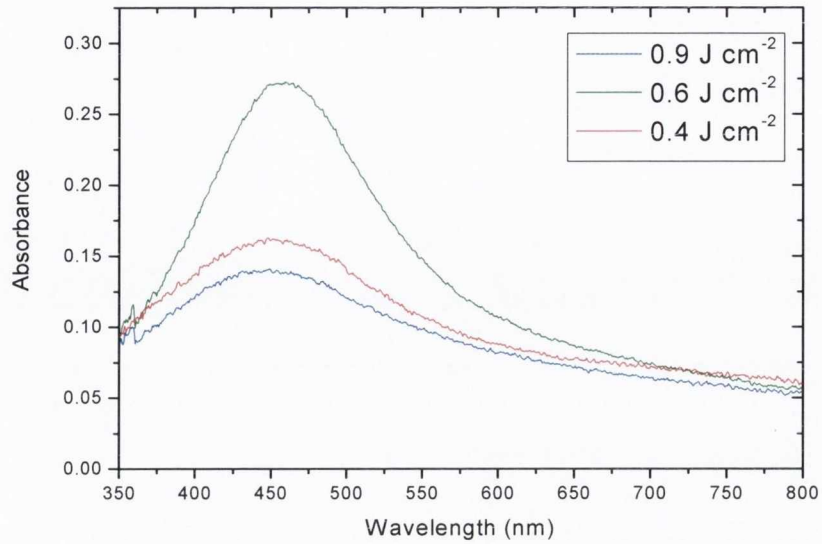
Figure 6.9 UV-Vis optical absorption spectrum of confined ablation deposition at a few different fluence values. The surface plasmon resonance around 450 nm is observed.

It seems that in the confined geometry, single shot ablation is sufficient to deposit a nanoparticle layer with high surface coverage. Comparing this to the deposition of nanoparticulate films by PLD which requires several thousands of shots, confined laser ablation represents a rapid nanofabrication technique. Fig. 6.10 compares the deposition of 1.4 nm of silver by PLD (discussed in the previous section) to the deposition from a single shot in the confined geometry. For the PLD grown films, 3,000 shots were required to grow a layer that consists of nanoparticles of ~ 10 nm in size. Confined laser ablation can achieve similar surface coverage with a single shot with 20 – 100 nm particle size. The optical response measured for the confined plasma deposits is very similar to that from PLD, which were described in the previous section. It is thought that the growth of nanoparticles during pulsed laser deposition in vacuum is due to surface diffusion of the deposited species [5].
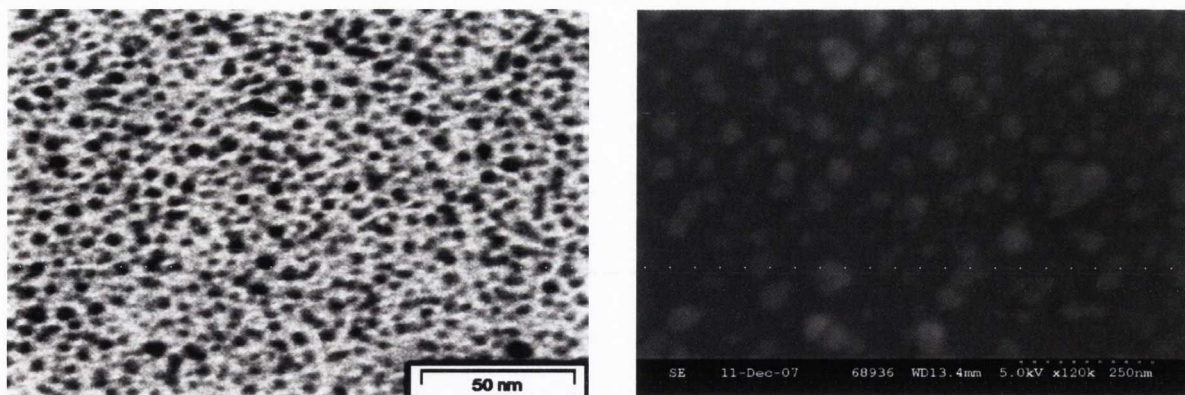
157

Figure 6.10 (a) 1.4 nm silver film grown by PLD at 9.5 cm. 3,000 248 nm laser shots at a fluence of 1 J cm^{-2} were used to deposit the film in a vacuum environment. (b) Silver film fromed from a single shot ablation in the confined geometry at 0.5 J cm^{-2}.

It has been shown that nanoparticles can form in the plume if given sufficient time to nucleate [7] and it is possible that this mechanism is responsible for formation of nanoparticles during confined ablation. Further experiments will be required to understand the growth mechanism. There is a wide scope to use confined laser ablation for novel material synthesis as it represents a rapid nano - fabrication technique for any target material. There also exists the possibility to carry out confined laser ablation in a high pressure background gas to investigate formation of multi-component nanostructured materials. In effect high temperature gas phase chemistry could be performed using confined laser ablation. As an example, ablation of aluminium in a nitrogen background gas could be investigated for growth of aluminium nitride (AlN), a material which is of interest as a wide band gap semi-conductor.

6.3 References

[1] F. Rosei, *J. Phys. C: Condens. Matter*, **16**, S1373-S1436, (2004)

[2] W. Eberhardt, *Surf. Sci.*, **500**, 242, (2002)

[3] C. N. Afonso, R. Serna, J. M. Ballesteros, A. K. Petford-Long, and R. C. Doole, *Appl. Surf. Sci.*, **127 – 129**, 339 – 343 (1998)

[4] C. N. Afonso, J. Gonzalo, R. Serna, J. C. G. de Sande, C. Ricolleau, C. Grigis, M. Gandais, D. E. Hole and P. D. Townsend, *Appl. Phys. A*, **69**, S201 – S207 (1999)

[5] S. Dolbec, E. Irissou, M. Chaker, D. Guay, F. Rosei, and M. A. El Khakani, *Phys. Rev. B*, **70**, 201406 (2004)

[6] S. Amoruso, R. Bruzzese, N. Spinelli, R. Velotta, M. Vitiello, X. Wang, G. Ausanio, V. Iannotti and L. Lanotte, *Appl. Phys. Lett.*, **84**, 4502 (2004)

[7] D.B. Geohegan, A. A. Puretzky, G. Duscher and S. J. Pennycook, *Appl. Phys. Lett.* **72**, 2987 – 2989 (1998)

[8] S. Fahler, K. Strum and H.U. Krebs, *Appl. Phys. Lett.* **75**, 24, 3768 (1999)

[9] *Optical Properties of Metal Clusters*, U. Kreibig and M. Vollmer, Springer-Verlag, New York (1995)

[10] *Absorption and Scattering of Light by Small Particles*, C. F. Bohren and D. R. Huffman, Wiley Interscience (1998)

[11] G. Xu, M. Tazawa, P. Jin and S. Nakao, *Appl. Phys. A*, **80**, 1535–1540 (2005)

Chapter 7: Conclusions and Future work

In this final chapter, the main conclusions based on the findings discussed in the preceding chapters are outlined. A future outlook is given and possible follow up experiments to build on this research are described.

7.1 Conclusions

7.1.1 Nanosecond laser ablation

From the study of the optical emission and absorption of laser plasma produced from nanosecond laser ablation of a solid silver target the following conclusions have been made.

- During the laser pulse and at short delays (10's ns) after the spectral resolved plasma emission and absorption is a broad continuum. This is not much explored in the literature and from this study it seems that the continuum emission is due to high plasma density. Severe spectral line broadening and/or bremstrahlung emission at high density are viable mechanisms that can cause this effect. Further work is required to distinguish which one is responsible and a future experiment is described in the next section.

- Confined laser ablation was investigated as a technique to produce long lived dense laser ablation plasma. The spectral line broadening is more pronounced at longer times compared to free expansion, indicating higher density with respect to that observed during free ablation. The confined plasma was used, for the first time, as a novel deposition source. It was found that extreme deposition conditions could be reached and a single shot nanoparticle deposition process was demonstrated.

- Plasma absorption was measured with a novel setup. The absorption cross section of silver laser ablation plasma formed near the ablation threshold was measured. A value of $0.5 - 1.5 \times 10^{-17}$ cm^2 was found but the technique may not be giving a

reliable measurement. A future plasma absorption experiment is described in the next section.

- Nanosecond laser ablation in vacuum has been shown to be a flexible and straight forward route to nanostructure film formation. Nanoparticulate films were observed by electron microscopy for silver deposited at equivalent thickness < 5 nm. Optical absorption spectra showed a surface plasmon resonance in the region 400 – 500 nm which is characteristic of silver nanoparticles. An effective medium theory was shown as a simple way to describe the main features of optical absorption by a silver nanoparticle film. The nanoparticle films produced from nanosecond laser ablation and from confined ablation show a very similar optical response and surface topography.

7.1.2 Femtosecond laser ablation

- For ultra-short laser ablation, comparison of the ablation depth measurements with available analytical models indicate that the energy loading to precipitate ablation is significantly lower than the heat of vaporisation used in the models. This is in agreement with more complicated molecular dynamic modelling.

- The expansion dynamics of the plasma part of the ablation products are well described by the Anisimov isentropic model of plume expansion, and the ion energy is consistent with deposited energy density near the target surface. Comparing the ion probe and deposition measurements shows that the ion fraction is < 1%. For low laser fluence it seems that the plume of nanoparticles can also be described by the Anisimov model but the physical reason why the expansion of a

162

cloud of molten, nano sized particles can be described by a gas dynamic model is unclear.

- For high fluence the nanoparticle plume is less sharply peaked in the forward direction and the shape no longer fits the Anisimov prediction. It seems that this change may be due to the increasing influence of the plasma pressure as the fluence is increased.

- This investigation of double pulse ultra-short laser ablation has shown that the addition of a second delayed pulse has a strong influence on the dynamics of the ablated material and the overall ablation process. This was ascribed to the interaction of the second laser pulse with the structured nascent plume formed by the first pulse.

- Depending on the delay different interactions take place. For delays < 10 ps the second pulse interacts with an excited surface. For delays of 10 – 100 ps the delayed pulse interacts with plasma that has formed on the target surface. The plasma ionisation is enhanced due to absorption of the delayed pulse and the ablation depth is reduced. For delays > 100 ps the plasma has expanded, the absorption is reduced and the ionisation falls. However, the ablation depth remains low.

- The fact that the ablation depth remains low at long delays, even though the absorption has fallen, seems to indicate that the plasma acts as a tamper which impedes the ejection of deeper lying layers within the region heated by the laser

pulse. A recently published molecular dynamics study [1] and hydrodynamic simulations of double pulse ablation support this hypothesis [2].

- It appears that double pulse laser ablation can produce smoother ablation craters. This occurred for long delays and may be due a tamper effect forcing deeper target layers to re-solidify during ablation.

7.2 Future work

To clarify the origin of the continuum optical emission observed during nanosecond laser ablation the following experiment is proposed. If laser ablation is carried out in the confined geometry the optical emission should be measured from the front and from the side. The emission measured at the front will include any contribution from the surface whereas the emission at the side will only be from laser produced plasma. For this experiment it would be desirable to change the gap thickness as this will allow variation of the plasma density. Then, comparing the emission measured normal to the target and from the side as a function of density it can be seen if density effects influence the optical emission profile. Figure 7.1 shows the possible target configuration for this.
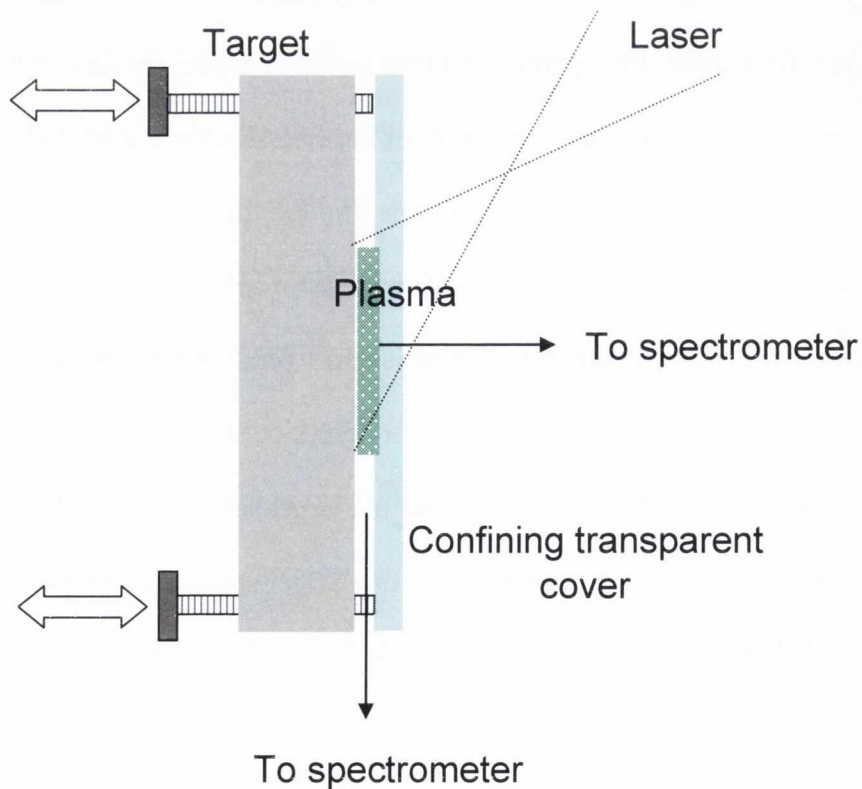
Figure 7.1 Possible target configuration for future confined plasma experiment to distinguish target and plasma emission.

The above configuration is not very different from the one used in the experiment in chapter 4.1. By replacing the fixed spacers with a set of adjustable screws and clamps to hold the cover in place (not shown) the gap distance can be changed allowing some control over the plasma density and temperature in the geometry. The laser fluence can also be changed to influence these parameters but must be kept below the ablation threshold of the confining cover.

For the above experiment, a target material other than silver will be used. This is due to the lack of available atomic data for many of the transitions in Ag I, II and III. Good atomic data exist for other elements and lithium, carbon, aluminium, magnesium and iron could all be used and these elements would be easier to simulate using available spectral codes. It would also be useful to have an independent measure of density so a technique such as interferometry would be a distinct advantage.

Depending on the outcome of this experiment a second setup could be performed to measure the plasma absorption properties in the confined plasma. If the plasmas are offset with respect to one another, a measure of the emission from each individual plasma can be made and also the emission of one plasma through the other. From the analysis in chapter 4 (Eq. 4.4) the wavelength dependant transmission and cross – section can then be found. This idea is shown in Fig. 7.2. The emission would be imaged onto the spectrometer slit and using two lasers with an ability to set delays between pulses would be an advantage. If the continuum emission is a result of the hot target surface then two separate targets will be required and the emission normal from one target should be imaged through the confined plasma.
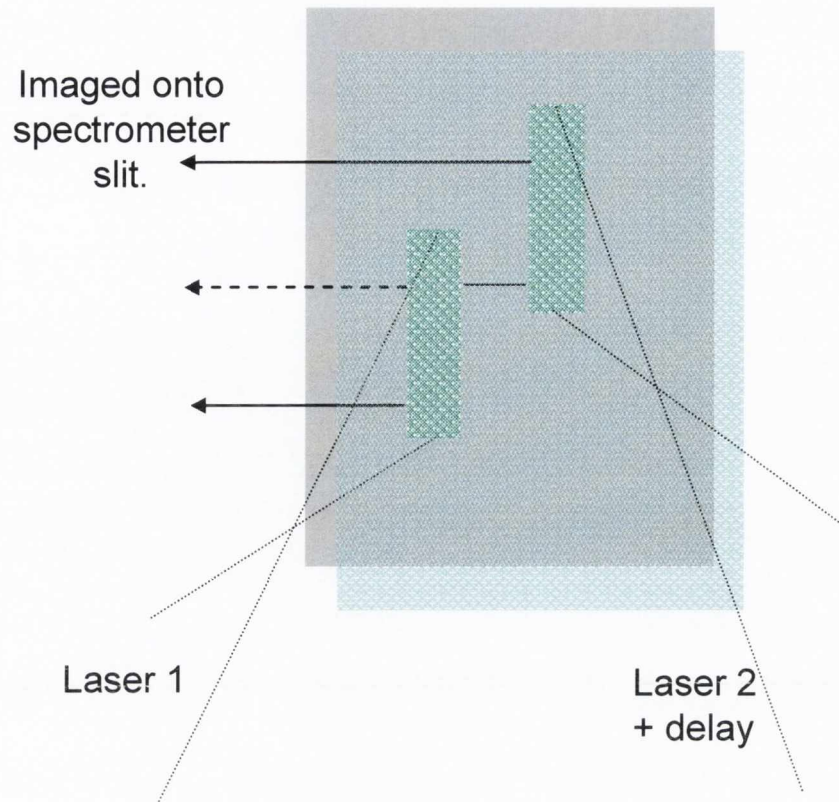
Figure 7.2 Dual plasma configuration for plasma absorption experiments.

To build on the work carried out on femtosecond laser ablation, it would be desirable to have molecular dynamic simulations to understand the exact way the ablated material is partitioned at the onset of adiabatic expansion. In our interpretation of the experimental data, the initial plumes are considered to be separated with well defined boundaries. In reality this may not be accurate and in deeper regions of the ablated material vapour and nanoparticles may co-exist. The physical reasons why the nanoparticle plume can be described by the Anisimov model also isn't clear and molecular dynamic modelling could also shed some light on this peculiar result.

To better understand the double pulse interaction and to confirm the conjecture made earlier concerning the plasma tamper effect, hydrodynamic simulations of the double pulse ultra-short laser ablation are underway in collaboration with other researchers in this field. This will shed some light on the reasons why the ablation depth values do not recover when the laser absorption is reduced as a result of the expansion of the plasma formed by the first pulse.

167

7.3 References

[1] D. Perez, L. K. Béland, D. Deryng, L. J. Lewis, and M. Meunier, Phys. Rev. B **77**, 014108 (2008)

[2] M.E. Povarnitsyn, K.V. Khishchenko, P.R. Levashov, J. Hermann, S. Noel and T.E. Itina, Oral presentation titled *"Simulation of ultrashort double pulse laser ablation of metals"*, EMRS Spring meeting (2009)

Appendices

In this section the two codes used for calculation in the thesis are given. The first is the code written in Mathematica that handles the Anisimov model calculations and the second is a code written in MathCAD that handles the optical properties of nanoparticle films calculations.

Appendix A: Mathematica code for Anisimov model calculations

Solution of the Anisimov model from the papers of Anisimov, Bauerle and Luk'yanchuk, Phys. Rev B 48, 12076 (1993) and Hansen, Schou and Lunney, Appl. Phys. A 69, S604 (1999)

S. Amoruso - May 2009 (version 2: there are new commands at the end to extract the data for origin plotting)

Loading add on ...

```
Needs["PlotLegends`"];
```

Definition of the problem and variables

The model considers the three - dimensional isentropic (adiabatic) self - similar solution of the gasdynamical equations describing the expansion of a plasma plume of energy Ep and mass Mp. As this variables appears as a ratio Ep/Mp they can be also considered (as here) as the energy and mass of a single particle in the plume, a variable which can be determined experimentally. This are related in the value of $\beta=(5\gamma-3)$ Ep/Mp, γ being the adiabatic exponent of the plume. The initial plume has an ellipsoidal shape with dimension 2 X0 and 2 Y0 in the plane of the target and a thickess Z0 along the normal to the target surface. At later time (t), the boundaries of the plume are given by X(t), Y(t) and Z(t) along the respective axes x, y and z. x indicates the axis along the larger dimesion of the initial plume, y indicates the axes along the smaller dimension of the inizial plume and z is the axis of the target normal. For a simmetric plume X0=Y0=R0 and X(t)=Y(t)=R(t). See the schematic drawing and note in the file Anisimov.doc.

Dimensionless variables are introduced to solve the equations, as follows: $\tau=t/t0=t/(X0/\sqrt{\beta}$); $\xi=X/X0$; $\eta=Y/X0$; $\zeta==Z/X0$; $\xi0=X0/X0=1$; $\eta0=Y0/X0$; $\zeta0==Z0/X0$.
SI units and dimensionless variables are used in the following.

```
Clear[X, X0, Y, Y0, Z, Z0, t, τ, ξ, η, ζ, η0, ξ0, γ, β, Ep, Mp, g1, g2, g12, sol1, sol2];

X0 = 200. 10⁻⁶; Y0 = 100. 10⁻⁶; Z0 = 0.135×10⁻⁶; (* initial plume dimensions, in m *)

γ = 1.25 ; (* adiabatic coefficient *)

Ep = 20×1.602 10⁻¹⁹;
(* energy per particle in J = energy per particle in eV × electron charge in C *)

Mp = 58.70 * 1.66 * 10⁻²⁷;
(* mass of the particle in kg = mass of the particle in u × unit atomic mass *)
```

$$\beta := (5\gamma - 3) \frac{Ep}{Mp}$$

```
    (* β parameter of the model defining the time-scale parameter - time t=(X0/√β)τ *)
```

$$\xi[t] := \frac{X[t]}{X0}; \ \eta[t] := \frac{Y[t]}{X0}; \ \zeta[t] := \frac{Z[t]}{X0}; \ (* \text{ definition of the dimensionless variables } *)$$

$$\tau[t] := \frac{t \sqrt{\beta}}{X0} ; \; \xi 0 = \frac{X0}{X0} ; \; \eta 0 = \frac{Y0}{X0} ; \; \zeta 0 := \frac{Z0}{X0} ; \; (* \text{ dimensionless time } \tau,$$

plume initial in-plane, $\eta 0$, and normal aspect ratio, $\zeta 0$ *)

$$t0 = \frac{X0}{\sqrt{\beta}} \; (* \text{ time scale parameter in seconds, the time } t = \tau \; t0 \; *)$$

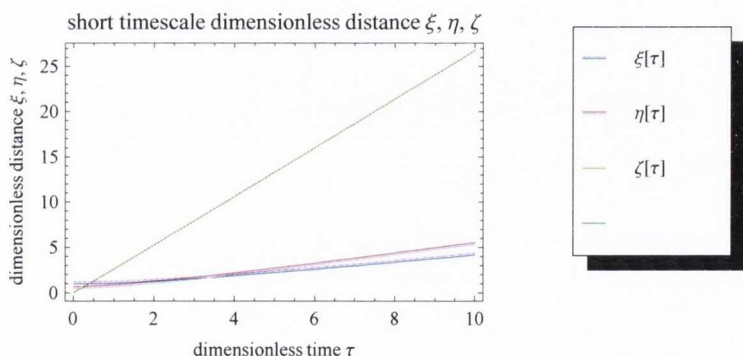1.93471×10^{-8}

$$u0 = \sqrt{\frac{2 \, Ep}{Mp}}$$

8109.39

Solution of the equation in dimensionless variables for short and long timescale, and plots of the results as a function of τ

solution for short timescale and corresponding plots

$$\text{sol1} = \text{NDSolve}\left[\left\{\xi[\tau] \; \xi''[\tau] == \eta[\tau] \; \eta''[\tau] == \zeta[\tau] \; \zeta''[\tau] == \left(\frac{\eta 0 \; \zeta 0}{\xi[\tau] \; \eta[\tau] \; \zeta[\tau]}\right)^{(\gamma-1)}\right.,\right.$$

$$\xi[0] == 1, \; \eta[0] == \eta 0, \; \zeta[0] == \zeta 0, \; \xi'[0] == 0, \; \eta'[0] == 0, \; \zeta'[0] == 0\},$$

$$\left.\{\xi, \eta, \zeta\}, \left\{\tau, 1 \, 10^{-2}, 1 \, 10^{1}\right\}\right] \; (* \text{ short timescale } *)$$

$\{\{\xi \to \text{InterpolatingFunction}[\{\{0.01, 10.\}\}, <>],$
$\quad \eta \to \text{InterpolatingFunction}[\{\{0.01, 10.\}\}, <>], \; \zeta \to \text{InterpolatingFunction}[\{\{0.01, 10.\}\}, <>]\}\}$

$$\text{Plot}\left[\text{Evaluate}[\{\xi[\tau], \eta[\tau], \zeta[\tau]\} /. \text{sol1}], \left\{\tau, 1 \, 10^{-2}, 1 \, 10^{1}\right\}, \text{PlotRange} \to \text{All},\right.$$

$\quad$ Frame $\to$ True, FrameLabel $\to$ {"dimensionless time τ", "dimensionless distance ξ, η, ζ"},

$\quad$ PlotLabel $\to$ "short timescale dimensionless distance ξ, η, ζ",

$\quad$ PlotLegend $\to$ {"$\xi[\tau]$", "$\eta[\tau]$", "$\zeta[\tau]$"}, LegendPosition -> {1, -0.25}$\Big]$

```
Plot[Evaluate[η[τ] / ξ[τ] /. sol1], {τ, 1 10⁻², 1 10¹}, PlotRange → All ,
  Frame → True, FrameLabel → {"dimensionless time τ", "in-plane aspect ratio η/ξ"},
  PlotLabel → "short timescale in-plane aspect ratio η/ξ"]
```


short timescale in−plane aspect ratio η/ξ

```
Plot[Evaluate [ζ[τ] / ξ[τ] /. sol1], {τ, 1 10⁻², 1 10¹}, PlotRange → All ,
  Frame → True, FrameLabel → {"dimensionless time τ", "normal aspect ratio ζ/η"},
  PlotLabel → "short timescale normal aspect ratio ζ/ξ",
  PlotLabel → "short timescale in-plane aspect ratio η/ξ"]
```


short timescale normal aspect ratio ζ/ξ
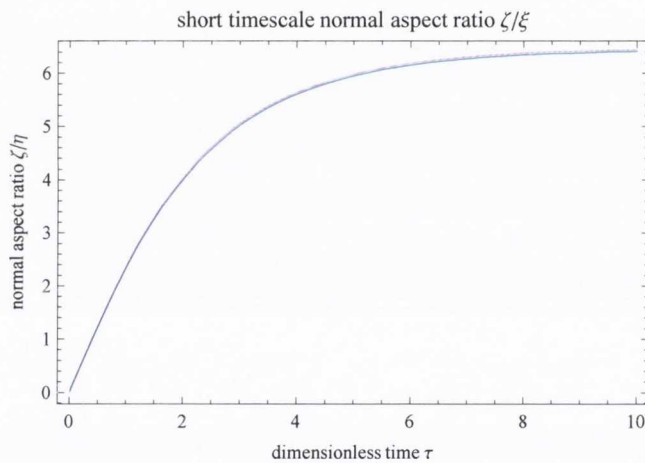
solution for long timescale and corresponding plots

$$\text{sol2} = \text{NDSolve}\left[\left\{\xi[\tau]\,\xi''[\tau] == \eta[\tau]\,\eta''[\tau] == \zeta[\tau]\,\zeta''[\tau] == \left(\frac{\eta 0\,\zeta 0}{\xi[\tau]\,\eta[\tau]\,\zeta[\tau]}\right)^{(\gamma-1)}, \xi[0] == 1,\right.\right.$$

$$\left.\left. \eta[0] == \eta 0,\ \zeta[0] == \zeta 0,\ \xi'[0] == 0,\ \eta'[0] == 0,\ \zeta'[0] == 0\right\}, \{\xi, \eta, \zeta\}, \left\{\tau, 1\,10^{-1}, 1\,10^4\right\}\right]$$

```
{{ξ → InterpolatingFunction [{{0.1, 10000.}}, <>],
  η → InterpolatingFunction [{{0.1, 10000.}}, <>],
  ζ → InterpolatingFunction [{{0.1, 10000.}}, <>]}}
```

```
Plot[Evaluate [{ξ[τ], η[τ], ζ[τ]} /. sol2], {τ, 1 10⁻¹, 1 10⁴ }, PlotRange → All ,
  Frame → True, FrameLabel → {"dimensionless time τ", "dimensionless distance ξ, ζ"},
  PlotLabel → "long timescale dimensionless distance ξ, ζ",
  PlotLegend → {"ξ[τ]", "η[τ]", "ζ[τ]"}, LegendPosition -> {1, -0.25}]
```


plot and evaluation of the limit velocity of the plume edges

```
vξ[τ] := ∂τ ξ[τ]; vη[τ] := ∂τ η[τ]; vζ[τ] := ∂τ ζ[τ]
```

```
Plot[Evaluate[{vξ[τ], vη[τ], vζ[τ]} /. sol2], {τ, 0.1, 10⁴ }, PlotRange → All , Frame → True,
  FrameLabel → {"dimensionless time τ", "dimensionless velocity vξ,vη,vζ"},
  PlotLabel → "long timescale dimensionless velocity vξ,vη,vζ",
  PlotLegend → {"vξ[τ]", "vη[τ]", "vζ[τ]"}, LegendPosition -> {1, -0.25}]
```
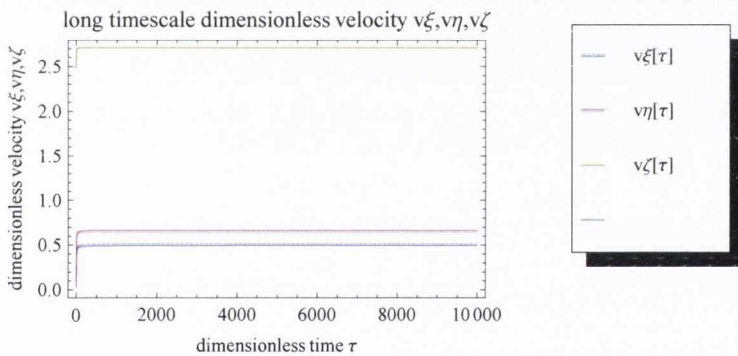

$$v\xi lim = \frac{Extract\left[Evaluate\left[\xi\left[10\ 10^3\right]\ /.\ sol2\right],\ 1\right] - Extract\left[Evaluate\left[\xi\left[9\ 10^3\right]\ /.\ sol2\right],\ 1\right]}{10\ 10^3 - 9\ 10^3}$$

0.493301

$$v\eta lim = \frac{Extract\left[Evaluate\left[\eta\left[10\ 10^3\right]\ /.\ sol2\right],\ 1\right] - Extract\left[Evaluate\left[\eta\left[9\ 10^3\right]\ /.\ sol2\right],\ 1\right]}{10\ 10^3 - 9\ 10^3}$$

0.643339

$$v\zeta lim = \frac{Extract\left[Evaluate\left[\zeta\left[10\ 10^3\right]\ /.\ sol2\right],\ 1\right] - Extract\left[Evaluate\left[\zeta\left[9\ 10^3\right]\ /.\ sol2\right],\ 1\right]}{10\ 10^3 - 9\ 10^3}$$

2.70954

plots of the aspect ratios: in-plane $k\eta\xi=\eta/\xi$, and on-axis $k\zeta\xi=\zeta/\xi$ and $k\zeta\eta=\zeta/\eta$
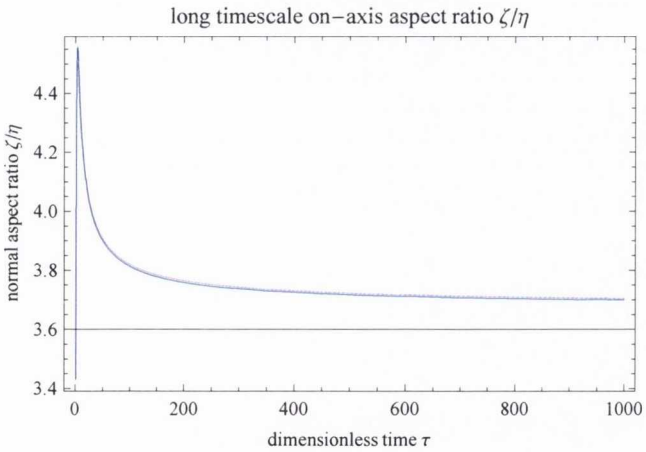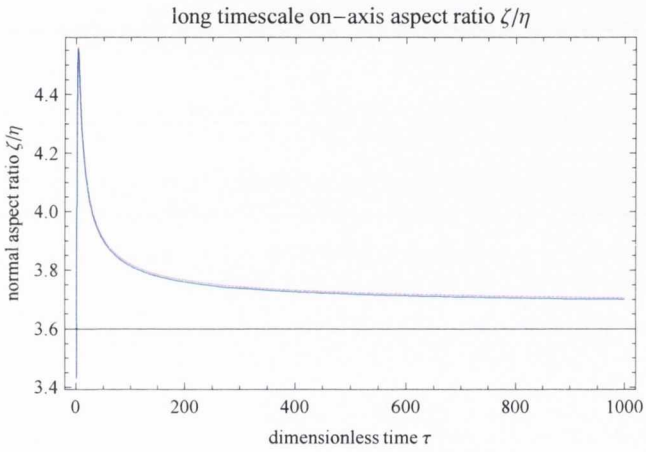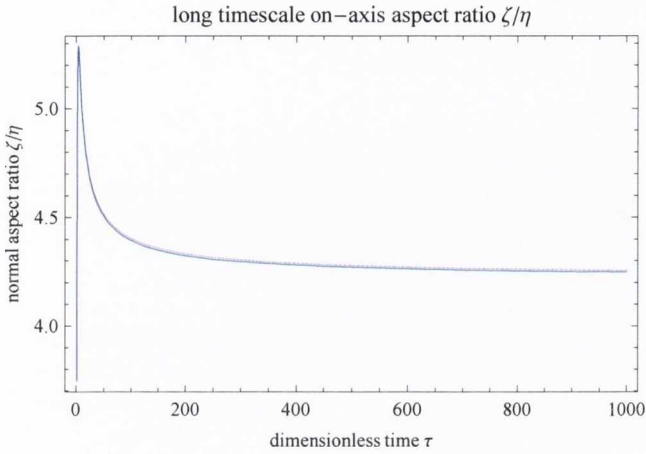
173

```
Plot[Evaluate[η[τ] / ξ[τ] /. sol2], {τ, 1, 1 10³}, PlotRange → All , Frame → True,
  FrameLabel → {"dimensionless time τ", "in-plane aspect ratio η/ξ"},
  PlotLabel → "long timescale in-plane aspect ratio η/ξ"]
```
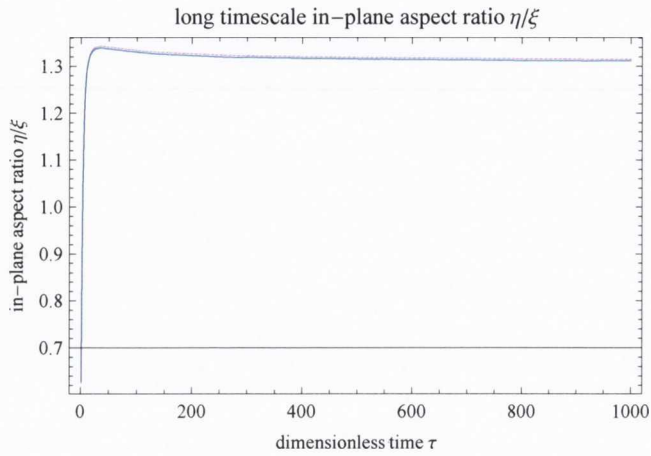

long timescale in−plane aspect ratio η/ξ

```
Plot[Evaluate[ζ[τ] / ξ[τ] /. sol2], {τ, 1, 1 10³}, PlotRange → All ,
  Frame → True, FrameLabel → {"dimensionless time τ", "normal aspect ratio ζ/ξ"},
  PlotLabel → "long timescale on-axis aspect ratio ζ/ξ"]
```


long timescale on−axis aspect ratio ζ/ξ

174

```
Plot[Evaluate[ζ[τ] / η[τ] /. sol2], {τ, 1, 1 10³}, PlotRange → All ,
  Frame → True, FrameLabel → {"dimensionless time τ", "normal aspect ratio ζ/η"},
  PlotLabel → "long timescale on-axis aspect ratio ζ/η"]
```
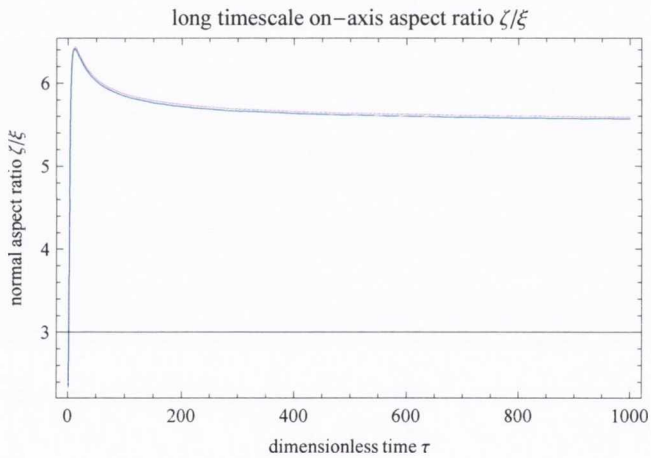

long timescale on−axis aspect ratio ζ/η

long timescale on−axis aspect ratio ζ/η

long timescale on−axis aspect ratio ζ/η

In-plane Aspect ratio at long timescale η/ξ- kyx value related to the elliptical shape of the plume section in the Y,X plane (kyx=Y(t)/X(t) with t->∞) compared to the initial aspect ratio kyxinitial evaluated at τ=0

175

```
kyx = Extract[Evaluate[η[1 10⁴] / ξ[1 10⁴] /. sol2], 1]
```

1.30511

$$\text{kyxinitial} = \frac{\eta 0}{\xi 0}$$

0.5

> **On-Axis Aspect ratio at long timescale ζ/ξ - kzx value of the angular distribution in the X,Z plane and Angular distribution in the X,Z plane (kzx=Z(t)/X(t) with t->∞)**

```
kzx = Extract[Evaluate[ζ[1 10⁴] / ξ[1 10⁴] /. sol2], 1]
```
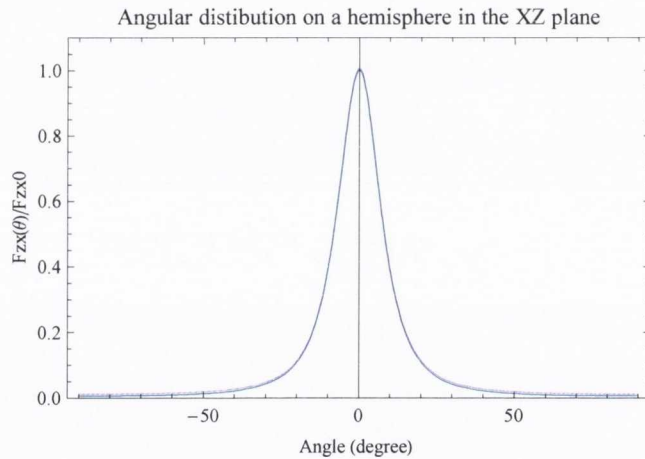
5.50303

Angular distribution on a hemisphere in the X,Z plane [This is our experimental case]

$$\text{Fzx}[\theta\_] := \left(1 + \text{Tan}\left[\frac{\pi}{180.}\theta\right]^2\right)^{\frac{3}{2}} \left(1 + \text{kzx}^2 \text{Tan}\left[\frac{\pi}{180.}\theta\right]^2\right)^{-\frac{3}{2}}$$

```
Plot[Fzx[θ], {θ, -90, 90}, PlotRange → {0, 1.1},
  Frame → True, FrameLabel → {"Angle (degree) ", "Fzx(θ)/Fzx0"},
  PlotLabel → "Angular distibution on a hemisphere in the XZ plane"]
```


Angular distibution on a hemisphere in the XZ plane

Angular width in degree Δθzx for deposition on a hemisphere in the X,Z plane [This is our experimental case]

$$\Delta\theta\text{zx} = 2\,\text{ArcTan}\left[\sqrt{\left(\frac{2^{\frac{2}{3}} - 1}{\text{kzx}^2 - 2^{\frac{2}{3}}}\right)}\right] \quad (* \text{ angular full width, in radiant } *)$$

0.284217

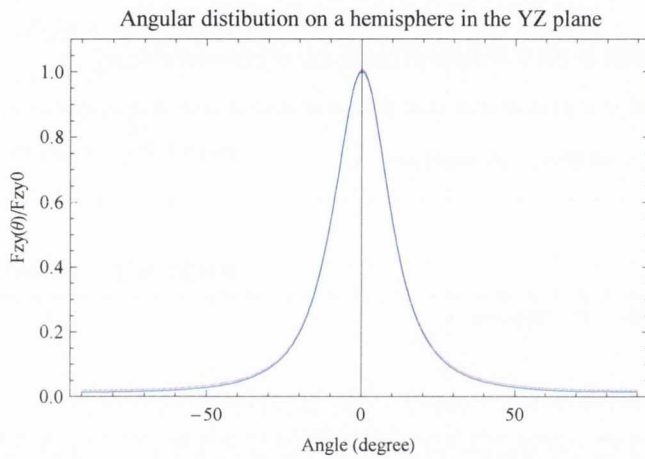$$\Delta\theta\text{zxdegree} = \frac{180}{\pi}\,\Delta\theta\text{zx} \quad (* \text{ angular full width, in degree } *)$$

16.2844

```
kzy = Extract[Evaluate[ζ[1 10⁴] / η[1 10⁴] /. sol2], 1]
```

4.21653

Angular distribution on a hemisphere in the Y,Z plane [This is not our experimental case]

$$\text{Fzy}[\theta\_] := \left(1 + \text{Tan}\left[\frac{\pi}{180.}\theta\right]^2\right)^{\frac{3}{2}} \left(1 + \text{kzy}^2 \text{Tan}\left[\frac{\pi}{180.}\theta\right]^2\right)^{-\frac{3}{2}}$$

```
Plot[Fzy[θ], {θ, -90, 90}, PlotRange → {0, 1.1},
 Frame → True, FrameLabel → {"Angle (degree) ", "Fzy(θ)/Fzy0"},
 PlotLabel → "Angular distibution on a hemisphere in the YZ plane"]
```


Angular distibution on a hemisphere in the YZ plane

Angular width in degree $\Delta\theta$zy for deposition on a hemisphere in the Y,Z plane[This is not our experimental case]

$$\Delta\theta\text{zy} = 2 \text{ArcTan}\left[\sqrt{\left(\frac{2^{\frac{2}{3}} - 1}{\text{kzy}^2 - 2^{\frac{2}{3}}}\right)}\right] \quad (* \text{ angular full width, in radiant } *)$$

0.376427

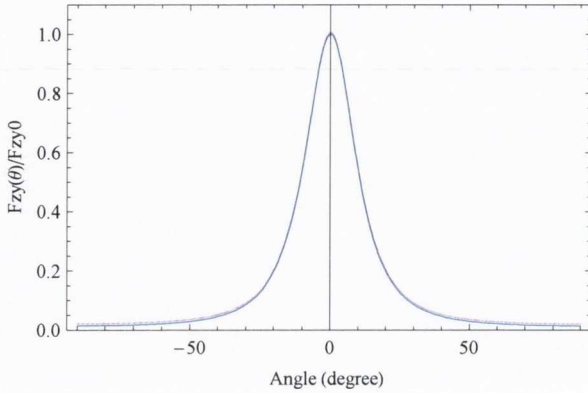$$\Delta\theta\text{zydegree} = \frac{180}{\pi} \Delta\theta\text{zy} \quad (* \text{ angular full width, in degree } *)$$

21.5677

Angular distribution for deposition on a plane in the Y,Z plane, corresponding to what we have in our case in the YZ plane [This is our experimental case]

$$\text{Fzyp}[\theta\_] := \left(1 + \text{kzy}^2 \text{Tan}\left[\frac{\pi}{180.}\theta\right]^2\right)^{-\frac{3}{2}}$$

177

```
Plot[Fzy[θ], {θ, -90, 90}, PlotRange → {0, 1.1},
 Frame → True, FrameLabel → {"Angle (degree) ", "Fzy(θ)/Fzy0"},
 PlotLabel → "Angular distibution of the deposition on a plane substrate in the YZ plane"]
```

ngular distibution of the deposition on a plane substrate in the YZ plar

Angular width in degree Δθzyp for deposition on a plane substrate in the Y,Z plane [This is our experimental case]

$$\Delta\theta zyp = 2 \, \text{ArcTan}\left[\sqrt{\left(\frac{2^{\frac{2}{3}} - 1}{kzy^2}\right)}\right] \quad (* \text{ angular full width, in radiant } *)$$
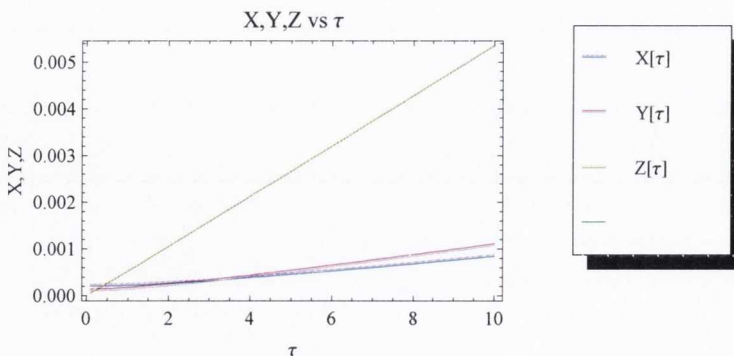
0.359606

$$\Delta\theta zydegree = \frac{180}{\pi} \, \Delta\theta zyp \quad (* \text{ angular full width, in degree } *)$$

20.6039

Plume edges X, Y, and Z as a function τ (which can be rescaled to real time t by using t=t0 τ) and plume edges' velocities vX, vY, vZ
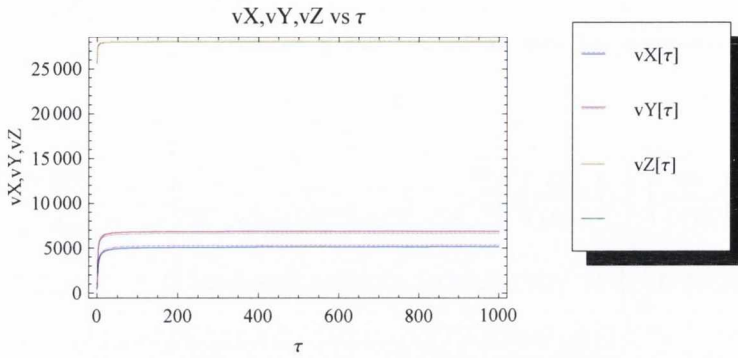
```
X[τ] := X0 ξ[τ]; Y[τ] := X0 η[τ]; Z[τ] := X0 ζ[τ]
```

```
Plot[Evaluate[{X[τ], Y[τ], Z[τ]} /. sol2], {τ, 0.1, 10¹},
 PlotLegend → {"X[τ]", "Y[τ]", "Z[τ]"}, LegendPosition -> {1, -0.25},
 Frame → True, FrameLabel → {"τ", "X,Y,Z"}, PlotLabel → "X,Y,Z vs τ"]
```



```
vX[τ] := t0⁻¹ ∂τ X[τ]; vY[τ] := t0⁻¹ ∂τ Y[τ]; vZ[τ] := t0⁻¹ ∂τ Z[τ]
```

```
Plot[Evaluate[{vX[τ], vY[τ], vZ[τ]} /. sol2], {τ, 0.1, 10³},
  PlotLegend → {"vX[τ]", "vY[τ]", "vZ[τ]"}, LegendPosition -> {1, -0.25},
  Frame → True, FrameLabel → {"τ", "vX,vY,vZ"}, PlotLabel → "vX,vY,vZ vs τ"]
```



```
vXlim = √β̄ vξlim
```

5099.49

```
vYlim = √β̄ vηlim
```

6650.51

```
vZlim = √β̄ vζlim
```

28 009.8

<div style="background-color: yellow;">
TOF profile as a function of θp and τ (which can be rescaled to real time t by using t=t0 τ) - the probe is in the XZ plane - Both the exact formula and the approximate formula for the TOF profile are considered. In the second case the plume edge variation is approximated by X(t)=vXlim t; Y(t)=vYlim t; Z(t)=vZlim t, where t=t0 τ. The formula is for the collection on a hemisphere.
</div>

```
θp = 0. (* probe angle, degree *)
```

0.

```
Lp = 64. 10⁻³ (* probe distance in m *)
```

0.064

```
ts = Lp / vZlim
   (* time at which the plume front edge along the normal reaches a probe at θp=0 *)
```

2.28491×10^{-6}

```
        ts
τs = ———
        t0
```

118.101

```
         ⌠1          1
I1 = 2 π ⎮ s² (1 - s²)^(γ-1) ds (* parameter of the Anisimov model, function of γ *)
         ⌡0
```

0.232106

$xp = Lp \, Sin\left[\dfrac{\pi}{180} \, \theta p\right]$ (* position coordinate of the probe in the x direction *)

0.

$zp = Lp \, Cos\left[\dfrac{\pi}{180} \, \theta p\right]$ (* position coordinate of the probe in the y direction *)
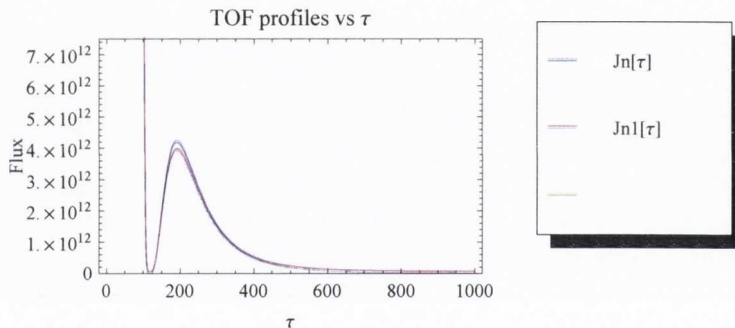
0.064

$Jn[\tau] := \dfrac{1}{I1} \, (X[\tau] \, Y[\tau] \, Z[\tau])^{-1} \left(1 - \left(\dfrac{xp}{X[\tau]}\right)^2 - \left(\dfrac{zp}{Z[\tau]}\right)^2\right)^{\frac{1}{\gamma-1}}$

$\left(\left(\dfrac{xp}{X[\tau]} \, \dfrac{1}{t0} \, \partial_\tau \, X[\tau]\right)^2 + \left(\dfrac{zp}{Z[\tau]} \, \dfrac{1}{t0} \, \partial_\tau \, Z[\tau]\right)^2\right)$ (* TOF profile - exact formula *)

$Jn1[\tau] := \dfrac{1}{I1} \left(vXlim \, vYlim \, vZlim \, t0^3 \, \tau^3\right)^{-1} \left(1 - \left(\dfrac{xp}{vXlim \, t0 \, \tau}\right)^2 - \left(\dfrac{zp}{vZlim \, t0 \, \tau}\right)^2\right)^{\frac{1}{\gamma-1}}$

$\left(\left(\dfrac{xp}{vXlim \, t0 \, \tau} \, vXlim\right)^2 + \left(\dfrac{zp}{vZlim \, t0 \, \tau} \, vZlim\right)^2\right)$ (* TOF profile - approximate formula *)

$Plot\left[Evaluate[\{Jn[\tau], Jn1[\tau]\} \, /. \, sol2], \, \{\tau, 0.1, 1 \, 10^3\}, \, PlotRange \to \{0, 7.5 \, 10^{12}\},\right.$
$PlotLegend \to \{"Jn[\tau]", "Jn1[\tau]"\}, \, LegendPosition \to \{1, -0.25\},$
$\left.Frame \to True, \, FrameLabel \to \{"\tau", "Flux"\}, \, PlotLabel \to "TOF \, profiles \, vs \, \tau"\right]$

$Jn2[t\_] := \dfrac{1}{I1} \, (vXlim \, vYlim \, vZlim)^{-1} \, t^{-5} \left(1 - \left(\dfrac{xp}{vXlim \, t}\right)^2 - \left(\dfrac{zp}{vZlim \, t}\right)^2\right)^{\frac{1}{\gamma-1}}$

$\left(xp^2 + zp^2\right)$ (* TOF profile - approximate formula as a function of time t *)

180

```
Plot[Jn2[t], {t, 0, 1.5 10⁻⁵}, PlotRange → {0, 3. 10¹²}, Frame → True,
  FrameLabel → {"time t (s)", "Flux"}, PlotLabel → "approximate TOF profiles vs time"]
```
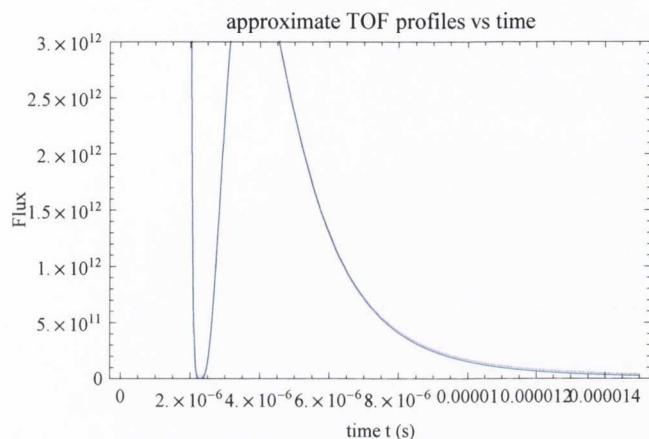

Find the time at which there is a minimum and maximum in the TOF profile : ine of these is the peak time

```
Solve[∂ₜ Jn2[t] == 0., t]
```

$$\{\{t \to -3.68431 \times 10^{-6}\}, \{t \to -2.28491 \times 10^{-6}\}, \{t \to -2.28491 \times 10^{-6}\}, \{t \to -2.28491 \times 10^{-6}\},$$
$$\{t \to 2.28491 \times 10^{-6}\}, \{t \to 2.28491 \times 10^{-6}\}, \{t \to 2.28491 \times 10^{-6}\}, \{t \to 3.68431 \times 10^{-6}\}\}$$

Commands line to export data for the dynamics and the TOF profile in txt format for the origin plots
Export["directory\filename",list,"Table"]

Plume expansion dynamics in dimensionless variables: short time (sol1) and long time (sol2). All the overall dynamics is put in one list (dynamics) . The velocities and aspect ratios are directly calculated in the origin file starting from the dynamics plots.

```
dynamics = {};

AppendTo[dynamics, {0, ξ0, η0, ζ0}]

{{0, 1., 0.5, 0.000675}}

Do[
  τ = 1. 10⁻¹ + (i - 1) 10⁻¹;
  AppendTo[dynamics, {τ, Extract[Evaluate[ξ[τ]] /. sol1, 1],
    Extract[Evaluate[η[τ]] /. sol1, 1], Extract[Evaluate[ζ[τ]] /. sol1, 1]}],
  {i, 1, 99}
]

Do[
  τ = 1. 10⁺¹ + (i - 1) 10⁰;
  AppendTo[dynamics, {τ, Extract[Evaluate[ξ[τ]] /. sol2, 1],
    Extract[Evaluate[η[τ]] /. sol2, 1], Extract[Evaluate[ζ[τ]] /. sol2, 1]}],
  {i, 1, 999}
]

dynamics // MatrixForm;
```
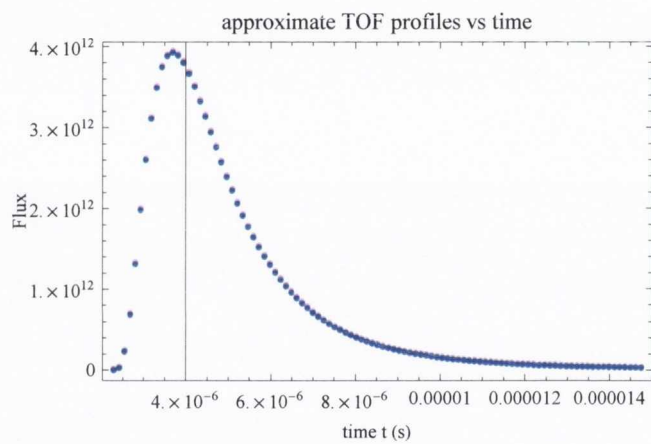
```
dynamics ;(* remove ; to see the list *)

Export["C:\Anisimov_code_output\dynamicsvstime.txt", dynamics, "Table"]

C:\Anisimov_code_output\dynamicsvstime.txt
```

Plume expansion TOF profile in real time coordinates.

```
TOF = {};

Do[
   time = ts + (1.5 10^-5 - ts)/100 (i - 1);
   AppendTo[TOF, {time, Jn2[time]}],
   {i, 1, 99}
]

ListPlot[TOF, PlotRange → All, Frame → True,
  FrameLabel → {"time t (s)", "Flux"}, PlotLabel → "approximate TOF profiles vs time"]
```



```
Export["C:\Anisimov_code_output\TOF.txt", TOF, "Table"]

C:\Anisimov_code_output\TOF.txt
```

Generation of the TOF profile in real time coordinates used in the experiment with the same step of the bin used in the acquisition.

```
TOF1 = {};

Do[
   time = 0.04 10^-6 i;
   AppendTo[TOF1, {time / 10^-6, Jn2[time]}],
   {i, 1, 1000}
]
```

182

```
ListPlot[TOF1, PlotRange → {0, 0.5 10¹³}, Frame → True,
  FrameLabel → {"time t (s)", "Flux"}, PlotLabel → "approximate TOF profiles vs time"]
```


approximate TOF profiles vs time
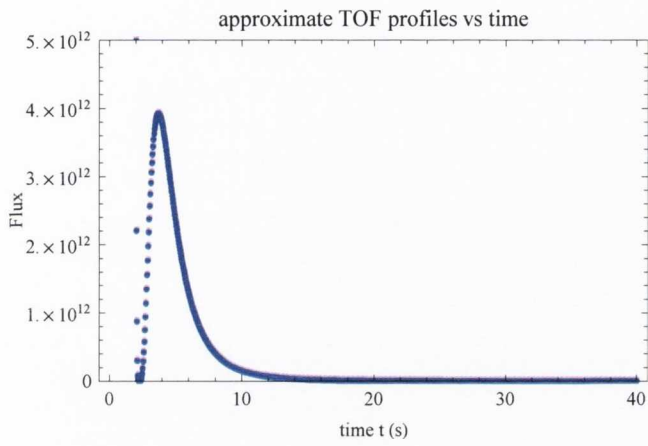
```
Export[
  "D:\Collaborations\Irlanda\Singlepulse_Ni-2008\Anisimov_plots\TOF1.dat", TOF1, "Table"]
```
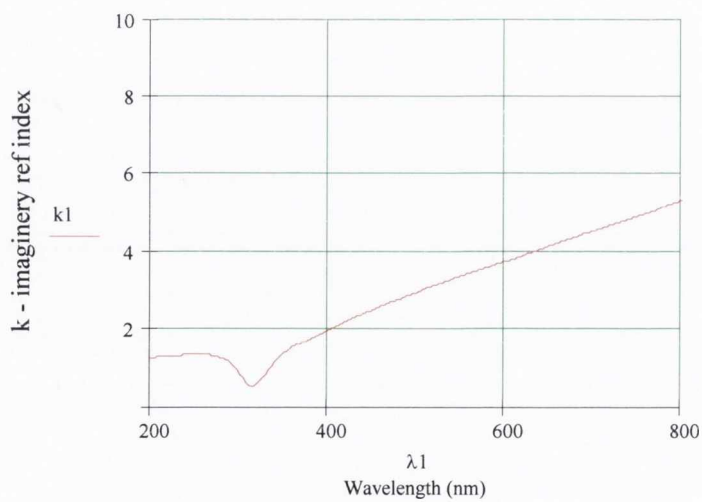
Export::nodir : Directory D:\Collaborations\Irlanda\Singlepulse_Ni-2008\Anisimov_plots\ does not exist.

```
$Failed
```

Appendix B: MathCAD code for Maxwell-Garnett calculation of optical properties of silver nanoparticle films

Data1 :=

⌷

I:\..\Ag Data Interpolated.txt

Reading in real and imaginary refractive indices values n(λ) and k(λ) for bulk silver

$\lambda 1 := Data1^{<0>}$

Wavelength in nm

$n1 := Data1^{<1>}$

Real refractive index

$k1 := Data1^{<2>}$

Imaginery refractive index

$n_{ref} := n1 - i \cdot k1$

Total refractive index

Silver bulk refractive indices as a function of wavelength

184
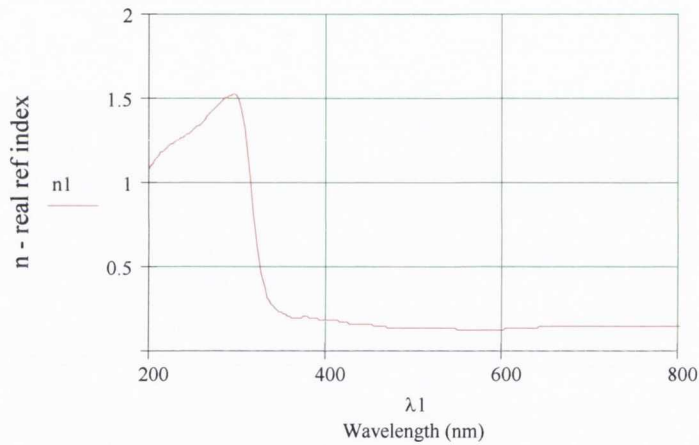
Calculating bulk dielectric function, ε(λ), of silver

$$i := \sqrt{-1}$$

$$\varepsilon 1 := \overrightarrow{\left(n1^2 - k1^2 \right)}$$ **Real componet of dielectric coefficient**

$$\varepsilon 2 := \overrightarrow{\left(2 \cdot n1 \cdot k1 \right)}$$ **Imaginery componet of dielectric coefficient**

$$\varepsilon_{Ag} := \varepsilon 1 + i \cdot \varepsilon 2$$ **Dielectric coefficient of bulk silver**

Silver bulk dielectric coefficient as a function of wavelength

λ1
Wavelength (nm)

λ1
Wavelength (nm)

185
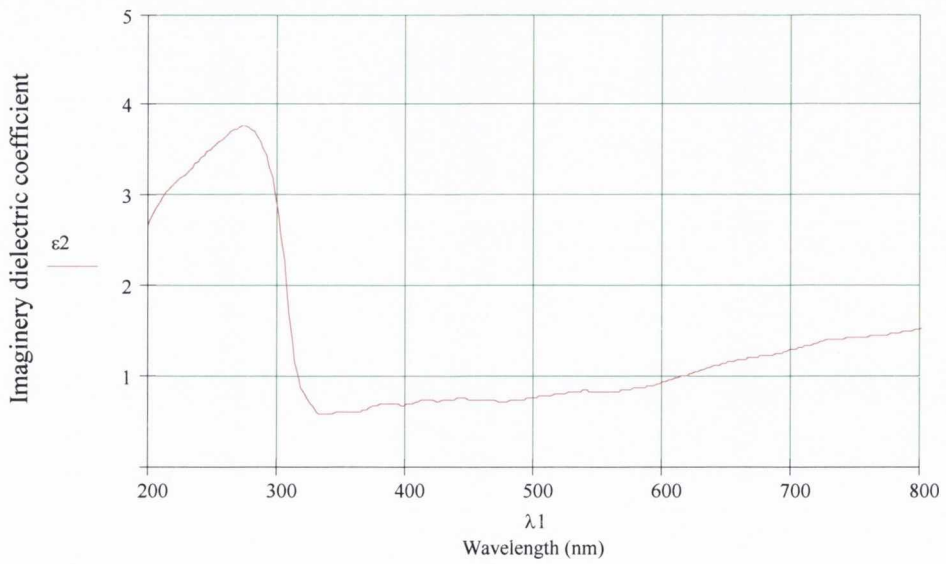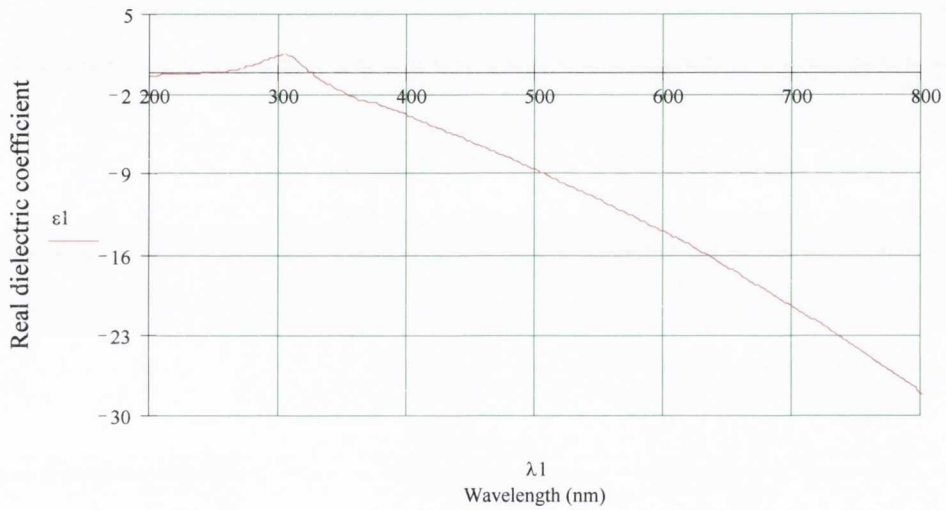
Arrays showing first few values of above functions

$\lambda 1 =$

	0
0	200
1	202.293
2	204.586
3	206.879
4	209.172
5	211.465
6	213.758
7	216.051
8	218.344
9	220.637
10	222.93
11	225.223
12	227.516
13	229.809
14	232.102

$n1 =$

	0
0	1.072
1	1.09
2	1.109
3	1.127
4	1.142
5	1.157
6	1.173
7	1.183
8	1.194
9	1.204
10	1.214
11	1.222
12	1.23
13	1.239
14	1.246

$k1 =$

	0
0	1.24
1	1.254
2	1.264
3	1.271
4	1.277
5	1.284
6	1.29
7	1.293
8	1.296
9	1.299
10	1.302
11	1.305
12	1.307
13	1.31
14	1.316

$n_{ref} =$

	0
0	1.072-1.24i
1	1.09-1.254i
2	1.109-1.264i
3	1.127-1.271i
4	1.142-1.277i
5	1.157-1.284i
6	1.173-1.29i
7	1.183-1.293i
8	1.194-1.296i
9	1.204-1.299i
10	1.214-1.302i
11	1.222-1.305i
12	1.23-1.307i
13	1.239-1.31i
14	1.246-1.316i

$\varepsilon 1 =$

	0
0	-0.388
1	-0.384
2	-0.369
3	-0.345
4	-0.327
5	-0.308
6	-0.289
7	-0.271
8	-0.254
9	-0.237
10	-0.222
11	-0.209
12	-0.196
13	-0.183
14	-0.179

$\varepsilon 2 =$

	0
0	2.659
1	2.734
2	2.802
3	2.864
4	2.917
5	2.971
6	3.025
7	3.06
8	3.095
9	3.129
10	3.16
11	3.189
12	3.217
13	3.246
14	3.278

$\varepsilon_{Ag} =$

	0
0	-0.388+2.659i
1	-0.384+2.734i
2	-0.369+2.802i
3	-0.345+2.864i
4	-0.327+2.917i
5	-0.308+2.971i
6	-0.289+3.025i
7	-0.271+3.06i
8	-0.254+3.095i
9	-0.237+3.129i
10	-0.222+3.16i
11	-0.209+3.189i
12	-0.196+3.217i
13	-0.183+3.246i
14	-0.179+3.278i

$\varepsilon_m := 1$ **Dielectric function for host material. Vacuum**

$j := 0 .. 299$ **Increment counter**

$$\varepsilon_{eff} := \overrightarrow{\left[\varepsilon_m \cdot \left[1 + \frac{3 \cdot f \cdot \left(\dfrac{\varepsilon_{Ag} - \varepsilon_m}{\varepsilon_{Ag} + 2 \cdot \varepsilon_m} \right)}{1 - f \cdot \left(\dfrac{\varepsilon_{Ag} - \varepsilon_m}{\varepsilon_{Ag} + 2 \cdot \varepsilon_m} \right)} \right] \right]}$$

Maxwell Garnett effective dielectric function for composite layer/film. Equation is from "Absorption and scattering of light by small particles" by Bohren and Huffman. Chapter 8.5 p217 (eqtn 8.50)

Effective dielectric function has 2 components, ε1 and ε2, such that ε=ε1+iε2

$\varepsilon_{eff1} := Re\left(\varepsilon_{eff} \right)$ **Real component**

$\varepsilon_{eff2} := Im\left(\varepsilon_{eff} \right)$ **Imaginery component**

Dielectric function values

$\varepsilon_{eff} =$

	0
0	1.134+0.272i
1	1.141+0.269i
2	1.147+0.266i
3	1.152+0.262i
4	1.155+0.259i
5	1.159+0.255i
6	1.163+0.252i
7	1.165+0.25i
8	1.167+0.247i
9	1.169+0.245i
10	1.171+0.243i
11	1.173+0.241i
12	1.174+0.24i
13	1.176+0.238i
14	1.178+0.237i

Effective dielectric coefficients as a function of wavelength

ε_{eff1}
ε_{eff2} -------

$\lambda1$
Wavelength (nm)
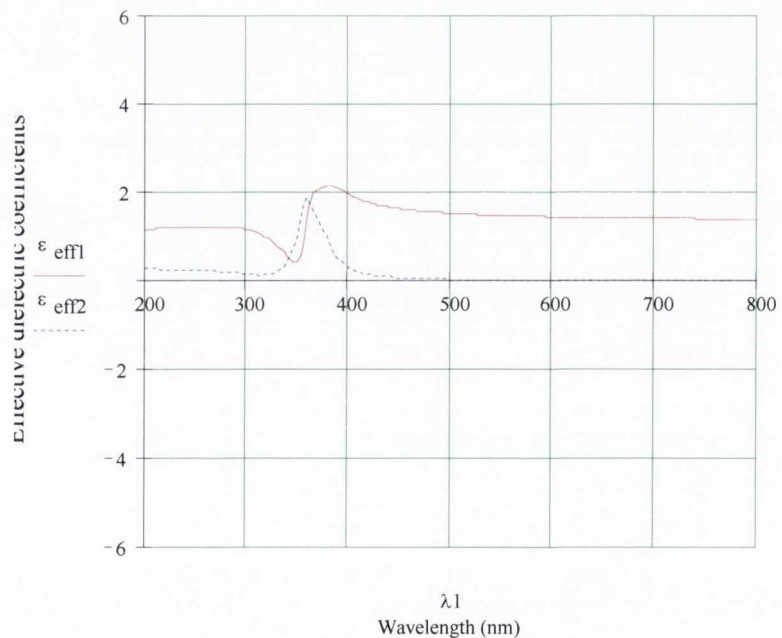
Want effective refractive index and its real and imaginary components

$$n1_{eff} := \sqrt{\frac{\left(\overrightarrow{\left| \varepsilon_{eff} \right| + \varepsilon_{eff1}}\right)}{2}}$$

Real effective refractive index

$$k1_{eff} := \sqrt{\frac{\left(\overrightarrow{\left| \varepsilon_{eff} \right| - \varepsilon_{eff1}}\right)}{2}}$$

Imaginary effective refractive index

$$n_{eff1} := n1_{eff} - i \cdot k1_{eff}$$

Effective refractive index

Effective refractive indices as a function of wavelength
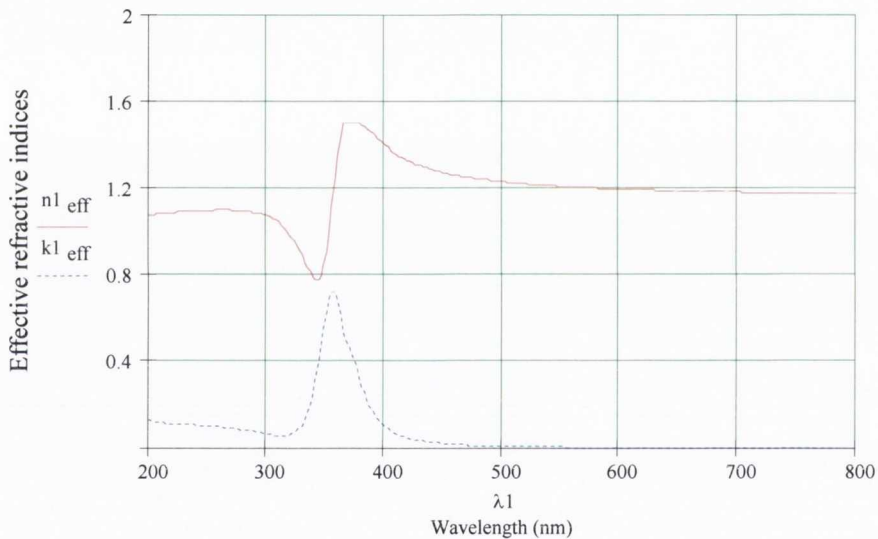
Want to simulate a composite layer with effective refractive index on transparent substrat
Refractive indices for 3 media.

$n_1 := 1$ Ambient - vaccum

$n_2 := n_{eff1}$ Composite layer of effective refractive index

$n_3 := 1.5$ Refractive index of substrate

Use following equations to get the Fresnel coefficients for reflection and transmission. Normal incidence is assumed. Refer to Heavens or Born and Wolf for more info.

$$r_{12} := \overrightarrow{\frac{n_1 - n_2}{n_1 + n_2}} \qquad r_{23} := \overrightarrow{\frac{n_2 - n_3}{n_2 + n_3}} \qquad t_{12} := \overrightarrow{2 \cdot \frac{n_1}{n_1 + n_2}} \qquad t_{23} := \overrightarrow{2 \cdot \frac{n_2}{n_2 + n_3}}$$

$d_{equiv} := 1$ (in nm) **Equivalent thickness of metal film inclusion (can be measured experimentally using deposition monitor)**

$f \equiv 0.1$ **Volume fraction of of silver in composite layer (f=0.1 means 10% of layer is made up of silver)**

$d_{film} := \dfrac{d_{equiv}}{f}$ **Thickness of composite layer**

$d_{film} = 10$ nm

$\delta_{1_j} := \overrightarrow{\left(\dfrac{2 \cdot \pi}{\lambda 1_j} \cdot n_{2_j} \cdot d_{film} \right)}$ **Change in phase of light transversing film (assuming normal incidence)**

Reflectance and transmittance equations

$$R_{n_j} := \left\| \frac{r_{12_j} + r_{23_j} \cdot \exp\left(-2 \cdot i \cdot \delta_{1_j}\right)}{1 + r_{12_j} \cdot r_{23_j} \cdot \exp\left(-2 \cdot i \cdot \delta_{1_j}\right)} \right\|^2 \qquad T_{n_j} := \frac{n_3}{n_1} \cdot \left\| \frac{t_{12_j} \cdot t_{23_j} \cdot \exp\left(-i \cdot \delta_{1_j}\right)}{1 + r_{12_j} \cdot r_{23_j} \cdot \exp\left(-2 \cdot i \cdot \delta_{1_j}\right)} \right\|^2$$

$A_{n_j} := -\log\left(T_{n_j}\right)$ **Absorbance**

Plots of Reflectance, Transmittance and Absorbance as a function of wavelength for composite layer.